UNIVERSIDAD MICHOACANA DE SAN NICOLÁS DE HIDALGO

FACULTAD DE INGENIERÍA ELÉCTRICA

DIVISIÓN DE ESTUDIOS DE POSGRADO

STEADY-STATE AND DYNAMIC SOLUTIONS OF ASYNCHRONOUS LINKS BASED ON VARIABLE FREQUENCY TRANSFORMERS

THESIS

FOR THE DEGREE OF

DOCTOR IN SCIENCES IN ELECTRICAL ENGINEERING

BY

LUIS ALBERTO CONTRERAS AGUILAR

SUPERVISOR:

NORBERTO GARCIA BARRIGA, PH.D.

FEBRUARY 2011

Steady-State and Dynamic Solutions of Asynchronous Links Based on Variable Frequency Transformers

by
Luis Alberto Contreras Aguilar

A thesis submitted to the División de Estudios de Posgrado,
Facultad de Ingeniería Eléctrica of the
Universidad Michoacana de San Nicolás de Hidalgo
for the degree of Doctor in Sciences in
Electrical Engineering

Supervisor:
Norberto García Barriga, Ph.D.

February 2011

STEADY-STATE AND DYNAMIC SOLUTIONS OF ASYNCHRONOUS LINKS BASED ON VARIABLE FRECUENCY TRANSFORMERS

Los Miembros del Jurado de Examen de Grado aprueban
la **Tesis de Doctorado en Ciencias en Ingeniería Eléctrica** de *Luis Alberto Contreras Aguilar*

Dr. J. Jesús Rico Melgoza
Presidente

Dr. Norberto García Barriga
Director de Tesis

Dr. Claudio R. Fuerte Esquivel
Vocal

Dr. Juan Anzurez Marín
Vocal

Dr. Enrique Acha Daza
Revisor Externo
The University of Glasgow

Dr. J. Aurelio Medina Ríos
Jefe de la División de Estudios de Posgrado
En Ingeniería Eléctrica.

UNIVERSIDAD MICHOACANA DE SAN NICOLÁS DE HIDALGO
Febrero 2011

To

Diana, Jacqueline and Leonardo

Acknowledgments

- Firstly, I thanks to God.
- There are not words to express my gratefulness to my wife Diana. Her love, compression, confidence and patience... Thanks my love.
- I would like to express my deep gratitude to my advisor Ph. D. Norberto García for giving me the opportunity to work on this research. His valuable suggestions, his encouragement and patience have been a big help for me over the last four years.
- My acknowledgement to the members of the supervisory committee, for the comments and suggestion that allow to improve this thesis report. Their valuable suggestions were very helpful to finish this thesis.
- A great acknowledgement for the Technology of México (CONACyT) for financial support to carry out Doctor in Sciences studies at the Universidad Michoacana de San Nicolás de Hidalgo.
- Finally, I would like to extend my deepest personal thanks to the department of Programación de Redes Eléctricas of the CFE for accepting me as a visiting student in this department. Thanks Ing. Gonzalo Arroyo, M.C. Guillermo Galicia, M.C. Raúl Adme, M.C. Marco Antonio and M.C. José Acosta.

Abstract

This thesis presents research carried-out on the modelling and analysis of asynchronous links of electric power systems using Variable Frequency Transformers (VFTs). A procedure to determine the stability of a steady-state solution has been implemented and tested with a VFT model suitable for stability studies. In addition, VFT models for harmonic-oriented and planning studies have been implemented.

The aim of the procedure implemented in this work is to determine the stability of a steady-state solution based on a sequential continuation scheme, eigenvalues analysis and a Newton method. The continuation scheme relies on an efficient predictor-corrector scheme, where the correction is accomplished through a Newton method. This acceleration procedure relies on the application of a Newton-Raphson method and the Poincaré map. More important, eigenvalues are computed with the transition matrix identified with a Newton method using a Direct Approach or a Numerical Differentiation procedure. In other words, all the information required to implement the stability analysis is provided by the Newton method. Furthermore, a comprehensive VFT park model is proposed to study the stability of asynchronous links. The VFT park allows the simulation of multi-unit VFTs operated in parallel in order to increase the power transfer between two electric power networks. Each VFT unit consists of a wound rotor induction machine, a DC motor and a control system, which provides power transfer regulation using power and speed controllers. Stability diagrams are reported for changes of the VFT parameters, power transfer and frequency on both sides of the asynchronous link. Even though the VFT is operated within its rated power transfer limits, simulation results reveal that a VFT may become unstable not only for changes of power transfer but also for variations of frequency.

On the other hand, a time domain modelling of a VFT, suitable for harmonic-oriented studies, is proposed in this Thesis. The backbone of the VFT model relies on a saturable wound-rotor induction machine, nonlinear conventional transformers,

shunt capacitor banks and its DC drive motor system. The nonlinear characteristic associated to the saturation effect in the wound rotor induction machine is incorporated with an extrapolation formulation for the magnetizing reactance. The control system includes power, speed and torque regulators to provide power transfer regulation using a separately excited DC machine. Whilst the computation of the periodic steady-state solution is achieved with a Newton method, an implicit integration algorithm based on a numerical differentiation formulation is incorporated to the Newton method to solve power networks with stiff problems. The incorporation of implicit integration algorithms into the Newton method paves the way to efficiently solve complex and realistic networks. This time domain approach is particularly useful for the fast determination of the periodic steady-state of the variable frequency transformer because of the inherently large inertia of its rotary machine, which may cause a prolonged transient response after a system disturbance. Simulation results, which include harmonic analysis, computational effort and dynamic transient tests, are presented for asynchronous interconnections between power networks.

Besides, a VFT model to be used in the Power System Simulator for Engineering (PSS/E) is developed to carry-out planning studies. The rotary machine of the VFT is represented as a phase-shifting transformer for power flow studies, while a set of two ordinary differential equations associated to the mechanic dynamics is incorporated to study the transient solution. The control system provides a mechanic torque drive on the rotor shaft of the rotary machine to control the power flow through the asynchronous link. This comprehensive controller comprises not only the speed and power regulators, but also frequency correction and power-stabilizing. Conventional transformers and shunt capacitor banks are connected at both stator and rotor sides in order to couple the rotary machine with the power grids and provide reactive power compensation, respectively. A study case of a potential project in the Mexican power network is carried-out with this VFT model.

Resumen

Esta tesis presenta el análisis y modelado el dominio del tiempo de enlaces asíncronos de sistemas de potencia asíncronos utilizando Transformadores de Frecuencia Variable (por sus siglas en ingles, VFTs). El análisis se realiza por medio de estudios de estabilidad, análisis de armónicos y estudios de planeación.

En esta tesis se implementa un procedimiento para determinar la estabilidad de la solución de estado estable basado sobre un esquema de continuación secuencial, análisis de valores caracteristicos y un método Newton. El esquema de continuación se basa en un eficiente esquema predictor-corrector en donde el corrector se implementa con un método Newton. Este procedimiento de aceleración se basa en la aplicación del método de Newton-Raphson y el mapa de Poincaré. Aún más importante, los valores caracteristicos se calculan con la matriz de transición identificada con un método Newton usando un procedimiento de Aproximación Directa o Diferenciación Numérica. Es decir, toda la información requerida para implementar el análisis de estabilidad la provee el método Newton. Por otra parte, se propone un modelo completo del parque de VFTs para estudiar la estabilidad de enlaces asíncronos. El parque de VFTs permite la simulación de múltiples unidades operando en paralelo de forma coordinada con la finalidad de incrementar la transferencia de potencia entre los sistemas enlazados. Cada unidad consiste de una máquina de inducción de rotor devanado, un motor de corriente continua y su sistema de control, el cual proporciona regulación de transferencia de potencia utilizando reguladores de potencia y velocidad. Se reportan diagramas de estabilidad para cambios en los parámetros de transferencia de potencia en el VFT y frecuencia en ambos lados del enlace. Los resultados de simulación muestran que el VFT puede llegar a ser inestable aun operando dentro de sus límites de transferencia de potencia nominal y durante cambios en la frecuencia.

Por otra parte, en esta tesis se propone un modelo del VFT en el dominio del tiempo, adecuado para estudios orientados al análisis de armónicos. La parte primordial del

modelo se basa en la máquina de inducción de rotor devanado con su efecto de saturación, transformadores de potencia saturables, bancos de capacitores y un motor de corriente continua con su sistema de control. El sistema de control incluye reguladores de potencia, velocidad y par, los cuales proveen regulación de transferencia de potencia por medio de un motor de corriente continua con excitación independiente. Mientras la obtención de la solución de estado estable periódica se logra con un método Newton, un algoritmo de integración implícito basado en una formulación de diferenciación numérica es implementado para resolver redes eléctricas con problemas de rigidez. La incorporación del algoritmo de integración implícito en el método Newton fortalece la forma de resolver eficientemente las redes complejas y realistas. Esta aproximación en el dominio del tiempo es particularmente útil para la rápida determinación del estado estacionario periódico del VFT debido a la gran inercia en su máquina rotatoria, lo cual puede causar una respuesta transitoria prolongada después de estar sujeta a una perturbación. Se presenta el análisis armónico de un sistema de interconexión asíncrono entre dos sistemas de potencia.

Además, se desarrolla un modelo del VFT en el software comercial Power System Simulator for Engineering (PSS/E). La máquina rotatoria del VFT se presenta como un transformador defasador para estudios de flujos de potencia, mientras que para la solución dinámica se incorporan dos ecuaciones diferenciales ordinarias asociadas a la parte mecánica. El sistema de control proporciona un par mecánico en el eje del rotor del VFT para controlar el flujo de potencia a través del enlace asíncrono. Transformadores convencionales y bancos de capacitores son conectados a ambos lados del estator y del rotor con el fin de acoplar el VFT con las redes de potencia y proveer compensación de potencia reactiva, respectivamente. Con este modelo del VFT se implementa un caso de estudio de un proyecto potencial en el sistema eléctrico Mexicano.

Contents

List of Figures

List of Tables

List of Symbols and Acronyms

$\mathbf{K}^e$	Rotation Matrix.
$\mathbf{L}$	Matrix of Inductances. . . . . [pu]
$\mathbf{x}$	State Vector.
$\mathbf{x}_0$	Initial Condition.
C	Capacitance. . . . . [pu]
D_m	Damping Coefficient. . . . . [pu]
H	Constant of Inertia. . . . . [pu-s]
$\mathrm{K}_{\mathrm{i}v}$	Integral Gain of the Voltage Regulator.
$\mathrm{K}_{\mathrm{i}\omega}$	Integral Gain of the Speed Regulator.
K_{ip}	Integral Gain of the Power Regulator.
K_{iT}	Integral Gain of the Torque Regulator.
$\mathrm{K}_{\mathrm{p}v}$	Proportional Gain of the Voltage Regulator.
$\mathrm{K}_{\mathrm{p}\omega}$	Proportional Gain of the Speed Regulator.
K_{pp}	Proportional Gain of the Power Regulator.
K_{pT}	Proportional Gain of the Torque Regulator.
M	Parameter Vector.
T_e	Electromagnetic Torque. . . . . [pu]

T_m	Mechanic Torque. . . . . [pu]
ω_b	Base Angular Velocity. . . . . [rad/s]
ω_m	Rotor Speed. . . . . [rad/s]
ω_r	Rotor Angular Velocity. . . . . [rad/s]
ω_s	Stator Angular Velocity. . . . . [rad/s]
Φ	Transition Matrix.
ψ	Flux Linkage. . . . . [pu]
Σ	Poincaré Map.
τ	Time Constant of the DC Drive Motor.
θ_m	Rotor Position. . . . . [rad]
d	Direct-Axis Quantity.
e	Synchronous Reference Frame.
I	Identity Matrix.
m_a	Amplitud Modulation Ratio.
q	Quadrature-Axis Quantity.
r_r	Rotor Resistance. . . . . [pu]
r_s	Stator Resistance. . . . . [pu]
Sw	PWM Switch.
x_∞	State Variable at the Limit Cycle.
x_{i+1}	State Variable at the End of the Base Cycle.
x_i	State Variable at the Beginning of the Base Cycle.
x_m	Magnetizing Reactance. . . . . [pu]
X_r	Rotor Reactance. . . . . [pu]

x_r Rotor Leakage Reactance. . . . . [pu]

X_s Stator Reactance. . . . . [pu]

x_s Stator Leakage Reactance. . . . . [pu]

AC Alternate Current.

DC Direct Current.

FACTS Flexible AC Transmission System

GUI Graphical User Interface.

HVDC High Voltage Direct Current.

IIA Implicit Integration Algorithm

ODEs Ordinary Differential Equations.

PCC Points of Common Coupling.

PSS/E Power System Simulator for Engineering.

PST Phase-Shift Transformer.

PWM Pulse Width Modulation.

RPFC Rotary Power Flow Controller.

VFT Variable Frequency Transformer.

VSCs Voltage Source Converters.

WRIM Wound Rotor Induction Machine.

Chapter 1

INTRODUCTION

1.1 Background

The advent of new power transmission technologies provides solutions to specific problems found in power utilities throughout the world. Alternate Current (AC) systems of different frequencies or different control philosophies and electrical regions within a power network can be interconnected by means of asynchronous links. The prevailing technology for accomplish an asynchronous interconnection between power systems is based on High Voltage Direct Current (HVDC) conversion. HVDC technology is a reliable and mature alternative with important advantages such as fast DC power flow control, capability to improve AC systems stability and power transmission over long distances [Arrillaga98a]. However, the operation of this HVDC-based solution is a complex task due to the need to closely coordinate harmonic filtering, reactive compensation and control systems. Moreover, HVDC links have high performance limits when the AC power system on either side has low capacity compared to the HVDC power rating [Runkle02]. Furthermore, an HVDC substation requires a significant space due to the large number of high-voltage switches, filter banks and the terminals cost is high.

A parent technology known as Flexible AC Transmission Systems (FACTS) provides solutions to specific problems at a lower cost. HVDC-VSC is a FACTS controller with the capability to dynamically regulates the active and reactive power in asynchronous interconnections. Power flow control is achieved by the implementation of the PWM techniques and solid-state devices. Furthermore, the PWM technique provides an unrestricted control of both positive and negative sequence voltages [Bahrman07]. This enables a reliable operation of the HVDC-VSC link under unbalanced conditions of in-

terconnected AC systems. Furthermore, the HVDC-VSC link can energize, supply and support an isolated load. However, HVDC-VSC solutions shows considerably higher power losses than a HVDC solution, practical experience with VSC transmission is not extensive and the transmission ratings are ±150 kV and 350 MVA [Andersen05].

A new alternative named Variable Frequency Transformer (VFT) has emerged recently to control power flow throughout asynchronous links. The backbone of a variable frequency transformer is a rotary machine, which has stator windings connected to a first three-phase power system and rotor windings connected to a second three-phase power grid. If the frequency of one system is different from that of the second system, a torque is exerted on the rotor in one direction so as to cause rotation of the rotor at a rotational rate equal to the different between the network frequencies. A closed-loop control system adjusts the rotational position of the rotor with respect to the stator in order to control the power transfer throughout the VFT.

Recent breakthroughs in power transmission technology have made possible the development of the VFT for practical implementations in power systems. Therefore, prospective asynchronous interconnections by means of VFT links will be commissioned during the next years. However, the proliferation of the VFT within the power network requires more detailed studies of its performance under different operating scenarios in order to quantify the impact of its operation. Besides, new models of the VFT are needed to carry-out specific studies such as harmonic and power quality, power flow, transient and stability studies.

1.2 State of the Art

The complexity of modern electric power systems is continuously increasing due to the growth in interconnections and the introduction of new technologies. At the same time, important aspects such as excessive growth in loads, low long-term planning in transmission networks and the need to provide open access to companies and customers, have forced utilities to operate power systems nearly at stability limits. Consequently, there is a need to improve the transmission capacity of electric grids maintaining or increasing the operation security margins. Research work to develop new alternatives for transmission and interconnection of power systems is a permanent pursuit.

HVDC power transmission is an attractive alternative, which has been justified by its low cost compared to the energy transmission in AC high voltage links for long ge-

ographical distances [Arrillaga98b]. The world's first commercial HVDC transmission link was built in 1954 between the Swedish mainland and the island of Gotland with a rating of 20 MW, 200 A and 100 kV. In the open literature, comparative studies can be found of the transmission technologies in AC and Direct Current (DC) [Larruskain05]. On the other hand, FACTS technology based on power electronic converters allows controlling power flow in transmission networks and operating the electric system near its limits without degrading the security and reliability. Moreover, Voltage Source Converters (VSCs) connected in a back-to-back configuration is a new technology that can provide reliable interconnection of electric systems with different voltage levels and frequency [Larsson01]. Nowadays, the application of power electronics in the transmission level relies on power electronic converters known as HVDC and FACTS technologies [Hingorani00].

In the last decade, the interconnection between power system using rotating machines became a reality with the introduction of the Rotary Power Flow Controller (RPFC) [Larsen99], which allows continuos control of power flow in AC transmission. This new device is an attractive alternative to FACTS technology (Phase-Shift Transformers and UPFC). It consists of a combination of two rotary machines that control the power flow through the AC link by adjusting the rotor position of the rotary machines. The basic characteristics of this controller are shown in [Fujita00], where a steady-state analysis for a RPFC is presented. Both steady-state and dynamic models of the RPFC and its control system to regulate the power flow in AC transmission link are described in [Fujita01]. In [Hughes99], the design of two power flow controllers for interconnection between synchronous or asynchronous power systems using electromechanical machines is reported. The design of these power flow controllers is similar to the wound rotor induction machine. The considerations and criteria of design for these machines are given in detail and the control system allows the power transfer in both directions of the interconnected systems. Besides, an experimental model of 10 kW has been operated successfully. The advantages of this device are a fast and continuous control of the power flow, security operation during transient events, no harmonic distortion neither undesirable interactions with control systems. Nevertheless, this controller has not been implemented in real power systems yet.

Recently, a new technology based on rotating machinery reached maturity to offer attractive solutions to the high-bulk power interconnections market. This new device known as Variable Frequency Transformer is able to control power flow through synchronous or asynchronous links between electric systems operating at different voltage

levels and frequency. Currently, this new device is already being incorporated within modern power systems. In [Nabb05] the authors present the first installation of this new technology located at the Langlois substation, which interconnects the New York (USA) and the Hydro-Québec (Canada) power systems. Although the modelling of the VFT for the PSS/E stability software and the Hypersim real time transient simulation software is reported in this latter contribution, no details are provided about the implementation of this model. The modelling of the VFT is validated through comparisons with field measurements and results indicated that this new technology have good agreement with the predicted performance. In [Piwko05], the authors describe the VFT technology and provide an overview of the VFT equipment installed at Langlois substation. An equivalent model of the VFT for planning studies is represented as a phase angle regulator. Besides, the dynamic performance of the VFT has been analyzed and verified by a combination of digital computer simulations and real-time simulator tests using the VFT control system at the Langlois substation. Results of commissioning tests are also included in this work. A maintenance program proposed for the Langlois substation in Hydro-Québec is reported in [Marken08]. The information presented in this paper reveals the that VFT is a reliable device that does not require extensive maintenance programs. Experiences of design, construction and evaluation for a DC machine used to control the torque on the VFT are reported in [Truman07].

A digital simulation model of a VFT and its control system using the Electromagnetic Transient Program is presented in [Chen05], where a set of studies are reported for the energization, speed regulation of rotor, synchronization, ramp power control, step power control, voltage dependent power limit control, islanding operation, reactive power balance and fault analysis. The characteristic response of a VFT under various operating conditions are discussed and its main advantages are reported. In [Nadeau07], the dynamic operation of the VFT for a set of real events is presented. The operation of the VFT under steady-state operation and small disturbances, single-phase and three-phase faults, islanding operation and a trip of a 400 MW power machine are reported.

The second practical application of a VFT installation worldwide is reported in [Hassink07], where a VFT interconnects the Electric Reliability Council of Texas electric company (ERCOT) of USA and the Comisión Federal de Electricidad of México. This new installation is located in Laredo, Texas in the border with México. A general review of this project is presented in [Pratico07], where some additional control features such as tie flow regulation, power runback, reactive power control and black start capability have been included in the Laredo VFT design. Furthermore, this paper includes

simulation tests with a Real-time Simulator for the performance in Laredo VFT substation during undervoltage. [Hassink08] discusses the stability characteristics in the electrical system of the second VFT application and the dynamic stability enhancement using VFT controllers. The VFT is found to provide stability benefits similar to that of a local electric generator. It is also noted that the VFT improves the post-fault voltage recovery and thereby extends the stability margin even with zero power transfer.

A review of the state of the art on the modelling of VFT units reveals that only one paper [Merkhouf08] is devoted to the study of harmonics in VFT instalations. In this contribution, a finite-element analysis and electromagnetic simulations are used for the design of the rotary machine associated to the VFT. Field measurements are carried-out for a four-pole machine rated 100 MW, 17/17 kV, 60 Hz. Extensive electromagnetic simulations showed that the level of torque harmonic distortion is below 2 % of the rated torque. The relationships between active and reactive powers as a function of the rotor position at rated frequency of 60 Hz are presented. Saturation characteristic for this rotary machine is reported in terms of magnetizing current-*vs*-voltage and voltage-*vs*-magnetizing reactance. Besides, the harmonics content of the current harmonics are less than 1% of the rated current during operation at rated power transfer and 1.2 Hz slip frequency. Unfortunately, this contribution provides no information regarding the VFT mathematical representation for harmonic-oriented studies. In addition, harmonic interactions between a VFT unit and power electronics-based controllers for reactive power compensation are not analyzed in this paper.

On the other hand, there exist an increasing interest to develop new projects using one or a set of VFTs working together in a coordinated fashion [Adams08][Pratico10]. A new high-power asynchronous link between Manitoba and Ontario is proposed in [Bagen07], where two technologies are analyzed for this potential project (HVDC back-to-back and VFT). The first multi-unit VFT has been commissioned in Linden, New Jersey to provide a synchronous interconnection with continuous control of power flow between PSEG and ConEd systems. Additional controls features are included in the Linden VFT project. The control features include manual and automatic sequences for multi-unit operation, reactive power control and remote dispatch. The deregulation in electrical markets was the main reason behind this project. In timely contributions [Contreras09a][Contreras09b], steady-state and dynamic solutions are reported for a VFT park model suitable for stability studies. This VFT park consists of a group of VFT connected in parallel to increase the power transfer between to asynchronous network.

Control system is very important in VFT installations, which must include automated sequences for energization, starting and stopping. The VFT at Langlois substation has a control unit that contains automated sequencing functions as power regulator, governor, reactive power control, power runback and a variety of monitoring functions [Piwko05][Nabb05]. For the Laredo VFT project some additional control features have been included in the design such as tie flow regulation, power runback, reactive power control and black start capability [Pratico07]. Nevertheless, these contributions report no details on the modelling of the control system. In [Chen05] an Electromagnetic Transient Program (EMTP) is used to develop a VFT model and its control system, where a flow char for the control system is presented. In two recent contributions [Raslan10][El-Din10] a VFT model is carried-out with Simulink/Matlab program. The VFT equipment is basically an induction machine and a DC machine taken of Simulink/Matlab library. In [Raslan10], a control system is design with ability to perform three main task PI controllers: *i*).- regulate the rotor speed at a synchronous speed that depends on the difference between the two grids frequencies, *ii*).- Control a DC machine to provide a phase shift between the VFT and power grids and *iii*).- regulate DC machine mechanic torque for power flow control. A more sophisticated control system is presented in [El-Din10], which regulates the rotor position with a DC motor coupled with the rotor of the asynchronous machine in order to control the power flow in the VFT. However, only a schematic diagram is provided to explain the control system. Apparently, the state of the art on the design of the VFT control system includes no contributions relying on more sophisticated control schemes such as sliding-mode control, fuzzy logic or the design of observers.

The field of electric power systems has been favored with the application of bifurcation theory. Pioneering research works on the application of bifurcation theory and simple models of power systems [Kwatny86][Dobson89] have shown that the theory of nonlinear dynamics can be used to explain undesirable low-frequency oscillations and voltage collapse. In an EPRI- sponsored research it was concluded that chaos may be presented in simple power system models for a range of loading conditions [Wildberger94]. These results suggested that events in the power system such as voltage collapse, low frequency electromechanical oscillations, and transient stability may be related to chaotic behavior. Indeed, chaotic behaviors in a simple power system have been determined by Lyapunov exponents and a broad-band spectrum [Chiang93]. In addition, the effectiveness of a control scheme based on state vector information has been questioned due to the presence of chaotic behavior for a range load conditions. Bi-

furcation and voltage instabilities are studied in [Kasusky03] using a 3-bus system with two generators and one load consisting of an induction generator and a constant PQ load. Bifurcation diagrams generated with AUTO software showed that a Hopf bifurcation may degradate stability margins and produce voltage collapse. However, authors show that a SVC controller can help to delay the occurrence of such nonlinear phenomena. Chaotic behavior on the IEEE 14-bus benchmark system is studied in [Li09] using a transient stability model and its associated set of differential-algebraic equations. Time domain simulations are carried-out to study this nonlinear phenomenon, where chaos is verified through Lyapunov exponents and a Fourier analysis. Besides, the incorporation of a PSS showed to remove the reported chaotic behavior. In [Carvajal07], the nonlinear behavior of a small power system model with an automated regulator is reported. Stability analysis of nonlinear oscillations associated to a highly nonlinear and time-varying component, namely electric arc furnace, is reported in [Gómez06]. Bifurcation theory and software XPPAUTO are used to report bifurcation diagrams.

Bifurcation theory and continuation techniques have been applied to study nonlinear phenomena such as voltage collapse [Ajjarapu92] and ferroresonance [Kieny91a] in electric power systems. In [Kieny91b], a Galerkin type technique and pseudo-arclength continuation scheme has been used to study the ferroresonance characteristic of a transformer connected to a bus through the capacitance. Furthermore, a time domain approach based on Newton method and a hybrid technique has been proposed for the analysis of ferroresonance in a circuit with a saturable reactor [Naidu97]. Recent work on transient stability, bifurcation and chaos of a DC motor and a synchronous generator set model is presented in [Xize02]. Floquet theory and nonlinear mode are applied to investigate the presence of Hopf bifurcation, period-doubling bifurcation and chaos associated to large line resistance. A stability analysis based on bifurcation theory is presented for a DSTATCOM in [Segundo09]. A DSTATCOM model to perform bifurcation analysis is proposed, while stability regions and contour lines are determined with a sequential predictor-corrector scheme and Floquet multipliers. While the predictor is carried out using an extrapolation method based on a cubic spline, a Newton method and a numerical differentiation approach are used as a corrector. Furthermore, in a recent research work [Segundo10a], bifurcation theory, continuation methods and Newton methods has been applied to perform stability analyses of custom power devices. The stability analysis of a DSTATCOM and DVR is presented using predictor-corrector scheme. The predictor is based on an extrapolation method based on a cubic spline, whilst corrector is implemented with a Newton method based on a Discrete Exponen-

tial Expansion approach. The steady-state and dynamic solutions of a adjustable speed drive is reported in [Segundo10b]. The periodic steady-state is computed with a Discrete Exponential matrix and the Poincaré map. Floquet theory is applied to determine the local stability of the solutions. However, no information is provided in these three latter contributions about how to determine the Jacobian of the Poincaré map required to compute the Floquet multipliers. The computation of the Jacobian of the Poincaré map is not a minor subject in order to carry out stability studies. The crucial step of computing the Jacobian matrix of the Poincaré map can be achieved by determining an analytical expression or using a numerical approximation. For instance, sensitivity analysis methods based on sensitivity equations or adjoint equations can be used to determine this Jacobian matrix [Banerjee01]. In switching circuits, the Poincaré map Jacobian of a periodic orbit can be obtained by dividing one period of operation into subintervals. A Poincaré map Jacobian is computed for each subinterval and the chain rule is applied to the Jacobian of the Poincaré map as the product of the Jacobians for the subintervals [Banerjee01].

On the other hand, the development of averaging methods has been a topic of interest for the power electronic community for over three decades. These averaging methods can be useful for computing the steady-state and performing stability analysis by setting to zero and linearizing the averaged model, respectively. Averaging theory based on classical Russian averaging techniques is widely used in the analysis of PWM-based power electronic systems [Middlebrook76]. However, this state-space averaging method may show discrepancies at lower switching frequencies and, therefore, is limited to systems with time discontinuities and large ripple conditions. The reason behind these discrepancies relies on the fact that conventional state-space average models are actually independent of frequency. As a consequence, reducing switching frequencies degradates the accuracy of these models, increasing the percentage error in the state variables [Caliskan99]. A more general averaging scheme based on a time-dependent Fourier series representation has proven to be suitable to model not only Pulse Width Modulation switching circuits, but also a wide range of power circuits [Sanders91]. An additional refinement of the Generalized Averaging method allows estimating the average as well as the ripple in the state variables even at low-switching frequencies and high-ripple levels [Caliskan99]. Average modeling decreases simulation time and suppresses some fast time constants compared to a conventional simulation tool. However, the modeling complexity increases with the number of switches and the nature of the operating mode. In a recent contribution, the concept of dynamic phasors based

on a generalized averaging procedure has been put forward to determine approximate nonlinear models [Stankovic00]. This proposal offers a good compromise between accuracy and computational effort for a benchmark power system test case consisting of a three-phase synchronous generator. However, it must be brought to attention the fact that the size of the resulting dynamic phasor model is proportional to the number of retained harmonics.

Even though the state of the art of the VFT is sufficient to understand the operation of this new device, additional studies are needed to quantify its performance and operation within modern power systems. As an example, it must be brought to attention the fact that despite the different approaches reported in the latter contributions to analyze the operation of VFT, no attempts have been made to apply a stability-oriented analysis. Furthermore, a review of the literature reveals that there is a lack of VFT models for harmonic-oriented studies. More detailed studies on power quality and planning studies for potential projects of electric systems links with the VFT are needed.

1.3 Objectives

The main objective of this thesis is the time domain modelling and analysis of asynchronous links between two power systems based on VFTs. Furthermore, the steady-state and dynamic solutions of the VFT device will be computed for a set of operating scenarios.

The specific objectives of this work are:

- To develop a variable frequency transformer model to carry-out stability studies.
- To develop a variable frequency transformer model to carry-out harmonic-oriented studies.
- To develop a variable frequency transformer model in PSS/E software to carry-out planning studies.
- To carry-out stability studies of the VFT using a sequential continuation scheme and Newton method.
- To carry-out harmonic-oriented studies of the VFT using an acceleration procedure based on a Newton method and an embedded implicit integration algorithm.

1.4 Motivation

Due to excessive growth in loads with respect to the growth of power plants and long-term planning in transmission networks, there exist a great interest to develop new technologies to improve power exchange between power systems. These technologies must satisfy both security and reliability specifications of the power system.

FACTS technology improves transmission capability and allows interconnections of electrical systems. However, this technology has the disadvantage of producing distortion in current and voltage waveforms due to nonlinear characteristic of the power electronic converters. For this reason, the introduction of the variable frequency transformer represents an alternative for practical implementations of synchronous and asynchronous links between power systems.

At present, the first two commercial VFT installations worldwide are located in the American Continent. The Langlois project is located at the border of Canada and USA, while the Laredo project is operated in the border of México and USA. New projects are being commissioned in order to apply this technology to interconnect electrical regions within an electric power network. In particular, the Comisión Federal de Electricidad in México is carrying-out preliminary studies to build new interconnections links in the north of the country.

A review of the state of the art reveals that there are only few contributions on the modelling of this new technology. Therefore, further research work is required to understand its performance under different operating scenarios. Besides, it is desirable to introduce modern tools to the analysis of asynchronous links using variable frequency transformers.

1.5 Methodology

The methodology employed to reach the goals of this research work is described as follows. Firstly, an important work was devoted to review the state of the art on the modelling and analysis of variable frequency transformers. In order to carry-out the stability studies of asynchronous links using VFTs, a procedure to determine the stability of a system will be implemented using a sequential continuation scheme, eigenvalues analysis and a Newton method. Besides, the Newton method is used in this thesis to compute steady-state solutions of asynchronous links incorporating the VFT. A Direct Approach and Numerical Differentiation procedures have been applied to compute

the transition matrix used in the Newton method, where the eigenvalues are computed with the transition matrix. On the other hand, a VFT park configuration is developed in this research work in order to increase the power transfer between two asynchronous networks. The backbone of the VFT is modelled with a wound rotor induction machine using the synchronous reference frame. Furthermore, a VFT model for harmonic-oriented analyses is presented in this work, where the nonlinearity associated to the saturation of the rotary machine is incorporated in the magnetizing inductance using a interpolation procedure. Simple control systems are incorporated to the VFT model. These controllers include power and speed regulators implemented with PI controllers. The harmonic steady-state analysis is carry-out with a powerful blend based on the Newton method and an implicit integration algorithm. The implicit integration algorithm is implemented using a numerical differentiation formulation in terms of backward differences, suitable to overcome stiffness problems associated with the nonlinear conventional transformer implemented in this work. A harmonic-oriented study was carried-out with the saturable VFT model. Lastly, it was developed a VFT user model will be implemented using the PSS/E program for planning studies of asynchronous links. The VFT user model is developed based on basic equation of a equivalent system with two differential equations. Additionally, a comprehensive control system is incorporated to the user written model using a FLEC/FORTRAN code. PSS/E program is used to compile the FLEC/FORTRAN code and to create a VFT user model in the PSS/E library. The VFT user model is used to analyze a potential project in the Mexican power system.

1.6 Original Contributions

An overview of the original contributions of the thesis is given here. The developments and findings are listed as follows,

1. Stability analyses of variable frequency transformers based on a sequential continuation scheme and a Newton method. The computation of the eigenvalues is accomplished with the transition matrix provided by the Newton method.

2. Development of the variable frequency transformer park model for stability studies.

3. Development of the VFT model for harmonic-oriented studies incorporating the

saturation characteristic of the induction machine. The steady-state solution is determined with the Newton method and an implicit integration algorithm, suitable for solving ordinary differential equations with stiff problems.

4. Development of a VFT model for planning studies using the PSS/E software.

1.7 Thesis Structure

The outline of this thesis is described as follows. In Chapter 2 an approach to determine the stability of a steady-state solution using a sequential continuation scheme, eigenvalues analysis and the Newton method is presented. Furthermore, a comprehensive VFT park model, suitable for stability studies, is implemented. It consists of a group of VFTs working together in a coordinated fashion to increase power transfer between two asynchronous systems.

Chapter 3 presents a nonlinear model of the variable frequency transformer in a phase-coordinate representation. Besides, a powerful blend based on an implicit integration algorithm and the Newton method is proposed to compute of the periodic steady-state solution of the time domain representation of the VFT. Test results are reported in terms of convergence to the periodic steady-state, time domain waveforms, harmonics and speedup factors.

Chapter 4 presents a VFT model to be used in the Power System Simulator for Engineering (PSS/E). The steady-state model is included as a phase-shifter transformer which is already included in the PSS/E library. A user written VFT model for transient analysis is developed and included in the simulations.

Finally, Chapter 5 presents the general conclusions drawn from this research and outline directions for further research.

1.8 Publications

The publications derived from this research work are:

Refereed papers in journal

- **L. Contreras-Aguilar** and N. Garcia, "Stability Analyses of a VFT Park Using a Sequential Continuation Scheme and the Limit Cycle Method", *IEEE Transactions on Power Delivery* (Accepted for publication).

Papers in conference proceedings:

- **L. Contreras-Aguilar** and N. Garcia, "Fast Convergence to the Steady-State Operating Point of a VFT Park Using the Limit Cycle Method and a Reduced Order Model", *IEEE Power Engineering Society General Meeting*, Calgary Canada, pp. 1-5, July 2009.
- **L. Contreras-Aguilar** and N. Garcia, "Steady-State Solution of a VFT Park Using the Limit Cycle Method and a Reduced Order Model", *IEEE PowerTech*, Bucharest Rumania, pp. 1-6, June-July 2009.
- **L. Contreras-Aguilar** and N. Garcia, "Accelerated Time Domain Solutions of a VFT Using the Poincaré Map Method with an Embedded Implicit Integration Algorithm", *North American Power Symposium*, Calgary Canada, pp. 1-8, September 2008.
- **L. Contreras-Aguilar** and N. Garcia, "Periodic Solutions of Stiff Systems Using the Limit Cycle Method and an Implicit Integration Technique", *International Power Engineering Conference*, Singapore Singapore, pp. 854-859, December 2007.

Chapter 2

MODELLING AND ANALYSIS OF A VFT FOR STABILITY STUDIES

2.1 Introduction

Modern electric power suppliers must be able to maintain not only the reliability of the system, but also high power quality standards and low cost operation. In addition, the increasing demand placed on grid utilities has favoured the introduction of new technologies to alleviate these requirements. High Voltage Direct Current transmission represents a reliable option, which is particularly useful for long distance transmission and constitutes an asynchronous interconnection with or without a transmission network. Power electronics based solutions known as FACTS controllers provide solutions for controlling power flow and enhancing the transmission systems capacity. On the other hand, recent improvements in power transmission technology have favoured the development of the Variable Frequency Transformer (VFT), which represents an attractive alternative to provide bi-directional control of power transfer between two electric power grids and to fully utilize available transmission capability. Its capacity to provide control of power transfer between two electric systems using a rotary machine has been demonstrated in VFT installations for commercial operation.

In this Chapter, a comprehensive VFT park model, suitable for stability studies is implemented. Each VFT unit within the VFT park comprises a Wound Rotor Induction Machine (WRIM), a DC motor, conventional transformers, reactive compensation and a control system. The validation of WRIM is carried-out using commercial software such as PSCAD/EMTDC. Besides, a procedure to determine the stability of a steady-state

solution using a sequential continuation scheme, eigenvalues analysis and the Newton method is implemented. The steady-state operating point of a 300 MW VFT park is computed with the Newton method, while stability analyses of the VFT park are carried out with a sequential continuation scheme based on the Newton method and eigenvalues analysis.

2.2 Basic VFT Configurations

VFT technology consists of a rotary transformer similar to a wound rotor induction machine, where a power system is connected to the stator three-phase winding through a conventional transformer and another power system is connected to the rotor three-phase winding through a collector system and a conventional transformer [Nabb05]. The collector system is designed with conventional technology based on carbon-brush technology on copper slip rings. A closed-loop power regulator maintains power transfer equal to a power reference. The regulator compares the measured power with the power reference and adjusts torque applied to the rotor shaft of the rotary transformer. A DC motor and a variable-speed drive system are used to provide frequency matching by continuous rotation in either direction and to provide regulated torque, thereby controlling the direction and the magnitude of the power flow through the VFT. In steady-state, power flow is proportional to the magnitude and direction of the torque applied. Regardless of power flow, the rotor inherently orients itself to follow the phase angle difference imposed by the two asynchronous systems and rotates continuously if the grids are at different frequencies. For the case of a synchronous link between tow power sytems with the same frequency the rotor will not rotate and it can be viewed as a conventional transformer. In addition, the VFT has a magnetizing reactance and a leakage reactance that consumes reactive power as a function of current flow. For this reason, capacitor banks are required to alleviate reactive power demanded by the VFT and the adjacent transmission system.

So far, two VFT installations have been implemented worldwide. The basic VFT configurations for these installations are shown in Figure 2.1. Figure 2.1 (a) shows a simplified one-line diagram of the first commercial application of a VFT technology located at Langlois Canada, which started operation in early 2004 [Piwko05]. This world's first VFT was initially designed as a 100 MW, 17 kV asynchronous link to supply power to New York and Ontario systems. It comprises a 100 MW rotary transformer,

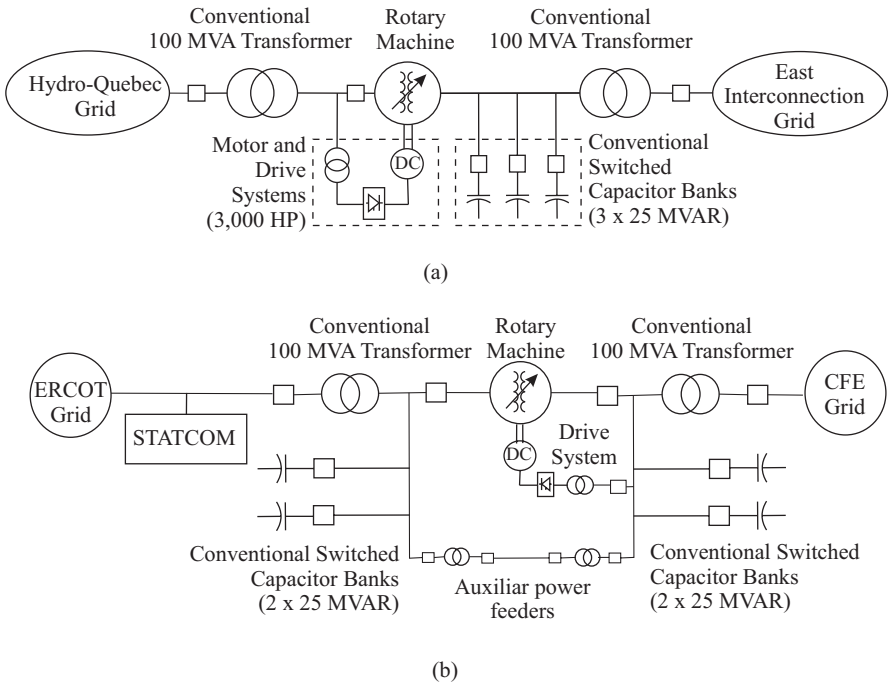

Figure 2.1: One-line diagram for (a) Langlois VFT substation and (b).- Laredo VFT substation.

one 3750 HP DC motor, a variable speed drive system, three 25 MVAR switched shunt capacitor banks and two 120/17 kV conventional generator step-up transformers. The Langlois VFT station has been designed to be expandable. The building is designed for future expansion to accommodate another 100 MW rotary transformer and its auxiliary equipment. The instalation has space for transformers, capacitor banks and switchgear associated with a second VFT unit.

The Langlois scheme was immediately followed by a second installation with the same capacity. The Laredo project is located in southwest Texas, at the electrical interface between the Electric Reliability Council of Texas (ERCOT) power grid in USA and the Comisión Federal de Electricidad (CFE) power grid of México [Pratico07]. A 100 MW VFT was installed at Laredo to enable power transfer between the two asynchronous power grids. Figure 2.1 (b) shows a simplified one-line diagram of the Laredo VFT, which contains one 100 MW rotary machine at 17 KV, one 3750 HP DC motor and a variable speed drive system, four 25 MVAR switched shunt capacitor banks, two 142/17 kV conventional step-up transformers and two auxiliary power transformers. On the ERCOT side, there are several 138 kV transmission lines, generators, switched capacitor banks at 138 kV and 69 kV, and a 150 MVAR STATCOM that regulates 138

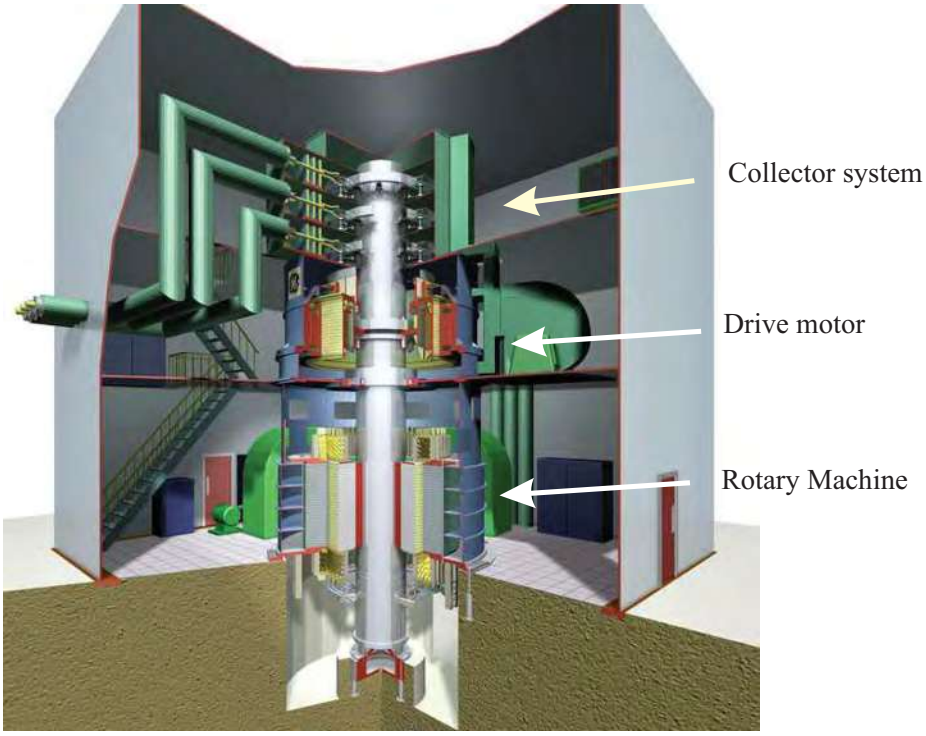

Figure 2.2: Cut-away Drawing of VFT.

kV bus voltages. On the CFE side, the VFT connects to the CFE system through 138 kV and 230 kV transmission lines with a 230/138 kV autotransformer and two switched capacitor bank rated 25 MVAR at 138 kV.

The core technology of the VFT is a rotary machine with three-phase windings on both rotor and stator. Figure 2.2 shows the main components of a VFT installation, including the collector system, drive motor and rotary machine. A variable frequency transformer is a doubly-fed electric machine resembling a vertical shaft hydroelectric generator with a three-phase wound rotor. The collector system conducts current between the three-phase rotor winding and its stationary network. In addition, a DC torque motor is mounted on the same shaft. A change in the direction of the torque applied to the shaft results in a change in the direction of power flow. For a no-applied torque condition, the shaft rotates due to the difference in frequency between the networks connected to the rotor and stator sides.

Figure 2.3 depicts a map of North America highlighting the current and potential VFT projects. It can be appreciated the progress made with VFT technology during the last decade. In addition to two VFT installations already in commercial operation at Langlois and Laredo, there are two additional prospective interconnection links between

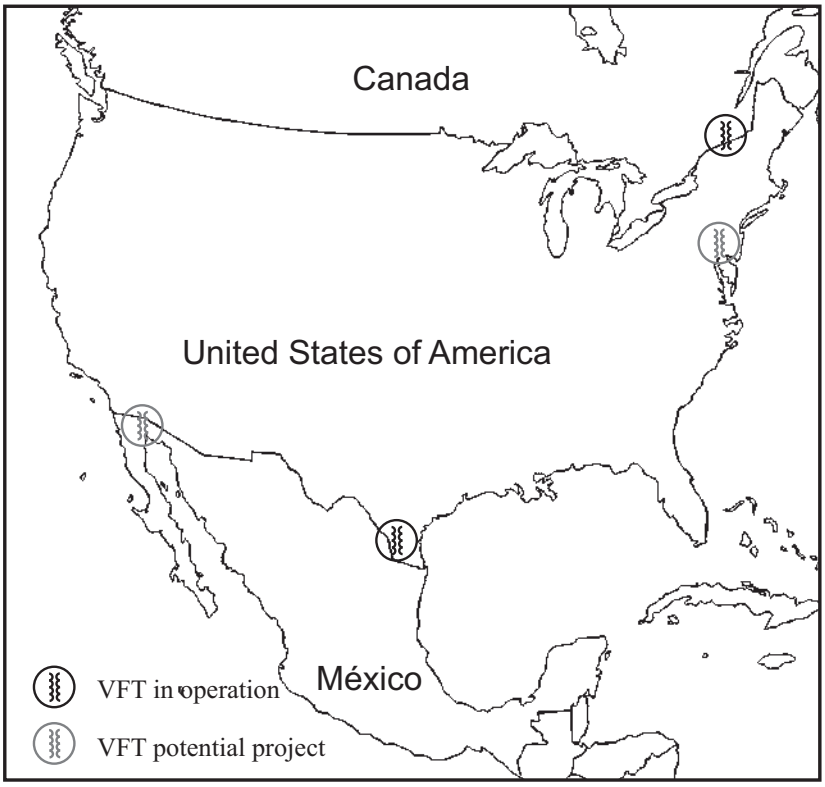

Figure 2.3: Map of North America highlighting current and prospective VFT installations.

two systems of the same nominal frequency: the Linden project in New York and the BC project in Baja California.

2.3 VFT Park Model

A VFT park model is presented in this section, which consists of a set of VFTs operated in parallel to increase the power exchange between two asynchronous networks. Figure 2.4 shows the general configuration of the VFT park proposed for power exchange between two asynchronous power grids. This novel topology for a VFT park comprises of a set of n VFT units connected in parallel, where each unit is modelled with a WRIM, a control system, coupling transformers and capacitor banks. The control system proposed in this work for the VFT park is a different alternative to those controllers reported in the literature. Three representations for the WRIM are proposed using a full model of order six and reduced order models. The control system consists of a power regulator working together with a speed regulator to adjust the mechanic

torque drive.

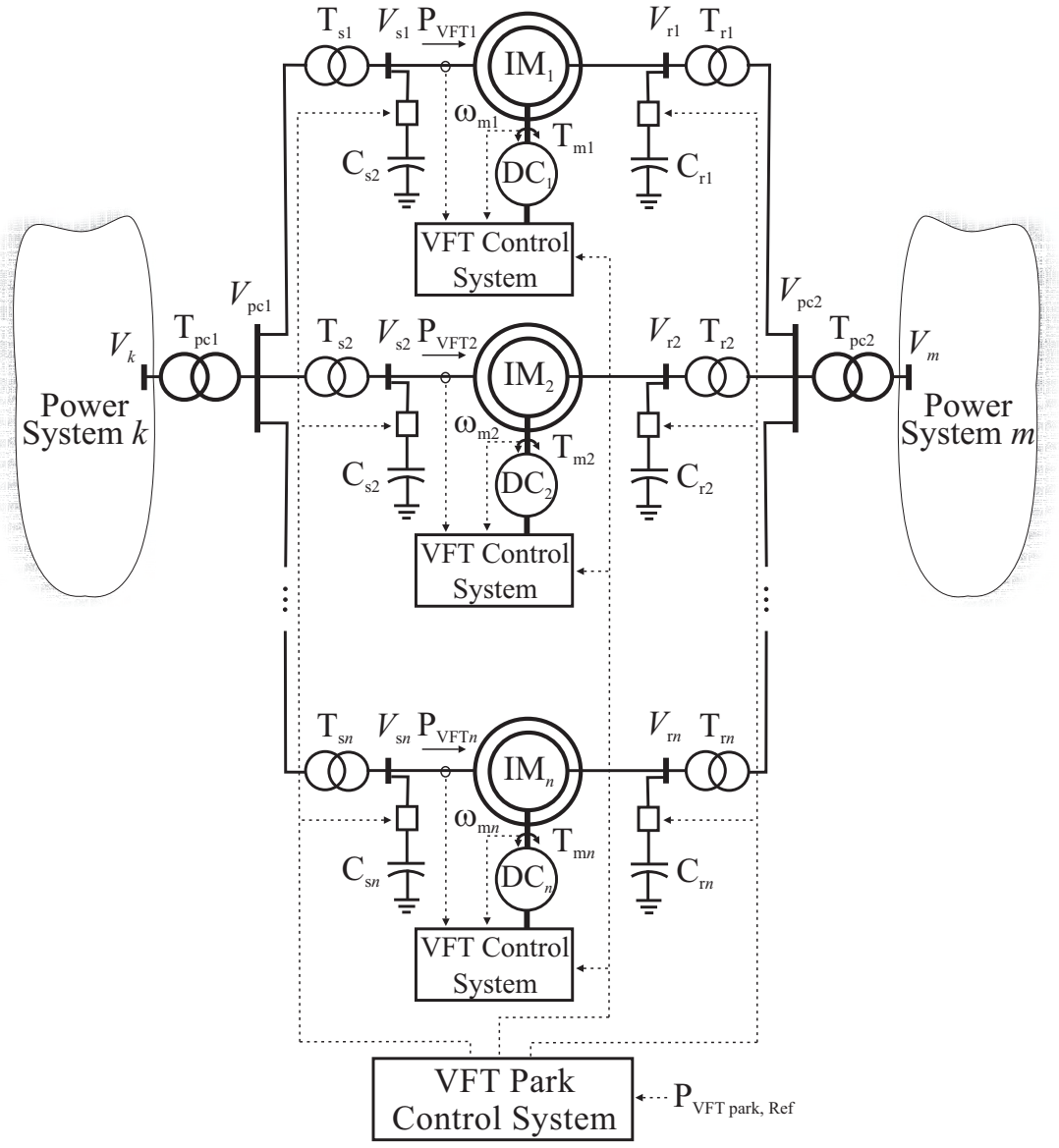

Figure 2.4: VFT park consisting of multi-unit VFTs.

2.3.1 WRIM Full and Reduced Models

The dynamic behavior of the WRIM can be described in the synchronous reference frame in terms of the flux linkages using a model of order six. The stator voltage equations are defined in pu as [Nelson69],

$$\frac{1}{\omega_b}\frac{d}{dt}\begin{bmatrix} \psi^e_{qs,i} \\ \psi^e_{ds,i} \end{bmatrix} = \frac{\omega^e_s}{\omega_b}\begin{bmatrix} 0 & -1 \\ 1 & 0 \end{bmatrix}\begin{bmatrix} \psi^e_{qs,i} \\ \psi^e_{ds,i} \end{bmatrix} - \begin{bmatrix} r_s & 0 \\ 0 & r_s \end{bmatrix}\begin{bmatrix} I^e_{qs,i} \\ I^e_{ds,i} \end{bmatrix} + \begin{bmatrix} V^e_{qs,i} \\ V^e_{ds,i} \end{bmatrix} \tag{2.1}$$

and the rotor voltage equations are,

$$\frac{1}{\omega_b}\frac{d}{dt}\begin{bmatrix} \psi^e_{qr,i} \\ \psi^e_{dr,i} \end{bmatrix} = \begin{bmatrix} 0 & -\mathrm{S} \\ \mathrm{S} & 0 \end{bmatrix}\begin{bmatrix} \psi^e_{qr,i} \\ \psi^e_{dr,i} \end{bmatrix} - \begin{bmatrix} r_r & 0 \\ 0 & r_r \end{bmatrix}\begin{bmatrix} I^e_{qr,i} \\ I^e_{dr,i} \end{bmatrix} + \begin{bmatrix} V^e_{qr,i} \\ V^e_{dr,i} \end{bmatrix} \tag{2.2}$$

with

$$\mathrm{S} = \frac{\omega^e_s - \omega_{m,i}}{\omega_b} \tag{2.3}$$

where ψ is the flux linkage, the superscript e denotes the synchronous reference frame, the subscript i indicates the WRIM number ($i = 1, ..., n$), ω_b is the base angular velocity, ω^e_s is the stator angular velocity, r_s is the stator resistance, r_r is the rotor resistance, I^e_{qs} is the quadrature-axis stator current, I^e_{ds} is the direct-axis stator current, I^e_{qr} is the quadrature-axis rotor current, I^e_{dr} is the direct-axis rotor current, V^e_{qs} is the quadrature-axis stator voltage, V^e_{ds} is the direct-axis stator voltage, V^e_{qr} is the quadrature-axis rotor voltage, V^e_{dr} is the direct-axis rotor voltage and ω_m is the rotor speed,. Besides, the relation

$$\begin{bmatrix} V^e_{qr,i} \\ V^e_{dr,i} \end{bmatrix} = \mathbf{K}^e \begin{bmatrix} V_{qr,i} \\ V_{dr,i} \end{bmatrix} \tag{2.4}$$

transforms rotor supply voltage to the synchronous reference frame [Krause94], where $\mathbf{K}^e$ is the transformation matrix between rotor and stator reference frames defined as,

$$\mathbf{K}^e = \begin{bmatrix} cos(-\theta_{m,i}) & -sin(-\theta_{m,i}) \\ sin(-\theta_{m,i}) & cos(-\theta_{m,i}) \end{bmatrix} \tag{2.5}$$

where θ_m is the rotor position.

The currents through the WRIM in terms of the flux linkages are [Nelson69],

$$\begin{bmatrix} I^e_{qs,i} \\ I^e_{ds,i} \\ I^e_{qr,i} \\ I^e_{dr,i} \end{bmatrix} = \frac{1}{X_D} \begin{bmatrix} X_r & 0 & -x_m & 0 \\ 0 & X_r & 0 & -x_m \\ -x_m & 0 & X_s & 0 \\ 0 & -x_m & 0 & X_s \end{bmatrix} \begin{bmatrix} \psi^e_{qs,i} \\ \psi^e_{ds,i} \\ \psi^e_{qr,i} \\ \psi^e_{dr,i} \end{bmatrix} \tag{2.6}$$

with $X_s = x_s + x_m$, $X_r = x_r + x_m$, $X_D = X_s X_r - x_m^2$. Moreover, x_s is the stator leakage reactance, x_r is the rotor leakage reactance and x_m is the magnetizing reactance [Krause94].

The electromagnetic torque, rotor speed and rotor position associated to the mechanical equations are defined as follows [Krause94],

$$\mathrm{T}_{e,i} = x_m \left[I^e_{qs,i} I^e_{dr,i} - I^e_{ds,i} I^e_{qr,i} \right] \tag{2.7}$$

$$\frac{d}{dt}\left(\frac{\omega_{m,i}}{\omega_b}\right) = \frac{\mathrm{T}_{e,i} - \mathrm{T}_{m,i} - \mathrm{D_m}\left(\frac{\omega_{m,i}}{\omega_b}\right)}{2\mathrm{H}} \tag{2.8}$$

$$\frac{d}{dt}\theta_{m,i} = \omega_b\left(\frac{\omega_{m,i}}{\omega_b}\right) - (\omega^e_s - \omega^e_r) \tag{2.9}$$

where T_e is the electromagnetic torque, T_m is the mechanic torque, ω_m is the rotor speed, H is the constant of inertia, D_m is the damping coefficient and ω^e_r is the rotor angular velocity. The ordinary differential equations that describe this six order model are (2.1), (2.2), (2.8) and (2.9).

WRIM Fourth-Order Model

Assuming that the stator transient of the induction machine in the synchronous reference frame is neglected, the terms $\frac{d\psi}{dt}$ in the stator voltage equations (2.1) can be discarded [Krause79]. Then, the stator voltage equations are,

$$\begin{bmatrix} 0 \\ 0 \end{bmatrix} = \frac{\omega^e_s}{\omega_b} \begin{bmatrix} 0 & -1 \\ 1 & 0 \end{bmatrix} \begin{bmatrix} \psi^e_{qs,i} \\ \psi^e_{ds,i} \end{bmatrix} - \begin{bmatrix} r_s & 0 \\ 0 & r_s \end{bmatrix} \begin{bmatrix} I^e_{qs,i} \\ I^e_{ds,i} \end{bmatrix} + \begin{bmatrix} V^e_{qs,i} \\ V^e_{ds,i} \end{bmatrix} \tag{2.10}$$

Solving (2.10) for $\psi^e_{qs,i}$ and $\psi^e_{ds,i}$ with $\frac{\omega^e_s}{\omega_b} = 1$ results,

$$\begin{bmatrix} \psi^e_{qs,i} \\ \psi^e_{ds,i} \end{bmatrix} = \begin{bmatrix} -r_s & 0 \\ 0 & r_s \end{bmatrix} \begin{bmatrix} I^e_{qs,i} \\ I^e_{ds,i} \end{bmatrix} + \begin{bmatrix} V^e_{qs,i} \\ -V^e_{ds,i} \end{bmatrix} \tag{2.11}$$

and substituting in the current equations (2.6), then the stator and rotor currents can be computed as,

$$\begin{bmatrix} I^e_{qs,i} \\ I^e_{ds,i} \\ I^e_{qr,i} \\ I^e_{dr,i} \end{bmatrix} = \begin{bmatrix} X_D & -r_s X_r & 0 & 0 \\ r_s X_r & X_D & 0 & 0 \\ 0 & -r_s x_m & X_D & 0 \\ -r_s x_m & 0 & 0 & X_D \end{bmatrix}^{-1} \begin{bmatrix} 0 & -X_r & -x_m & 0 \\ X_r & 0 & 0 & -x_m \\ 0 & x_m & X_s & 0 \\ -x_m & 0 & 0 & X_s \end{bmatrix} \begin{bmatrix} V^e_{qs,i} \\ V^e_{ds,i} \\ \psi^e_{qr,i} \\ \psi^e_{dr,i} \end{bmatrix} \tag{2.12}$$

Therefore, the Ordinary Differential Equations (ODEs) that describe this reduced model are only (2.2), (2.8) and (2.9).

WRIM Second-Order Model

A set of algebraic equations in terms of the flux linkages is obtained by dropping the operator $\frac{d}{dt}$ in (2.1) and (2.3). These equations are solved for $\psi^e_{qs,i}$, $\psi^e_{ds,i}$, $\psi^e_{qr,i}$, $\psi^e_{dr,i}$ and substituted in (2.6). The stator and rotor currents can be computed as,

$$\begin{bmatrix} I^e_{qs,i} \\ I^e_{ds,i} \\ I^e_{qr,i} \\ I^e_{dr,i} \end{bmatrix} = \begin{bmatrix} X_s & -r_s & x_m & 0 \\ r_s & X_s & 0 & x_m \\ x_m & 0 & X_r & -\mathrm{S}^{-1} r_r \\ 0 & x_m & \mathrm{S}^{-1} r_r & X_r \end{bmatrix}^{-1} \begin{bmatrix} V^e_{qs,i} \\ V^e_{ds,i} \\ -\mathrm{S}^{-1} V^e_{qr,i} \\ \mathrm{S}^{-1} V^e_{dr,i} \end{bmatrix} \tag{2.13}$$

This reduced order model is defined with only two ODEs (Equations (2.8) and (2.9)).

2.3.2 Control System

The VFT park control system determines the number of VFT units required to reach the desired power transfer capacity. In order to coordinate the operation of the VFT units, the VFT park control system is based on a dispatch power strategy. It compares the VFT park power capacity with the demanded power transfer and assigns a rated power transfer command to as many VFT units as possible. Then, each VFT unit control system receives a control signal so as to contribute with a specific power flow.

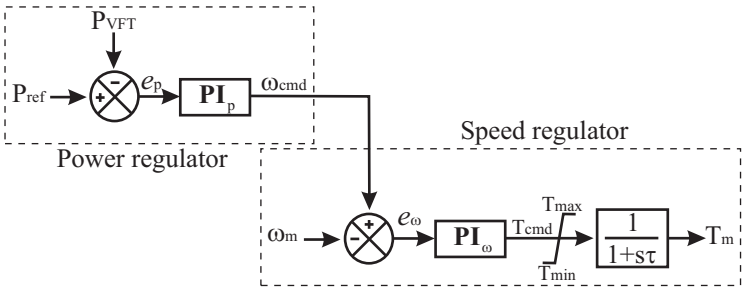

Figure 2.5: VFT unit control system including power and speed regulators.

Reactive power compensation is provided on both sides of the VFT installation in order to alleviate the reactive power demand of each VFT unit. It consists of shunt capacitor banks, which are switched as a function of the VFT power transfer. While the stator-side three-phase capacitor bank is switched-in for an input power transfer reference $\mathrm{P_{ref}} > 0$, the rotor-side three-phase reactive compensator is connected for $\mathrm{P_{ref}} > 0.5\,\mathrm{P_{rated}}$, where $\mathrm{P_{rated}}$ is the rated power transfer capacity of the VFT unit.

Figure 2.5 illustrates an elementary control system for one VFT unit, which provides power regulation by adjusting the rotor speed [VFT07]. The power regulator shown in Figure 2.5 measures the power flow throughout the VFT ($\mathrm{P_{VFT}}$) and compares it with its power reference ($\mathrm{P_{ref}}$). The error signal is fed to a PI controller and its output represents a speed command ω_{cmd}. This PI controller is defined as,

$$\frac{d}{dt}y_\omega = \mathrm{K_{ip}}(\mathrm{P_{ref}} - \mathrm{P_{VFT}}) \tag{2.14}$$

and the speed command is computed with,

$$\omega_{cmd} = y_\omega + \mathrm{K_{pp}}(\mathrm{P_{ref}} - \mathrm{P_{VFT}}) \tag{2.15}$$

where $\mathrm{K_{pp}}$ is the proportional gain of the power regulator and $\mathrm{K_{ip}}$ is the integral gain of the power regulator.

On the other hand, the speed regulator compares the speed command ω_{cmd} determined by the power regulator and the rotor speed ω_m. A PI controller computes the commanded torque $\mathrm{T_{cmd}}$ using the speed error signal. A torque limiter prevents the torque command to be within the motor capability. In this work, the rate of change of the driving torque command is allowed to take values between ± 5 pu [VFT07]. However, the torque limit is determined by the design of the DC machine for practical implementations. The torque drive feeds a first order system that represents the dy-

namic response of the DC drive motor. Then, the speed regulator is defined with two differential equations [Contreras09b],

$$\frac{d}{dt}\begin{bmatrix} y_{\mathrm{T}} \\ \mathrm{T}_m \end{bmatrix} = \begin{bmatrix} 0 & 0 \\ \tau^{-1} & -\tau^{-1} \end{bmatrix}\begin{bmatrix} y_{\mathrm{T}} \\ \mathrm{T}_m \end{bmatrix} + \begin{bmatrix} K_{i\omega} & -K_{i\omega} \\ K_{p\omega}\tau^{-1} & -K_{p\omega}\tau^{-1} \end{bmatrix}\begin{bmatrix} \omega_{cmd} \\ \omega_m \end{bmatrix} \tag{2.16}$$

where $\mathrm{K_{p\omega}}$ is the proportional gain of the speed regulator, $\mathrm{K_{i\omega}}$ is the integral gain of the speed regulator and τ is the time constant of the DC drive motor. The integral and proportional gains are tuned in this work using the Ziegler-Nichols rules [Astrom95].

2.3.3 Capacitor Banks and Conventional Transformers

The transients associated with the remaining components of the VFT park such as the conventional transformers and the capacitor banks can be neglected in order to obtain a set of algebraic equations. The transient associated to these components decays very rapidly and there is little justification for modeling their effects in transient stability studies [Kundur94]. Hence, the transformers' currents on the stator and rotor side of each WRIM can be computed applying Kirchhoff's current law at nodes V_s and V_r as follows,

$$\begin{bmatrix} I_{qTs,i} \\ I_{dTs,i} \end{bmatrix} = \begin{bmatrix} 0 & \omega_s^e \mathrm{C}_{s,i} \\ -\omega_s^e \mathrm{C}_{s,i} & 0 \end{bmatrix}\begin{bmatrix} V_{qs,i}^e \\ V_{ds,i}^e \end{bmatrix} + \begin{bmatrix} I_{qs,i}^e \\ I_{ds,i}^e \end{bmatrix} \tag{2.17}$$

$$\begin{bmatrix} I_{qTr,i} \\ I_{dTr,i} \end{bmatrix} = \begin{bmatrix} 0 & \omega_r^e \mathrm{C}_{r,i} \\ -\omega_r^e \mathrm{C}_{r,i} & 0 \end{bmatrix}\begin{bmatrix} V_{qr,i}^e \\ V_{dr,i}^e \end{bmatrix} + \begin{bmatrix} I_{qr,i}^e \\ I_{dr,i}^e \end{bmatrix} \tag{2.18}$$

where C_s is the capacitance at the stator side and C_r is the capacitance at the rotor side. The voltages at the points of common coupling (PCC) V_{pc1} and V_{pc2} can be expressed algebraically by applying Kirchhoff's voltage law on the stator and rotor sides as follows,

$$\begin{bmatrix} V_{q\mathrm{pc1}} \\ V_{d\mathrm{pc1}} \end{bmatrix} = -\begin{bmatrix} r_{\mathrm{Tpc1}} & x_{\mathrm{Tpc1}} \\ -x_{\mathrm{Tpc1}} & r_{\mathrm{Tpc1}} \end{bmatrix}\begin{bmatrix} \sum_{i=1}^{n} I_{qTs,i} \\ \sum_{i=1}^{n} I_{dTs,i} \end{bmatrix} + \begin{bmatrix} V_{qk} \\ V_{dk} \end{bmatrix} \tag{2.19}$$

$$\begin{bmatrix} V_{q\mathrm{pc2}} \\ V_{d\mathrm{pc2}} \end{bmatrix} = -\begin{bmatrix} r_{\mathrm{Tpc2}} & x_{\mathrm{Tpc2}} \\ -x_{\mathrm{Tpc2}} & r_{\mathrm{Tpc2}} \end{bmatrix}\begin{bmatrix} \sum_{i=1}^{n} I_{qTr,i} \\ \sum_{i=1}^{n} I_{dTr,i} \end{bmatrix} + \begin{bmatrix} V_{qm} \\ V_{dm} \end{bmatrix} \tag{2.20}$$

where I_{qTs} is the quadrature-axis current through the conventional transformer connected to WRIM at the stator side, I_{dTs} is the direct-axis current through the conventional transformer connected to WRIM at the stator side, I_{qTr} is the quadrature-axis current through the conventional transformer connected to WRIM at the rotor side, I_{dTr} is the direct-axis current through the conventional transformer connected to WRIM at the rotor side, V_{qk} is the quadrature-axis voltage at power systems k, V_{dk} is the direct-axis voltage at power systems k, V_{qm} is the quadrature-axis voltage at power systems m and V_{dm} is the direct-axis voltage at power systems m. In addition, r_{Tpc1} and x_{Tpc1} are the resistance and reactance of the power transformer connected at power network k, while r_{Tpc2} and x_{Tpc2} are the resistance and reactance of the power transformer connected at power network m.

The new values for voltages V_s and V_r at each WRIM to be used in the next integration step can be computed applying Kirchhoff's voltage law. Then,

$$\begin{bmatrix} V^e_{qs,i} \\ V^e_{ds,i} \end{bmatrix} = -\begin{bmatrix} r_{\mathrm{T}s} & x_{\mathrm{T}s} \\ -x_{\mathrm{T}s} & r_{\mathrm{T}s} \end{bmatrix} \begin{bmatrix} I_{qTs,i} \\ I_{dTs,i} \end{bmatrix} + \begin{bmatrix} V_{q\mathrm{pc1}} \\ V_{d\mathrm{pc1}} \end{bmatrix} \tag{2.21}$$

$$\begin{bmatrix} V_{qr,i} \\ V_{dr,i} \end{bmatrix} = -\begin{bmatrix} r_{\mathrm{T}r} & x_{\mathrm{T}r} \\ -x_{\mathrm{T}r} & r_{\mathrm{T}r} \end{bmatrix} \begin{bmatrix} I_{qTr,i} \\ I_{dTr,i} \end{bmatrix} + \begin{bmatrix} V_{q\mathrm{pc2}} \\ V_{d\mathrm{pc2}} \end{bmatrix} \tag{2.22}$$

where $r_{\mathrm{T}s}$ and $x_{\mathrm{T}s}$ are the resistance and reactance of the conventional power transformer connected at the stator side, $r_{\mathrm{T}r}$ and $x_{\mathrm{T}r}$ are the resistance and reactance of the conventional power transformer connected at the rotor side.

As a consequence, the VFT park is represented with 9 ODEs and 16 algebraic equations for the order 6 WRIM model. A total number of 7 ODEs and 16 algebraic equations are needed for the order 4 WRIM model. Finally, 5 ODEs and 16 algebraic equations are required with the order 2 WRIM model.

2.3.4 Validation of the WRIM

The dynamic solution obtained with the WRIM model implemented in this work is validated with a PSCAD/EMTDC simulation. While PSCAD-EMTDC uses a trapezoidal rule, in this work a Runge-Kutta fourth order is implemented. An induction machine of 2250 HP, 2300 V, 60 Hz, 1786 rpm with three-phase winding is connected at a balanced three-phase source. The parameters of the WRIM are summarized in appendix D. The initial condition of the state variables in the induction machine at $t = 0$ are $\mathbf{x}_0 = 0$.

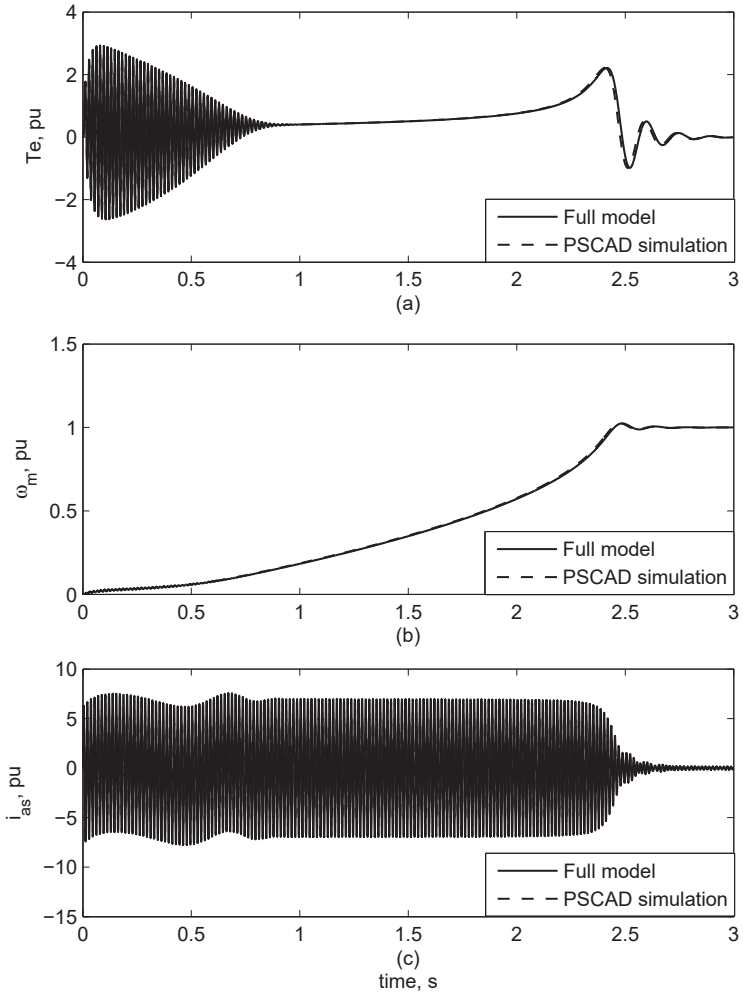

Figure 2.6: Start-up of a 2250 HP WRIM: (a).- electromagnetic torque, (b).- rotor speed and (c).- stator current phase *a*.

Figure 2.6 shows the electromagnetic torque, the rotor speed and stator current for phase *a* for the start-up of the induction machine using the full model implemented in this work and PSCAD/EMTDC software. Excellent agreement in terms of the transient solutions can be observed during the transient and steady-state solutions. It can be observed that the WRIM presents a large transient solution because of the rotor inertia of the rotary machine. For instance, it should be noted that the rotor speed of the rotary machine lasts nearly 2.5 seconds to reach the synchronous speed (see Figure 2.6 (b)). In addition, Figure 2.6 (c) shows that the inrush current at phase *a* on the stator side is nearly 7 pu.

With the WRIM operating in the steady-state at full load, a three-phase fault to

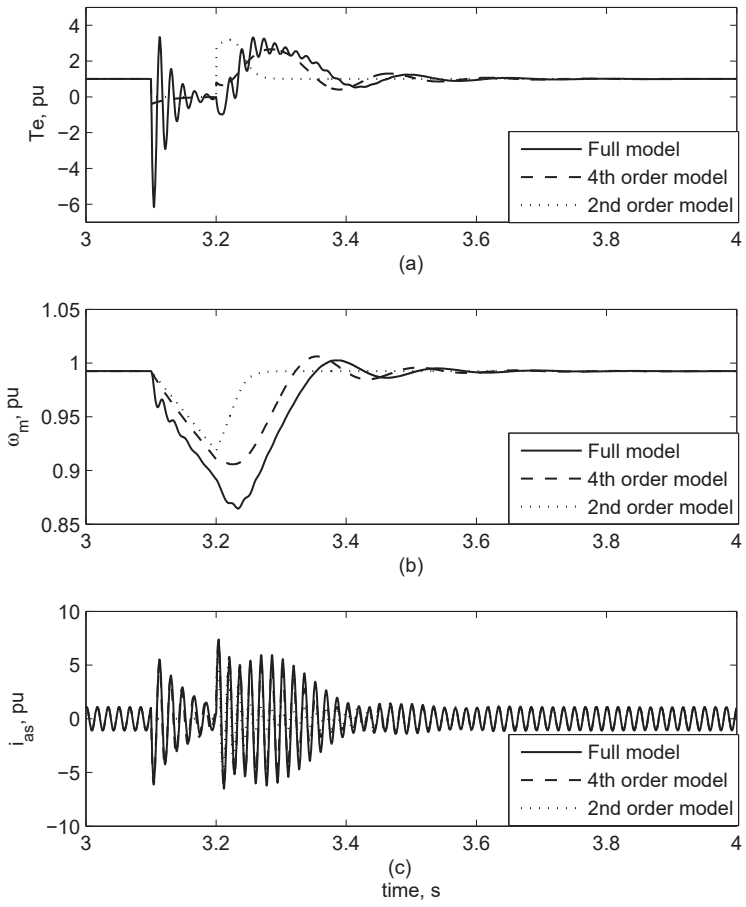

Figure 2.7: Transient solution after fault clearing for (a).- electromagnetic torque, (b).- rotor speed and (c).- stator current phase a.

ground is simulated on the stator side at $t = 3.1$ s and cleared after six cycles. Figure 2.7 shows the electromagnetic torque, the rotor speed and the stator current phase a of the WRIM when the three-phase fault takes place on the stator side. These results are reported using the $6th$, $4th$ and $2nd$ order models. As expected, discrepancies during transient are observed with the reduced models since the stator and rotor transients of the WRIM are neglected. However, no differences are observed at the steady-state solution before the three-phase fault and after fault clearing. It can be observed that the electromagnetic torque and the stator current at phase a present important transient values of nearly -6 pu and around ± 5 pu when the fault takes place, respectively. On the other hand, Figure 2.7 (b) reports a reduction to 0.87, 0.91 and 0.93 in the

rotor speed during fault for the full model, fourth order model and second order model, respectively. Besides, it shuld be noted that the transient dies out in approximately 0.6 seconds (see Figure 2.7).

2.4 Continuation Scheme for Stability Analyses

The stability of a steady-state solution can be studied using continuation schemes and eigenvalues analysis. While the continuation scheme shows how solutions of a system vary with a certain parameter, eigenvalues analysis determine the stability of the solutions. A continuation method can be implemented using a sequential continuation, a Davidenko Newton-Raphson or a pseudo-arclength approach. These methods rely on a predictor-corrector approach to follow a branch of solutions or a piece-wise-linear curve that approximates a branch of solutions [Nayfeh95].

2.4.1 Characteristic Multipliers and Equilibrium Points

The characteristic multipliers can be considered a generalization of the eigenvalues at an equilibrium point. As a consequence, characteristic multipliers can be used to find the stability of equilibrium points as well as the stability of limit cycles [Parker89].

Let an autonomous system be defined as,

$$\dot{x} = f(x) \tag{2.23}$$

where $x(t) \in \mathbb{R}$ and $\phi(t)$ represents the solution of (2.23).

Besides, a map $P : \mathbb{R} \rightarrow \mathbb{R}$ defines a discrete-time dynamical system by the state equation [Parker89],

$$x_{k+1} = P(x_k), \quad for\, k = 0, 1, 2... \tag{2.24}$$

Assume an equilibrium point x_{eq} of an autonomous system and consider any $T > 0$. Since the vector field of an autonomous system is independent of time, the autonomous system can be considered as a time-periodic, non-autonomous system with a non-minimum period T. Thus, the Poincaré map for the non-autonomous system $P_N(x) = \phi_T(x)$ is well defined and since $x_{eq} = P(x_{eq})$, then x_{eq} may be interpreted as a periodic solution [Parker89]. In order to determine the characteristic multipliers of this periodic solution, it is necessary to calculate the Poincaré map Jacobian [Parker89],

$$DP_N(x_{eq}) = \Phi_T(x_{eq}) \tag{2.25}$$

where Φ_T represents the transition matrix.

Due to the fact that $\phi_t(x_{eq}) = x_{eq}$, then the variational problem is defined as,

$$\dot{\Phi} = Df(x_{eq})\Phi \tag{2.26}$$

which represents a linear time-invariant system where Df is the Jacobian matrix of (2.23). The state transition matrix is represented as [Parker89],

$$\Phi_t(x_{eq}) = e^{Df(x_{eq})t} \tag{2.27}$$

In this research work, the transition matrix Φ_T associated to VFT models in the qd0 frame of reference are computed with the Newton method using a Direct Approach and a Numerical Differentiation method.

2.4.2 Methods for the Computation of the Steady-State Solution

The computation of transient and steady-state solutions of a VFT can be obtained numerically by repeatedly integrating a set of ODEs till the transient dies out. This alternative is known as Brute Force [Parker89] but it has an important drawback because it may require a considerable computational effort due to the inherently large inertia of its rotary machine, which may cause a prolonged transient response after a system disturbance. However, relevant contributions can be found in literature to overcome this problem. For instance, a shooting method to determine the steady-state response of nonlinear oscillators is presented in [Aprille72]. A frequency domain method based on the harmonic balanced concept is developed in [Nakhla76], which decreases its efficiency when a large number of state variables and harmonic terms are included in the solution. Besides, an acceleration procedure based on the Poincaré map and Newton algorithm to speedup the computation of the periodic steady-state solution of electric systems with nonlinear components is proposed in [Semlyen95]. This contribution reports a hybrid methodology, where the linear network is represented in the frequency domain, while nonlinear and time-varying components are represented in the time domain.

On the contrary, a variety of methods to determine the transient and steady-state

response on nonlinear systems have been developed by approximating the derivative and integral operators. The backbone of these methods relies on the transformation of a set of differential equations into a set of algebraic ones. In [Rico01], operational matrices have been used to study transient inrush currents in electric networks. A discrete-time method to compute the steady-state of nonlinear autonomous systems is presented in [Dalmau00], which is based on a Gear method and a polynomial fitting procedure. An extension of this method has been proposed in [López01] to determine the steady-state response of switched nonlinear circuits. In addition, a discrete-time representation of the derivative has been introduced in [Campos01] to locate limit cycles of non-autonomous systems, which consists basically in the substitution of the derivatives appearing in the differential equations by finite-dimensional matrices.

2.4.3 Sequential Continuation Scheme Using a Newton Method

The time domain representation of a non-linear electric system can be described as,

$$\dot{\mathbf{x}} = f(t, \mathbf{x}, \alpha),\ \mathbf{x}(t_0) = \mathbf{x}_0 \tag{2.28}$$

where $\mathbf{x}$ is a m-dimensional state vector and $\mathbf{x}_0$ is the initial condition.

A continuation scheme relies on the variation of the solutions of (2.28) defined as,

$$f(t, \mathbf{x}, \alpha) = 0 \tag{2.29}$$

where $\alpha \in \mathrm{M}$ is the continuation parameter and M is a parameter vector. The parameter α varies within an interval, which is divided into an equally spaced grid points $\alpha_0, \alpha_1, ..., \alpha_u$. The solution x_i at α_i is used as the predicted value for the solution x_{i+1} at α_{i+1}. This predicted value is corrected normally through a Newton-Raphson scheme.

In this section, a stability analysis based on a continuation scheme and eigenvalues analysis is implemented. The continuation method applies a sequential and predictor-corrector scheme, where the predicted value is corrected through the Newton method. More important, eigenvalues are computed with the transition matrix identified with the Newton method. Furthermore, the transition matrix and, therefore, eigenvalues are computed with a Direct Approach or a Numerical Differentiation procedure.

The direct approach procedure computes the transition matrix $\mathbf{\Phi}$ by integrating the Jacobian $J(t, x)$ associated to the system described by (2.29). A set of sequential perturbations are carried-out in order to determined the transition matrix by columns.

Each perturbation is defined with the column vectors of the identity matrix [Semlyen95]. On the other hand, a numerical differentiation approach calculates matrix $\mathbf{\Phi}$ by columns relying on the application of a sequential perturbation of the initial vector of the state variables calculated at the base cycle. This procedure has no need of evaluating the Jacobian matrix and only the set of ordinay differential equations that describes the dynamic behavior is necessary [Semlyen95]. Both approaches require the application of a conventional integration technique to identify the transition matrix by columns. Further details on the fundamentals of these procedures are given in Appendix A.

In order to check the stability of steady-state solutions, a well know procedure is used to compute and test stability as follows:

Step 1: Obtain the solution x_∞

Step 2: Compute the Poincaré map Jacobian $DP(x_\infty)$ at the steady-state solution

Setp 3: Evaluate the eigenvalues of $DP(x_\infty)$

The computation of the steady-state solution in Step 1 is usually done by integrating the system of equation from an initial state until the transient dies out. This option may be questioned because it may require extensive computing time. However, a Newton-Raphson method can be used to obtain the steady state solution in Step 1. In this thesis, the Newton-Raphson iteration involved in the Newton method is used to compute the steady-state solution as follows [Semlyen95],

$$x_\infty = x_i + (I - \Phi)^{-1}(x_{i+1} - x_i) \tag{2.30}$$

Note that the transition matrix Φ provided by the Newton method represents the Jacobian matrix of the Poincaré map DP. This means that the steady state solution x_∞ obtained in Step 1 and the transition matrix in Step 2, are computed at the same time. As a consequence, the stability of the solution x_∞ can be checked by evaluating the eigenvalues of the transition matrix Φ in the Newton Raphson iteration once it converges.

In this thesis, two procedures are applied to determine the transition matrix Φ required to investigate the stability of a solution: a Direct Approach and a Numerical Differentiation. Both procedures rely on a sequential perturbation of the state variables at the steady state in order to identify the transition matrix by columns. While the Numerical Differentiation method requires the solution of the set of ordinary differential equations of the system, the Direct Approach uses the Jacobian matrix of the system.

The continuation scheme implemented in this work based on the Newton method

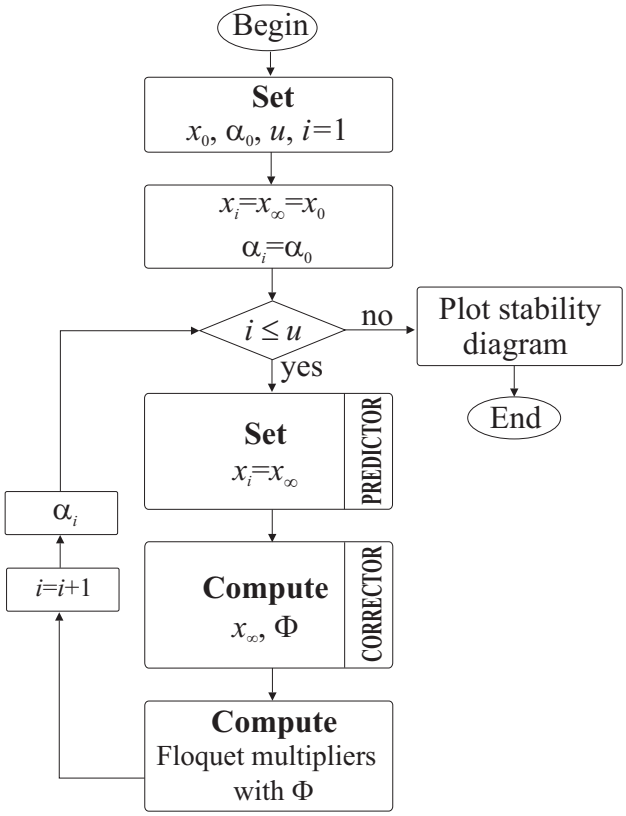

Figure 2.8: Continuation scheme based on the Newton method.

consists of major steps such as a parameterization strategy and a predictor-corrector scheme, as depicted in Figure 2.8. It can be appreciated that, as a first step, an initial steady-state solution x_0 is assumed for an initial scalar parameter α_0 and the initial predicted value is set with $\mathrm{x}_i = \mathrm{x}_\infty = \mathrm{x}_0$ at $\alpha_i = \alpha_0$. The parameter α_i is defined as,

$$\alpha_i = \alpha_0 + i \cdot \triangle\alpha \tag{2.31}$$

where $i = 1, 2, .., u$, α_0 is the initial condition for α and $\triangle\alpha$ is a pre-defined variation step.

In case a three dimensional stability diagram must be constructed, it is necessary to incorporate a second continuation parameter as follows,

$$\beta_j = \beta_0 + j \cdot \triangle\beta \tag{2.32}$$

where $j = 1, 2, .., v$, β_0 is the initial condition for β and $\triangle\beta$ is a pre-defined variation step.

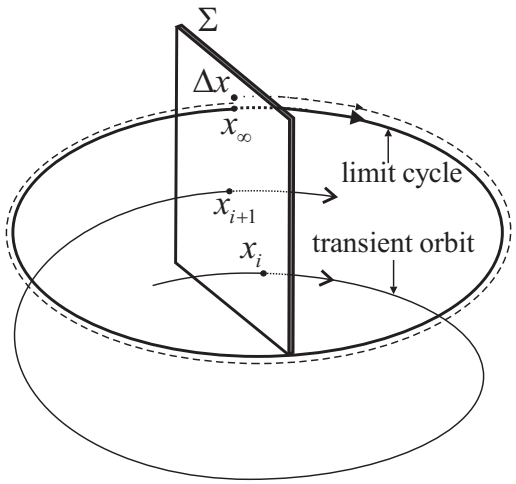

Figure 2.9: Single transient orbit on the Poincaré map.

The predicted value $x_{predictor}$ is defined as

$$x_{predictor} = x_i \tag{2.33}$$

The corrected value is obtained with the Newton method by computing the transition matrix Φ using a Direct Approach or a Numerical Differentiation procedures, and the state variables at the steady-state x_∞ (A.7), then

$$x_{corrector} = x_\infty \tag{2.34}$$

Once the steady-state is determined, eigenvalues can be computed using the transition matrix Φ defined with (A.11) or (A.15). This process is repeated for each grid point α_i for $i = 1, 2, .., u$. In this section, the periodic solution computed in the previous step is used as an initial guess for the periodic solution to be determined in the next step. Finally, eigenvalues are plotted to obtain the stability diagram.

Consider the fixed point x_∞ on the Poincaré map Σ (see Figure (2.9)). According to (A.4), the derivative of the perturbation Δx is approximated with,

$$\Delta \dot{x} \approx J(t, x)\Delta x \tag{2.35}$$

Then, the perturbation Δx evolves according to [Parker89],

$$\Delta x_i = \Phi(t, x)\Delta x_0 \tag{2.36}$$

where Φ is the transition matrix.

The evolution of a perturbation Δx in a neighborhood of the fixed point x_∞ is determined by (2.36). Therefore, the local behavior of the map for Δx_k is,

$$\Delta x_{k+1} = \Phi \Delta x_k \tag{2.37}$$

Let the eigenvalues of Φ be $\mu_i \in \mathbb{C}$ and the eigenvectors $\eta_i \in \mathbb{C}^m$, for $i = 1, ..., m$. Thus, the orbit of Σ with the initial condition $x_\infty + \Delta x_0$ is defined as [Parker89],

$$\begin{aligned} x_k &= x_\infty + \Delta x_i = x_\infty + \Phi^k \Delta x_0 \\ &= x_\infty + c_1 \mu_1^k \eta_1 + ... + c_m \mu_m^k \eta_m \end{aligned} \tag{2.38}$$

where $c_i \in \mathbb{C}$ are chosen according to the initial condition and x_∞ is the state variables at the steady-state. The eigenvalues $\{\mu_i\}$ of the transition matrix Φ determine the stability. When $|\mu_i| < 1$ for all μ_i, then any small perturbation converges toward 0 as $t \to \infty$ and x_∞ is asymptotically stable. For $|\mu_i| > 1$ for all μ_i, then any small perturbation grows with time and x_∞ is unstable. Given i and j such that $|\mu_i| < 1$ and $|\mu_j| > 1$, then x_∞ is non-stable.

2.5 Asynchronous Link Test Case

The VFT analysis is carried-out using a $qd0$ frame of reference. Figure 2.10 shows the test case used this section for power exchange between two asynchronous power grids. The VFT parameters used in this section are reported in the appendix D. Both power systems on the rotor and stator sides are simulated as infinite buses. The voltage of the systems are at 1.0 pu, and the angular difference between the two systems is 5 degrees. The controlled variable is the power exchange P_{VFT} through each VFT. The scenarios to be analyzed in this section are: *i*).- the steady-state operating point of a 300 MW VFT park, which is computed with the Newton method, *ii*).- the transient solution of a VFT park and *iii*).- the stability analyses of the VFT park are carried out with a sequential continuation scheme based on the Newton method and eigenvalues analysis. The set of equations that defined this test case are summarized in Appendix E.

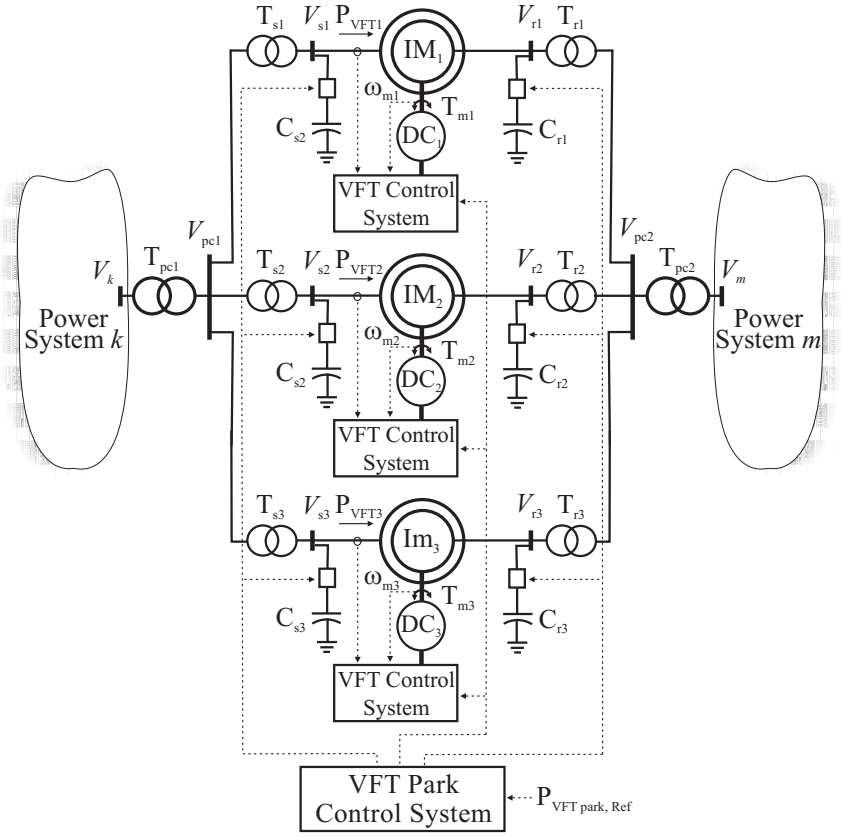

Figure 2.10: VFT park consisting of multi-unit VFTs.

2.5.1 Convergence to the Steady-State

The case study presented in this section consists of two asynchronous systems connected throughout a VFT park with three 100 MW VFT units. Besides, the VFT park is simulated with its rotor side connected to a power network of 59 Hz, while the power grid connected at its stator side has a frequency of 60 Hz. The power command (P_{cmd}) is set to 1.0 pu for each VFT unit in order to power exchange 300 MW in the VFT park. The steady-state operation of the 300 MW VFT park is studied for *i*).- the energization of the VFT units, *ii*).- a step power transfer and *iii*).- a three-phase fault on the rotor side. The maximum mismatch is set to 1×10^{-10} to locate the steady-state operating point of the VFT park. The energization of the VFT consists of assuming a power transfer across the VFT equal to zero and considering the initial conditions of all state variables set to zero. The computational effort is measured in a PC dual core at 1.73 GHz and 1GB RAM memory.

Table 2.1 summarizes the maximum mismatches during convergence to the steady-

Table 2.1: Errors during convergence to the steady-state operating point with the Direct Approach procedure.

NA	Energization			Power Transfer			Fault		
	6th order	4th order	2nd order	6th order	4th order	2nd order	6th order	4th order	2nd order
BC	3.2427e-2	7.8368e-2	1.9085e-2	2.7988e-2	2.7988e-2	2.7981e-2	8.1510e-3	2.1287e-2	6.2103e-3
1	4.6247e-3	7.3459e-3	2.4333e-4	3.9796e-3	1.0505e-2	1.3330e-4	6.9301e-4	1.8176e-3	3.2118e-4
2	1.0169e-4	4.6630e-5	3.8236e-6	1.5716e-5	6.8491e-5	2.0637e-5	4.3940e-6	2.6073e-5	1.2635e-5
3	1.2778e-6	3.0195e-6	1.1143e-7	2.9790e-8	1.3448e-6	1.5352e-7	1.3204e-7	2.7435e-7	2.5952e-7
4	1.5096e-8	1.2115e-8	2.6065e-9	6.189e-10	1.7314e-8	1.2336e-8	1.889e-10	1.2861e-8	9.0413e-9
5	4.738e-11	2.986e-10	6.499e-11	2.263e-12	4.257e-10	9.230e-11	3.617e-12	8.789e-11	8.124e-12
6		3.974e-12			6.628e-12				

state operating point using the Newton method and a direct approach procedure. The first column indicates the number of applications (NA) of the Newton-Raphson method required to achieve the steady-state solution after computing a base cycle (BC). The base cycle is determined by integrating the set of ordinary differential equations of the system during a number of cycles of integration. The number of cycles to be run depends on the characteristics of each test case. It can be appreciated that 5, 6 and 5 applications of the Newton method are required to reach the steady-state operating point for the energization case with the $6th$, $4th$ and $2nd$ order models, respectively. After the steady-state operating point is computed for the energization, the power transfer command is set to 100 MW for $\text{VFT}_{1,2,3}$, in order to transfer 300 MW from the system connected at stator side to system connected at rotor side. A new base cycle is computed after five cycles and 5, 6 and 5 applications of the Newton method are needed to reach the steady-state operating point with the $6th$, $4th$ and $2nd$ order models, respectively. Once the steady-state operating point for the power transfer scenario is computed, a three-phase fault is applied at the PCC of the rotor side and cleared after 6 cycles of integration. A new base cycle is determined after five cycles of integration and only 5 applications of the Newton method are needed to find the steady-state operating point. It can be appreciated that the computation of the steady-state operating point with the fourth order model required more applications than the $6th$ and $2nd$ order models for the energization and power transfer scenario.

On the other hand, Table 2.2 summarizes the maximum mismatches during convergence to the steady-state operating point using the Newton method implemented with a numerical differentiation procedure. It can be observed from Table 2.1 and Table 2.2 that similar results in terms of convergence and number of applications to

Table 2.2: Errors during convergence to the steady-state operating point with the Numerical Differentiation procedure.

NA	Energization			Power Transfer			Fault		
	6th order	4th order	2nd order	6th order	4th order	2nd order	6th order	4th order	2nd order
BC	3.2427e-2	7.8368e-2	1.9085e-2	2.7988e-2	2.7988e-2	2.7981e-2	8.1510e-3	2.1287e-2	6.2103e-3
1	4.6844e-3	6.0363e-3	1.5927e-5	3.9837e-3	1.0514e-2	1.3288e-4	6.8419e-4	1.6425e-3	6.2076e-6
2	1.0701e-4	5.5460e-5	6.3812e-6	1.5539e-5	6.2473e-5	1.8061e-5	3.9361e-6	1.9299e-5	4.5371e-6
3	1.2948e-6	2.2283e-6	7.2407e-9	3.7175e-8	1.4127e-6	6.0945e-8	7.2229e-8	2.6179e-7	2.8884e-9
4	1.6017e-8	1.4240e-8	3.5073e-9	6.516e-10	2.7268e-8	1.0368e-8	3.972e-10	8.0950e-9	2.5631e-9
5	3.750e-11	4.392e-10	4.000e-12	2.056e-12	4.616e-10	3.436e-11	2.340e-12	7.796e-11	1.667e-12
6		2.251e-12			1.022e-11				

Table 2.3: Speedup factors for the computation of the steady-state.

	Energization			Step command			Fault		
	6th	4th	2nd	6th	4th	2nd	6th	4th	2nd
DA	26	23	37	11	11	19	9	10	13
ND	31	43	43	15	16	21	11	13	15

the steady-state are observed with the numerical differentiation and direct approach methods.

The speed-up factors obtained with the Newton method to compute steady-state solution are summarized in Table 2.3. The speed-up factor for each operating scenario is computed with

$$\text{Speed up} = \frac{\text{T}_{\text{BF}}}{\text{T}_{\text{LCM}}} \tag{2.39}$$

where T_{BF} is the elapsed time needed by a Brute Force approach and T_{LCM} is the elapsed time required by the Newton method. Speedup factors reported in Table 2.3 are computed with T_{BF} equal to elapsed required by the Brute Force approach using the $6th$ order model. Speed-up factors up to 37 and 43 are obtained with the numerical differentiation and direct approach and a second order model, respectively. It can be appreciated that the numerical differentiation procedure is faster than the direct approach procedure due to the additional computational effort required to determine the Jacobian matrix involved in the direct approach procedure.

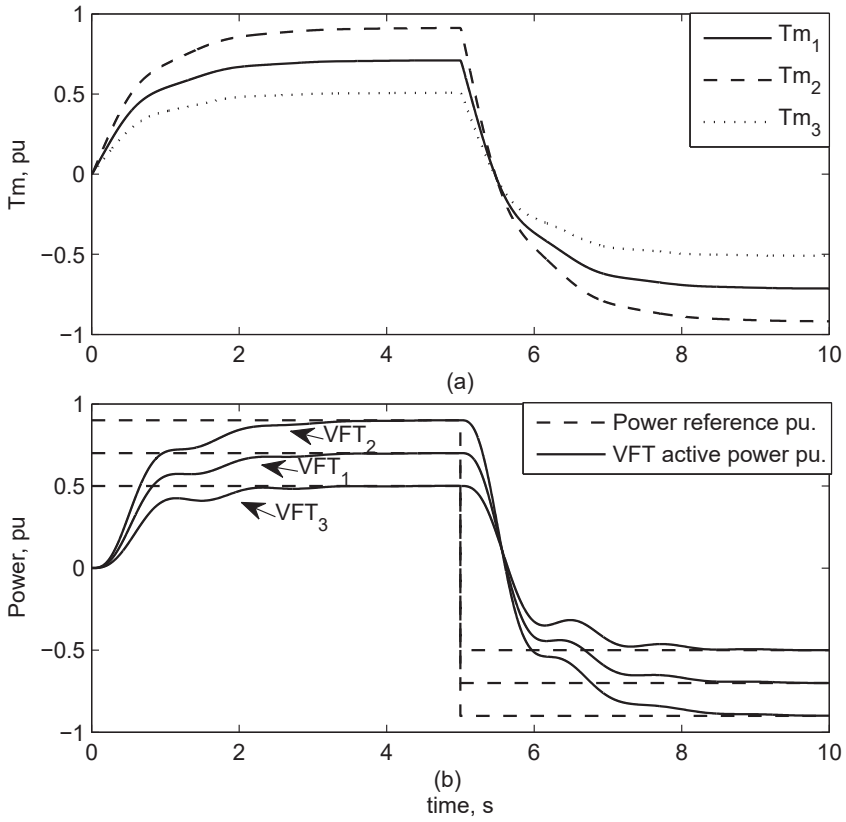

Figure 2.11: VFT responses to step power command for (a).- the mechanic torque and (b).- the active power flow.

2.5.2 Transient Solution

In this test case three VFT units are simulated with its rotor side connected to a power network of 59 Hz, while the power grid connected at its stator side has a frequency of 60 Hz. In order to study the transient solution obtained with the proposed control system, a step power command (P_{cmd}) and a power reversal of 0.7, 0.9 and 0.5 pu are applied to VFT_1, VFT_2 and VFT_3 at t=0 and t=5 seconds, respectively. Figure 2.11 (a) shows the mechanic torque drive provided by the speed drive, whilst Figure 2.11 (b) shows the active power flow response throughout each VFT. It can be observed that the transient settles down in approximately three seconds. This time delay in the response of the VFT is associated to the large inertia of its rotary machine.

On the other hand, Figures 2.12 (a) and (b) show the total active and reactive power exchange throughout the VFT park when a three-phase fault takes place at the PCC on the rotor side. Comparative results are reported with the $6th$, $4th$ and $2nd$

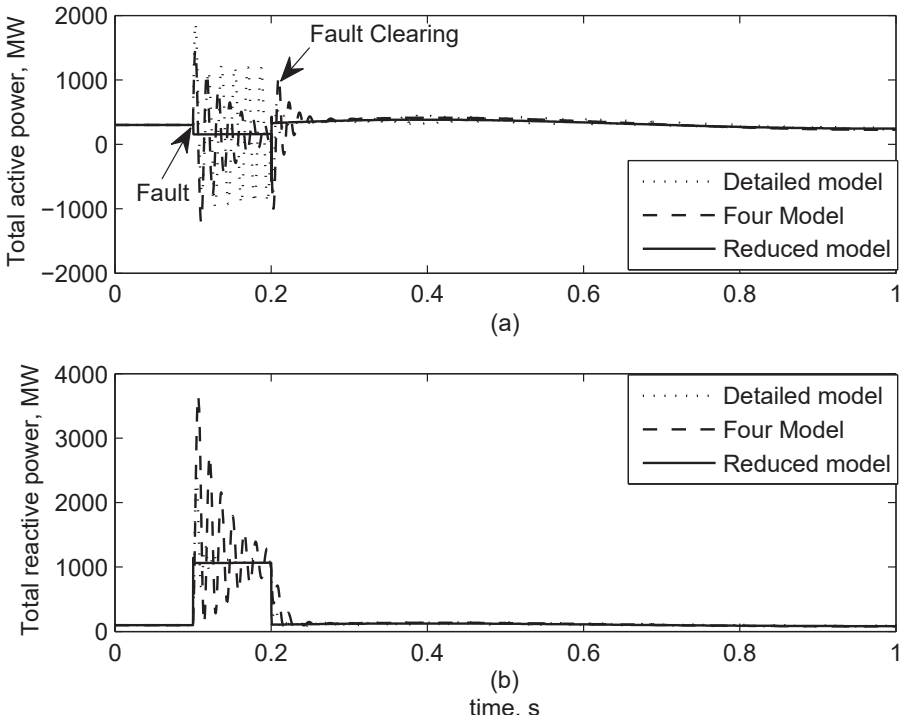

Figure 2.12: Transient behavior during fault for (a).- total active power and (b).- total reactive power.

order models. Figure 2.12 shows an oscillatory pattern during the transient for detailed model. Magnitudes up 1200 MW are observed for the oscillations in the detailed model during the transient. In the practical operation this operation mode is desirable not due to uncontrolled power transfer during the transient. As expected, discrepancies during transient are observed with the reduced model since the stator transient of WRIM has been neglected. However, no differences are observed at the steady-state operating point. Therefore, it is recommended to use the reduced model if only steady-state solutions are of interest. For the detailed dynamic analysis of the VFT operating under conditions such as sudden changes of power transfer, transient faults or switching components of the system it is suggested to use the detailed model. On the other hand, it can be observed that the power flows during the three-phase fault show an oscillatory behavior and large transient values of nearly 4 pu. These results have been reported previously in a dynamic performance study of the VFT control system during a three-phase fault using a real time simulator setup by General Electric [Nabb05]. Figure 2.13 shows the rotor speed and rotor position of VFT_1, where it can be appreciated a

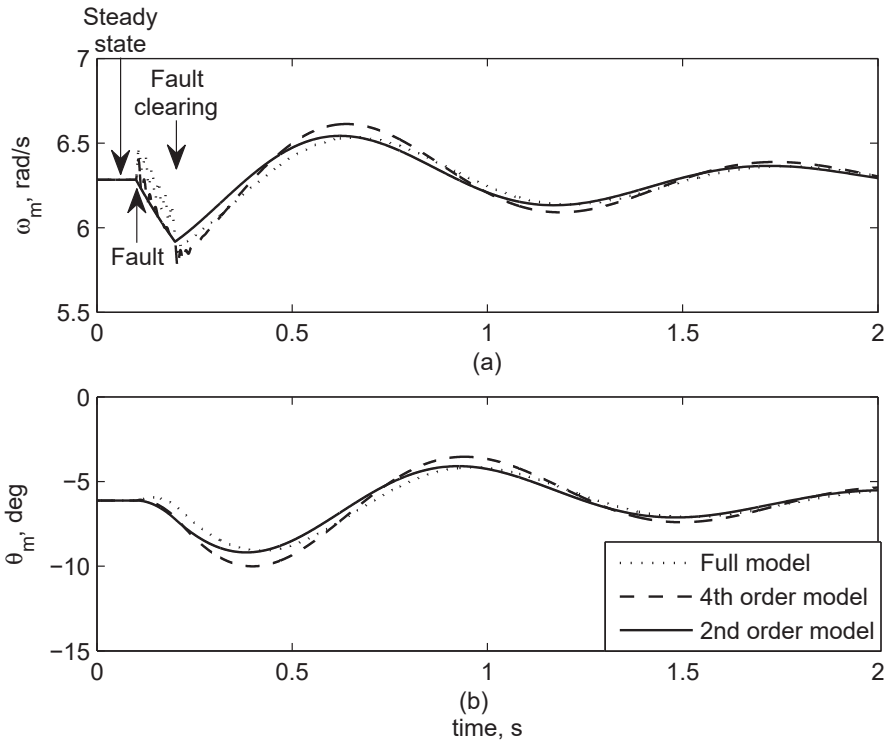

Figure 2.13: Transient solution after fault clearing for (a).- rotor speed and b).- rotor position.

transient solution during fault and a slow convergence to the steady-state after fault clearing. Similar results are obtained for the $\text{VFT}_{2,3}$. After the transient dies out the rotor speed and the rotor position return to their pre-fault steady-state solutions. Therefore, the steady-state solution after fault clearing for the rotor speed and the rotor position is $6.2833\,\frac{rad}{s}$ and 6.1198°, respectively (not shown in Figure 2.13).

2.5.3 Stability Analyses

In this section, the sequential continuation method based on the Newton method and eigenvalues analysis is applied to only one VFT unit of the VFT park model shown in Figure 2.10 in order to determine regions of stability. The effects on the stability of the VFT for changes on VFT and power system parameters are presented. The continuation parameters chosen in this section are the gains of the PI controllers, the VFT power transfer and the frequency of the asynchronous networks. From the point of view of the design of the control system of the VFT, the use of the gains of the PI controllers as continuation parameters may help to verify the adequate performance of

the control system.

Stability Regions in the Gains Plane

Figure 2.14 plots the stability regions of the VFT closed-loop control system for a power transfer command of -1, 0 and 1 pu, where $P_{VFT} = 0$ means that there is not power transfer across the VFT. While Figure 2.14 (a) presents the regions of stability when the proportional and integral gains of the PI power regulator are selected as continuation parameters, Figure 2.14 (b) shows the stability regions when varying the Kp and Ki gains of the speed regulator. The parameter K_{ip} is varied as follows,

$$K_{ip} = K_{ip0} + i \cdot \triangle K_{ip} \tag{2.40}$$

where $i = 1, 2, .., 240$, $K_{ip0} = 0$ and $\triangle K_{ip} = 0.0015$. The parameter K_{pp} is varied as follows,

$$K_{pp} = K_{pp0} + j \cdot \triangle K_{pp} \tag{2.41}$$

where $j = 1, 2, .., 210$, $K_{pp0} = 0$ and $\triangle K_{pp} = 6.8182e - 4$.

In addition, $K_{i\omega}$ varies as,

$$K_{i\omega} = K_{i\omega 0} + i \cdot \triangle K_{i\omega} \tag{2.42}$$

where $i = 1, 2, .., 240$, $K_{i\omega 0} = 0$ and $\triangle K_{i\omega} = 0.5$. The parameter $K_{p\omega}$ is defined as,

$$K_{p\omega} = K_{p\omega 0} + j \cdot \triangle K_{p\omega} \tag{2.43}$$

where $j = 1, 2, .., 210$, $K_{p\omega 0} = 0$ and $\triangle K_{p\omega} = 0.5$.

The direct approach and numerical differentiation procedures have been used to compute the transition matrix required to determine the eigenvalues analysis. Both methods provided similar results using WRIM models of order 6, 4 and 2. The continuous contours shown in Figure 2.14 represent the boundary between stable and no-stable regions of operation. It is observed from Figure 2.14 that changes in reference power transfer have a minor effect on the stability region in the gains plane. In addition, it must be brought to attention the fact that the nominal values of the PI gains shown in Figure 2.14 are associated to stable operating conditions of the test system.

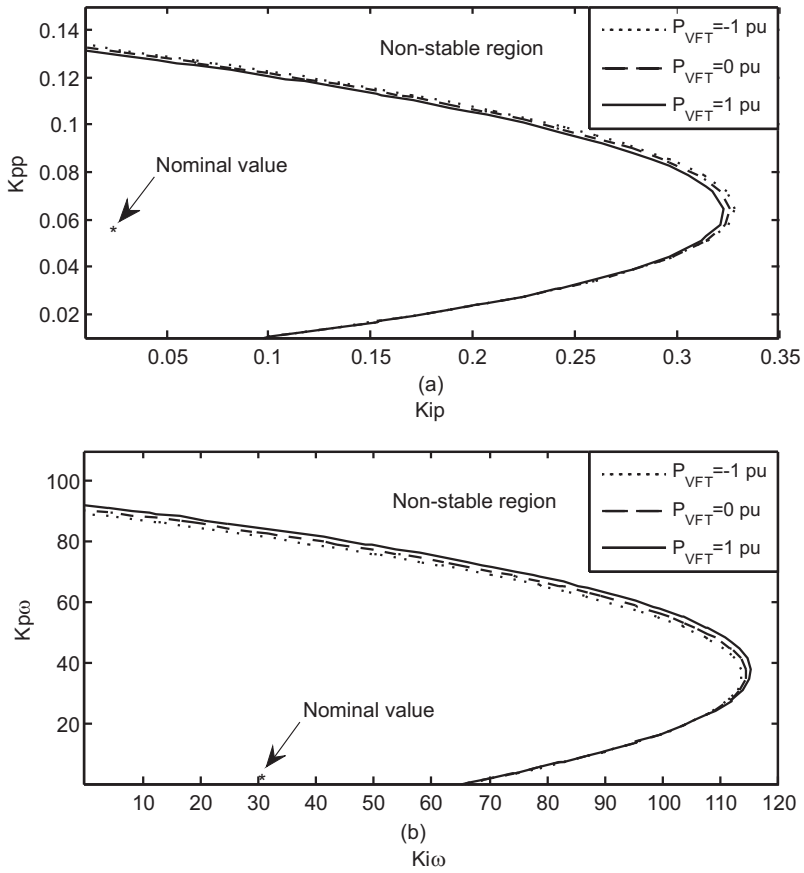

Figure 2.14: Stability regions for changes in the gains plane for a).- the power regulator and b).- the speed regulator.

Stability Regions in the Plane $\mathrm{P_{VFT}} - f$

In this section, stability regions in the plane $\mathrm{P_{VFT}} - f$ are reported for only one VFT unit of the VFT park model shown in Figure 2.10. For this experiment, three continuation parameters have been chosen: stator frequency f_s, rotor frequency f_r and the power transfer P_{VFT}. The parameter f_s is changed as follows,

$$f_s = f_{s0} + i \cdot \triangle f_s \tag{2.44}$$

where $i = 1, 2, .., 50$, $f_{s0} = 50$ and $\triangle f_s = 0.2$. The parameter f_r is varied as follows,

$$f_r = f_{r0} + j \cdot \triangle f_r \tag{2.45}$$

where $j = 1, 2, .., 50$, $f_{r0} = 50$ and $\triangle f_r = 0.2$. In addition, $\mathrm{P_{VFT}}$ varies as,

$$P_{VFT} = P_{VFT0} + k \cdot \triangle P_{VFT} \tag{2.46}$$

where $k = 1, 2, .., 50$, $P_{VFT0} = -3$ and $\triangle K_{i\omega} = 0.12$.

The contours shown in Figure 2.15 illustrate the effect upon VFT stability due to changes of frequency in the asynchronous networks (f_s and f_r) and changes of power transfer $\mathrm{P_{VFT}}$ for a phase-angle difference between interconnected power networks at 0 degrees. According to the three-dimensional plot shown in Figure 2.15 (a), two regions of instability are obtained when the frequencies f_s and f_r are varied from 50 to 60 Hz and $\mathrm{P_{VFT}}$ changes within the range ± 3 pu. Despite the fact that state-of-the-art of VFT installations have not been applied for interconnection of AC systems with large difference of frequencies or operating above its nominal capacity, it is important to determine the performance of the VFT under those scenarios. For instance, an interesting application would be the development of variable frequency electric power transmissions. Pioneering works on fractional frequency transmission have been reported in [Wang06] and [Funaki00]. It can be appreciated that the non-stable region **A** does not include the operating point $\mathrm{P_{VFT}} = 1.0$ pu (see Figure 2.15 (b) and (c)). However, the VFT may lay within the non-stable region **B** for $\mathrm{P_{VFT}} = -1.0$ pu if f_r is varied from 60 to 50 Hz.

In addition, Figure 2.16 shows the regions of instability for variations of frequency in the asynchronous networks (f_s and f_r) and changes of power transfer $\mathrm{P_{VFT}}$ for phase angle differences of 5 degrees. It can be appreciated that regions of instability **A** and **B** are indicated in this figure when frequencies f_s and f_r are varied from 50 to 60 Hz and $\mathrm{P_{VFT}}$ variations with the range ± 3 pu. Similar results are reported in Figure 2.15 for a phase angle difference equal to 0 degrees. However, it can be appreciated from Figures 2.15 and 2.16 that an increase in the phase-angle difference tends to decrease region of instability **A** and increase region of instability **B** within the interval $\mathrm{P_{VFT}} = \{1, -1\}$.

Furthermore, Figure 2.17 and 2.18 show a closer look to the top side of the three-dimensional stability diagram shown in Figure 2.16 (b). The dashed and dotted contours plotted in Figures 2.17 and 2.18 show the effect on the instability region when varying the rotor resistance and the magnetizing reactance, respectively. It can be appreciated that an increase of rotor resistance from the nominal value $r_r = 0.002$ to $r_r = 0.007$ pu produces an increase of the non-stable region **A** and reduces the non-stable region **B**. Therefore, an increase in rotor resistance tends to promote VFT stability within the power transfer margins $\mathrm{P_{VFT}} = \pm 1.0$ pu, whereas a decrease in rotor resistance results

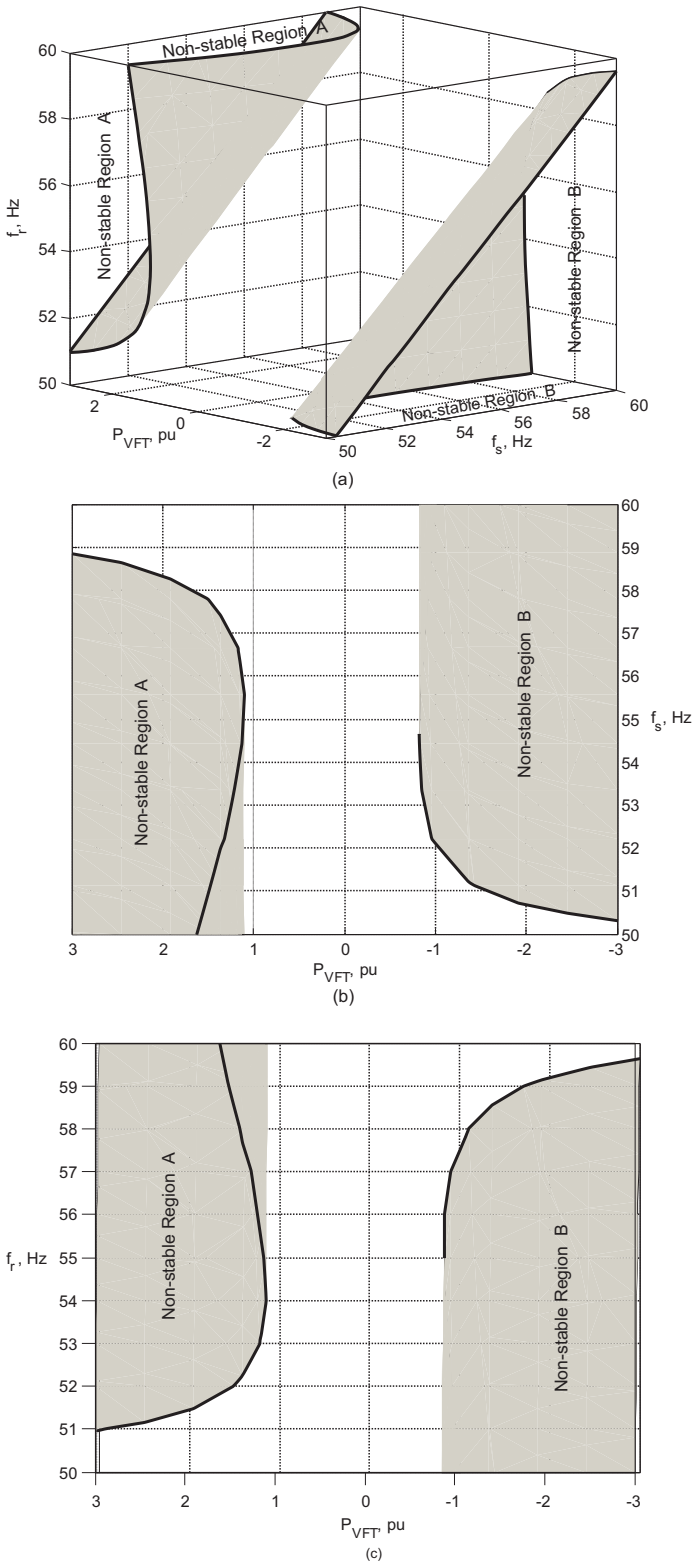

Figure 2.15: Stability regions for changes in the power transfer and frequency throughout VFT for a phase-angle difference of 0 degrees: (a).- three-dimensional representation, (b).- top side view with $f_r = 60$ Hz and (c).- front side view with $f_s = 60$ Hz.

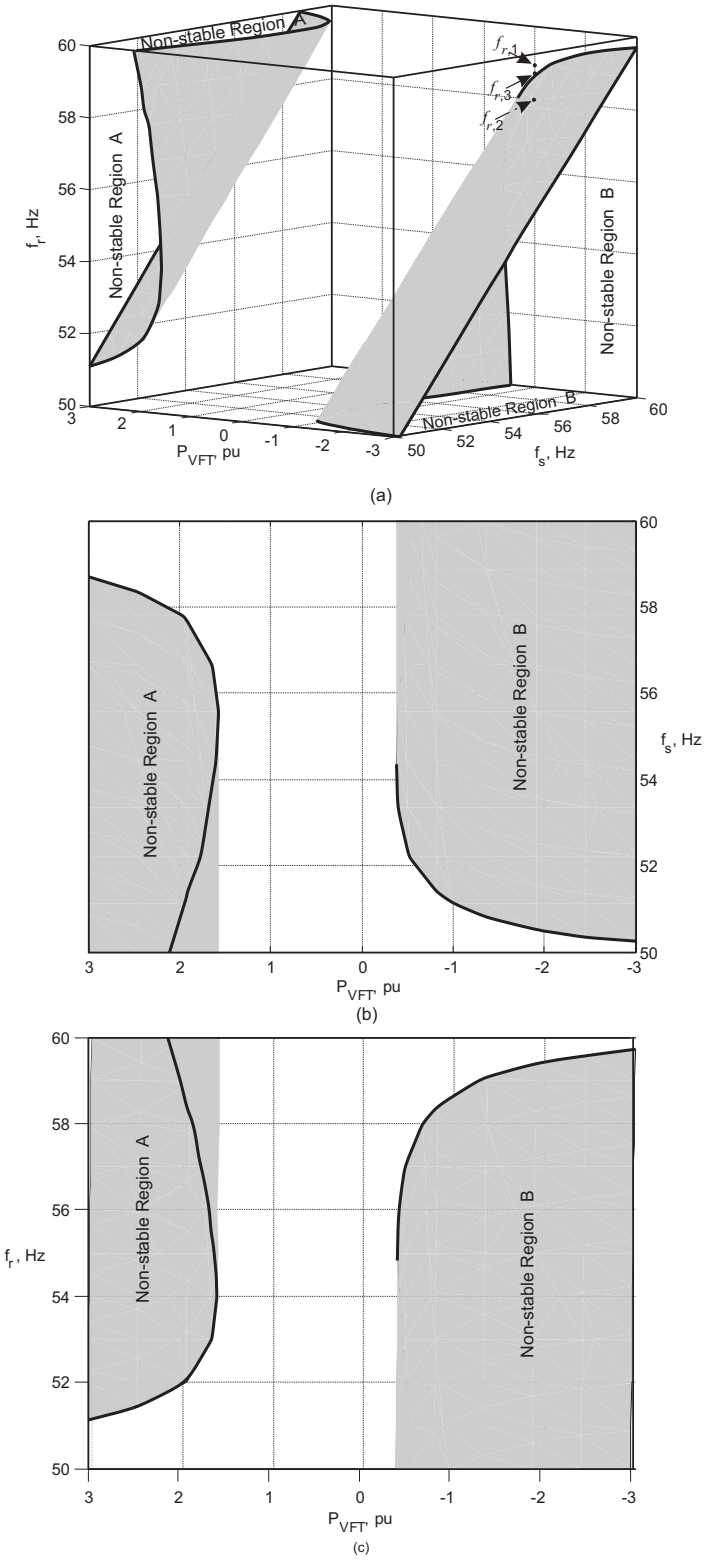

Figure 2.16: Stability regions for changes in the power transfer and frequency throughout VFT for a phase-angle difference of 5 degrees: (a).- three-dimensional representation, (b).- top side view with $f_r = 60$ Hz and (c).- front side view with $f_s = 60$ Hz.

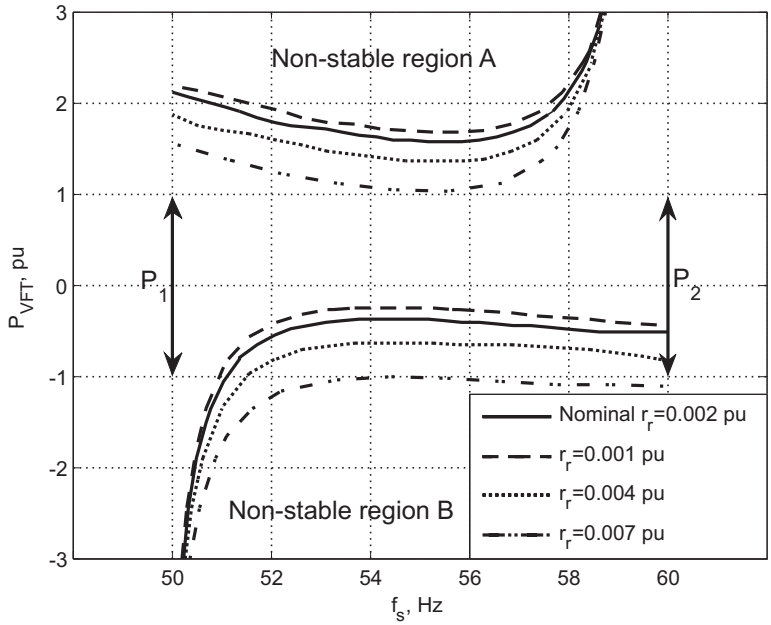

Figure 2.17: Stability regions for changes of rotor resistance.

in an increase in the region of instability. With $r_r = 0.007$ pu, the VFT is stable over all regions of operation within the range $\mathrm{P_{VFT}} = \pm 1.0$ pu. On the contrary, a decrease of the magnetizing reactance from the nominal value 5.6 to 1.6 pu tends to decrease the regions of instability **A** and **B** (see Figure 2.18). However, these contours show a more pronounced reduction of the region of instability **A** than the region of instability **B** for a decrease of the magnetizing reactance. A small magnetizing reactance results in the disappearance of the instability region **A**.

The simulation results summarized in Figure 2.17 and 2.18 indicate that the VFT can be used to link two power systems with frequencies of 50 and 60 Hz. The set of operating points identified as $\mathrm{P_1}$ shows that the VFT park with $r_r = 0.002$ pu can operate within a stable region for $\mathrm{P_{VFT}} = \pm 1.0$ pu, $f_s = 50$ Hz and $f_r = 60$ Hz (see Figure 2.17). Nevertheless, Figure 2.17 reveals that the VFT with $r_r = 0.002$ pu may operate within the non-stable region **B** for $f_s = 60$ Hz, $f_r = 50$ Hz and $\mathrm{P_{VFT}} = \pm 1.0$ pu (set of operating points $\mathrm{P_2}$). More specifically, the VFT operates within the stable region for the power transfer range $\mathrm{P_{VFT}} = \{1\,\mathrm{pu}, -0.6\,\mathrm{pu}\}$ but its operation within the range $\mathrm{P_{VFT}} = \{-0.6\,\mathrm{pu}, -1\,\mathrm{pu}\}$ will cause unbounded increases of oscillation. Consequently, it appears from Figures 2.16, 2.17 and 2.18 that the VFT is more likely to fall into a non-stable region if the power system connected to the

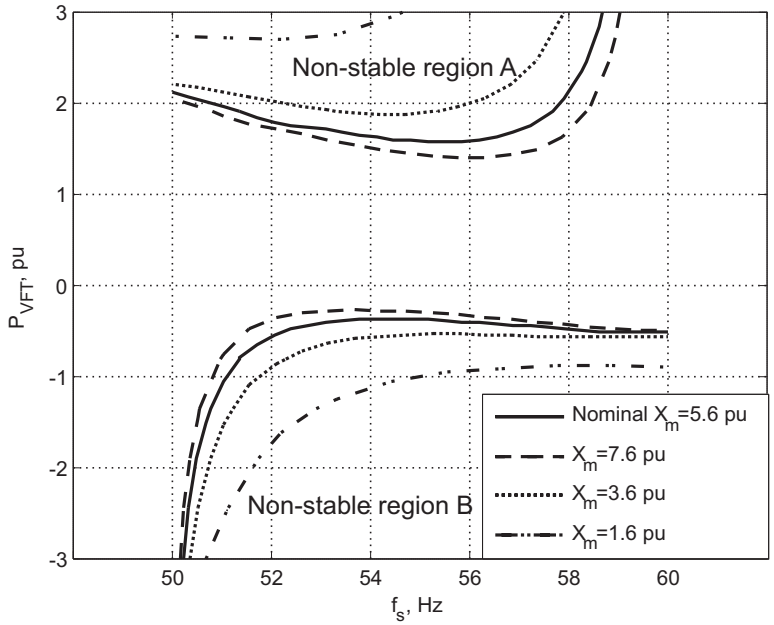

Figure 2.18: Stability regions for changes of magnetizing reactance.

rotor side presents wide range changes of frequency. In addition, it should be noted that Figures 2.17 and 2.18 are useful for the design of the VFT. It can be observed that variations on the resistance and magnetizing reactance due to variations of temperature have a large influence on the stability of the VFT. Despite the fact that most power networks show small frequency variations, it is of interest to investigate the operation of the VFT for future applications with a wider range of frequencies.

It is of interest to compare the results reported in Figures 2.16, 2.17 and 2.18 to the time domain solution of the VFT unit. The digital solution of one VFT unit for step changes in frequency is shown in Figure 2.19 for the active power, reactive power and rotor position. With the VFT initially operating in steady-state with $\mathrm{P_{VFT}} = -1.0$ pu, $f_s = 60$ Hz and $f_r = 59$ Hz, the rotor frequency is suddenly changed to $f_r = 58$ Hz at $t = 2$ seconds. This switching corresponds to a change from a stable operation point f_1 to a non-stable point of operation f_2, as shown in Figure 2.16. At $t = 40$ seconds the frequency f_r is switched to 58.8 Hz. This switching corresponds to a change from the non-stable operation point f_2 to a stable point of operation f_3 (see Figure 2.16). Once frequency f_r is changed to 58.8 Hz, the power flows and the rotor position show a prolonged transient solution and tend to reach a steady-state solution (see Figure 2.19). The steady-state solution for $f_r = 58.8$ Hz is not shown in Figure 2.19 becaused it is a

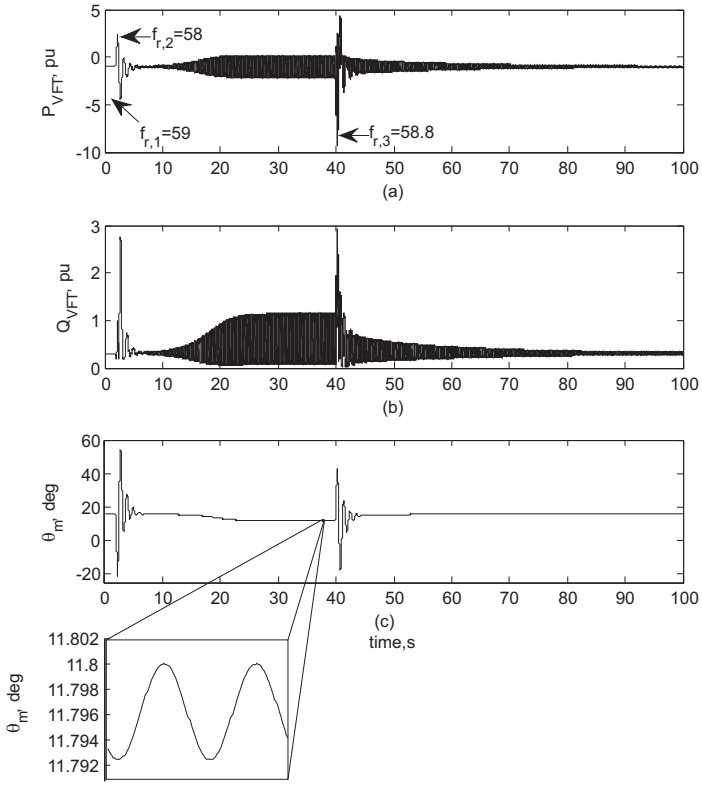

Figure 2.19: Transient solution during changes in the frequency of the rotor side with $f_s = 60$ Hz for a).- active power, b).- reactive power and c).- rotor position.

prolonged transient.

The steady-state operation of the VFT is shown in Figure 2.20 when the VFT operates with $\mathrm{P_{VFT}} = 1.0$ pu, $f_s = 60$ Hz and $f_r = 58$ Hz. The power transfer is suddenly changed to $\mathrm{P_{VFT}} = -1.0$ pu at $t = 2$ seconds, which corresponds to a change from a stable operating point to a non-stable point of operation in $\mathrm{P_2}$, as shown in Figure 2.17. The traces shown in Figure 2.20 illustrate that sustained oscillations will occur in the power transfer of the VFT. At $t = 70$ seconds the reference power transfer is switched to $\mathrm{P_{VFT}} = 0$ pu and, as a consequence, the closed-loop control system determines an operating point within the stable region.

Regarding the reactive power flow, Figure 2.19 (b) shows that the reactive power requirement of the VFT unit for rated power transfer is approximately 0.306 pu for stable operating points , $f_{r,1} = 59$ Hz and $f_{r,3} = 58.8$ Hz. The total reactive power consumption of the rotor and stator circuits is associated to the leakage and magnetizing reactances. Figure 2.19 (b) demonstrates that the reactive power consumed by the VFT shows minor variations for changes in the frequency of the rotor side at the

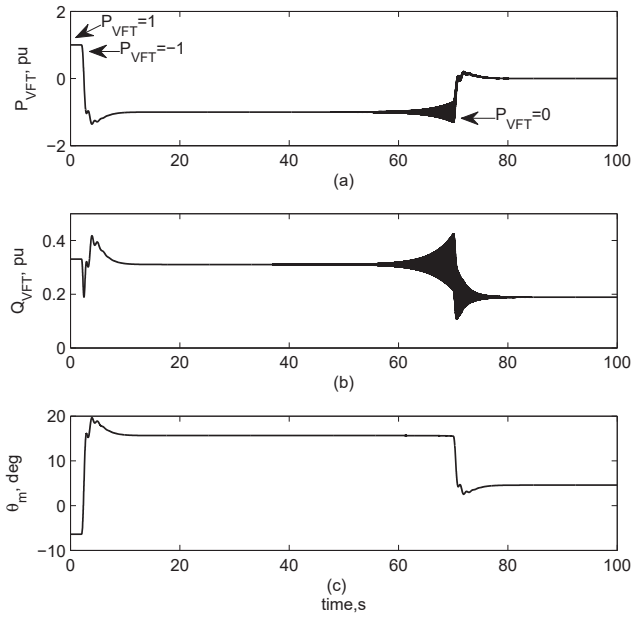

Figure 2.20: Transient solution during changes in the power transfer reference with $f_s = 60$ Hz and $f_r = 58$ Hz for a).- active power, b).- reactive power and c).- rotor position.

steady-state solution. However, it can be appreciated that important variations of active and reactive powers are observed during changes of the frequency on the rotor side. These transient variations on the active and reactive powers may be attenuated if dynamic VAR compensators such as SVC or a STATCOM are incorporated to the VFT installation. Similar results are observed for changes in the frequency of the stator side (not shown). A closer look to Figure 2.19 (c) shows that the rotor position is oscillates from 11.793 to 11.8 degrees. Nevertheless, a closer look to Figure 2.20 (b) shows that the reactive power is reduced from 0.331 pu to 0.189 pu for a power transfer modification from 1 pu to 0 pu. The total reactive power demanded by the VFT for $\mathrm{P_{VFT}} = 0$ is related to the magnetizing reactance of the rotary machine.

2.6 Conclusions

Stability analyses of variable frequency transformers based on a sequential continuation scheme, eigenvalues analysis and the Newton method have been presented in this chapter. The implementation of a predictor-corrector scheme and the computation of

eigenvalues based on the Newton method pave the way to carry-out efficient stability studies. Eigenvalues are computed with the transition matrix identified with the Newton method. A Direct Approach and Numerical Differentiation procedures have been applied to compute the transition matrix and, as a consequence, the eigenvalues. Besides, a comprehensive VFT park model consisting of a set of VFT units operated in parallel has been proposed. This VFT park model incorporates an alternative topology where a group of VFT operate in a coordinated fashion to improve the power transfer capacity of an asynchronous link. Each VFT unit comprises a WRIM, a DC motor, capacitor banks, conventional transformer and a control system. The VFT control system incorporates power and speed regulators in order to provide a mechanic torque drive. The steady-state operating point is computed for the energization, step command and fault on the rotor side of a VFT park with the Newton method using both direct approach and numerical differentiation procedures. Speed up factors up to 31 have been achieved with the Newton method and the numerical differentiation procedure for the location of the steady-state operating point. The computation of the stability regions of the VFT control system provides the system designer with valuable information for tuning the PI controller. Non-stable regions have been identified for changes of frequency of the asynchronous networks and power transfer. Sustained oscillations on the VFT power transfer have been observed when the VFT park operates in the non-stable region. Instability is very likely to occur in VFTs if the rotor circuit is connected to a weak power network showing variations of frequency. Based on the simulation results, it is recommended to connect the rotor side of the VFT to the power system that shows minor frequency variations.

Chapter 3

MODELLING AND ANALYSIS OF A VFT FOR HARMONIC-ORIENTED STUDIES

A review of the literaure on the application of an acceleration procedure based on a Newton method and the Poincare map [Semlyen95] reveals that this approach has been used to determine periodic steady-state solutions of a variety of nonlinear devices. However, one important aspect for the application of this procedure relies on the identification of a transition matrix. All the contributions found in literature apply a convencional integration routine in order to identity the transition matrix by applying a sequential perturbation to the state variables using a Numerical Differentiation or a Direct Approach. For instante, a Runge-Kutta integration routine has been applied to compute the steady-state solution using a hybrid methodology [Semlyen95], a nonlinear transformer [S.García00][S.García01], a synchronous machine [Rodriguez02], a small power network with nonlinear branches [Medina03], a UPFC [Segundo08a][Segundo08b], TSCs [García00] and electric arc furnaces [Medina98]. Furthermore, a Trapezodal Rule of integration has been applied to identify the transition matrix for a small test case [Garcia02] and large-scale electric systems using parallel processing [García04], TSCs [García00] and electric Networks with STATCOMS [Garcia05]. However, more sophisticated implicit integration routines with variable time step have been proposed recently in [Contreras07][Contreras08] in order to improve the effectiveness to compute the transition matrix.

3.1 Introduction

Modern power systems may contain several nonlinear devices, which may degrade the power quality supplied to customers. Harmonics occur due to equipment with non-linear characteristic such as transformers and fluorescent lamps and, nowadays, power electronics devices. In addition, nonlinear devices produce harmonic currents and, as a consequence, distorted voltages and currents, which can adversely impact the electric system performance in different ways. The problem of power quality has gained increasing importance due to the widespread use of power electronics and the use of lower signal levels in electronic equipment. To fully appreciate the impact of these nonlinear devices, there are two important concepts to bear in mind with regard to power system harmonics: *i*).- the nature of harmonic-current phenomena (operation in non-linear region) and *ii*).- the harmonic current and voltage propagation in the electrical network. Despite the fact that the VFT allows power exchange between two asynchronous links with no harmonic generation, its rotary machine and conventional transformers may show a nonlinear behavior associated to the saturation characteristic. For this reason, further harmonic-oriented studies are needed to study the interaction of the VFT with the power system.

In this Chapter, a nonlinear model of the VFT is developed in a phase-coordinate representation. The rotary machine is represented as a WRIM with its saturation effect incorpored on the magnetizing inductance. The control system includes power, speed and torque regulators in order to provide a mechanic torque drive on the VFT rotor shaft. Three-phase nonlinear conventional transformers and shunt capacitor banks are connected at the stator and rotor sides. A powerful blend based on the Newton method and an implicit integration algorithm is used to compute the periodic steady-state solution of the VFT. An Implicit Integration Algorithm (IIA) based on a numerical differentiation formulation and backwards differences to adjust the time step is used to overcome stiffness problems associated with the solution of the nonlinear VFT model.

3.2 Variable Frequency Transformer Model

The general configuration of the VFT model is shown in Figure 3.1, where it can be observed that the main components are the wound rotor induction machine, a drive system and DC motor to adjust the power flow throughout the VFT. Shunt capacitor banks at stator and rotor terminals to provide reactive power compensation, whilst conventional

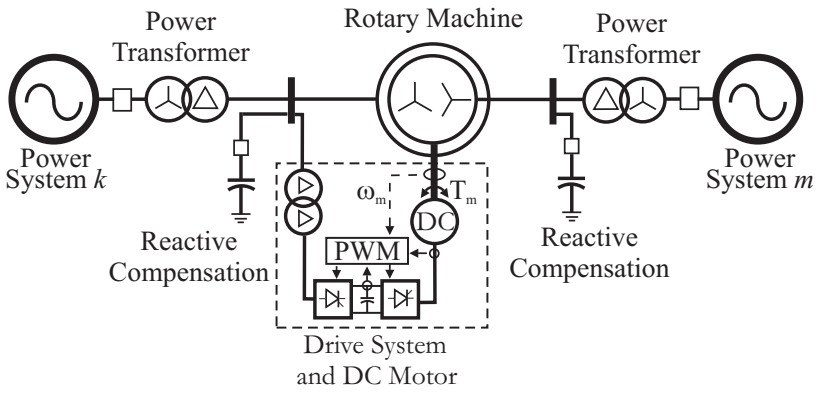

Figure 3.1: Variable frequency transformer configuration.

transformers link the wound rotor induction machine to the power networks.

3.2.1 Wound Rotor Induction Machine

Figure 3.2 shows the three-phase wound rotor induction machine implemented in this Chapter. Voltage equations for phases $a,\ b,\ c$ can be expressed as [Krause94],

$$\mathbf{v}_{s,r}^{abc} = \mathbf{r}_{s,r}\mathbf{i}_{s,r}^{abc} + \frac{1}{\omega_b}\frac{d}{dt}\boldsymbol{\psi}_{s,r}^{abc} \tag{3.1}$$

where the superscript abc denotes the phases of the system, the subscript s,r indicates the stator and rotor variables, $\boldsymbol{\psi}_{s,r}^{abc}$ are the stator and rotor flux linkage, $\mathbf{i}_{s,r}^{abc}$ are the stator and rotor currents, $\mathbf{r}_{s,r}$ are the stator and rotor resistances, $\mathbf{v}_{s,r}^{abc}$ are the stator and rotor voltages and ω_b is the base angular velocity. The flux linkages $\boldsymbol{\psi}$ can be related to the currents by means of the inductance matrix $\mathbf{L}$ as follows,

$$\boldsymbol{\psi}_{s,r}^{abc} = \mathbf{L}\cdot\mathbf{i}_{s,r}^{abc} \tag{3.2}$$

with

$$\mathbf{L} = \begin{bmatrix} \mathbf{L}_s & \mathbf{L}_{sr} \\ \mathbf{L}_{sr}^{\mathrm{T}} & \mathbf{L}_r \end{bmatrix} \tag{3.3}$$

and

$$\mathbf{L}_s = \begin{bmatrix} L_{ls}+L_m & -\frac{1}{2}L_m & -\frac{1}{2}L_m \\ -\frac{1}{2}L_m & L_{ls}+L_m & -\frac{1}{2}L_m \\ -\frac{1}{2}L_m & -\frac{1}{2}L_m & L_{ls}+L_m \end{bmatrix} \tag{3.4}$$

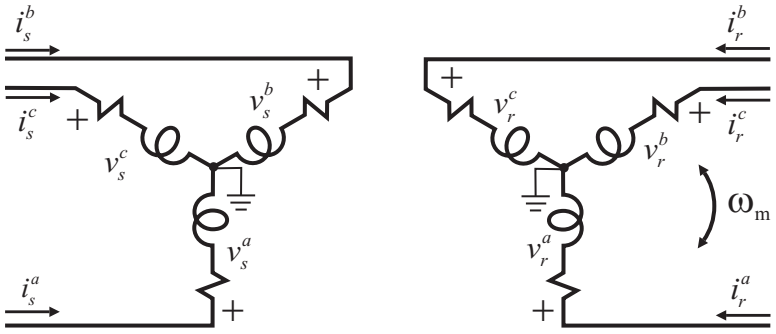

Figure 3.2: Equivalent circuit for three-phase, wye connected wound rotor induction machine.

$$\mathbf{L}_r = \begin{bmatrix} L_{lr} + L_m & -\frac{1}{2}L_m & -\frac{1}{2}L_m \\ -\frac{1}{2}L_m & L_{lr} + L_m & -\frac{1}{2}L_m \\ -\frac{1}{2}L_m & -\frac{1}{2}L_m & L_{lr} + L_m \end{bmatrix} \tag{3.5}$$

$$\mathbf{L}_{sr} = \begin{bmatrix} cos\theta_m & cos(\theta_m + \frac{2\pi}{3}) & cos(\theta_m - \frac{2\pi}{3}) \\ cos(\theta_m - \frac{2\pi}{3}) & cos\theta_m & cos(\theta_m + \frac{2\pi}{3}) \\ cos(\theta_m + \frac{2\pi}{3}) & cos(\theta_m - \frac{2\pi}{3}) & cos\theta_m \end{bmatrix} \tag{3.6}$$

where the inductances L_{ls}, L_{lr} and L_m are the stator leakage, rotor leakage indutances and magnetizing inductance, respectively. By combining (3.1) and (3.2) the next formulation in terms of current is obtained,

$$\mathbf{v}_{s,r}^{abc} = \mathbf{r}_{s,r}\mathbf{i}_{s,r}^{abc} + \frac{\omega_m}{\omega_b}\left[\frac{d}{d\theta_m}\mathbf{L}\right]\mathbf{i}_{s,r}^{abc} + \frac{1}{\omega_b}\mathbf{L}\left[\frac{d}{dt}\mathbf{i}_{s,r}^{abc}\right] \tag{3.7}$$

where $\mathbf{L}$ is the matrix of inductances, ω_m is the rotor speed and θ_m is the rotor position.

By defining the matrix

$$\mathbf{G}_{s,r} = \frac{\omega_m}{\omega_b}\left[\frac{d}{d\theta_m}\mathbf{L}\right] \tag{3.8}$$

then a set of ordinary differential equations for the stator and rotor currents in the wound rotor induction machine are described as,

$$\frac{d}{dt}\mathbf{i}_{s,r}^{abc} = \omega_b\left[\mathbf{L}^{-1}(\mathbf{v}_{s,r}^{abc} - (\mathbf{r}_{s,r} + \mathbf{G}_{s,r}) \cdot \mathbf{i}_{s,r}^{abc})\right] \tag{3.9}$$

The electromagnetic torque, rotor speed and rotor position associated to the mechanical equations are defined as follows [Krause94],

$$\mathrm{T_e} = \left(\frac{2}{3}\right) \mathbf{i}_s^{abc\mathrm{T}} \frac{\partial}{\partial \theta_m} [\mathbf{L}_{sr}] \mathbf{i}_r^{abc} \tag{3.10}$$

$$\frac{d}{dt}\left[\frac{\omega_m}{\omega_b}\right] = \frac{1}{2\mathrm{H}} \left(\mathrm{T_e} - \mathrm{T_m} - \mathrm{D_m}\omega_m\right) \tag{3.11}$$

$$\frac{d}{dt}\theta_m = \left[\frac{\omega_m}{\omega_b}\right] \omega_b \tag{3.12}$$

where $\mathrm{T_e}$ is the electromagnetic torque, H is the constant of inertia, $\mathrm{T_m}$ is the mechanic torque supplied by the control system and $\mathrm{D_m}$ is the damping coefficient.

3.2.2 Saturation Characteristic

The saturation effect in the induction machine is incorporated into the magnetizing rectance according to [Donescu99]. Taking into account that L_m depends mainly on the stator flux for low slip frequencies, then it is reasonable to consider the magnetizing inductance L_m as a function of a resultant stator flux ψ_s. Therefore, the resulting stator flux can be computed as a sum of the stator phase fluxes ψ_s^a , ψ_s^b and ψ_s^c obtained from (3.2) as follows,

$$\psi_s = \sqrt{\left(-\frac{\sqrt{3}}{2}\psi_s^b + \frac{\sqrt{3}}{2}\psi_s^c\right)^2 + \left(\psi_s^a - \frac{1}{2}\psi_s^b - \frac{1}{2}\psi_s^c\right)^2} \tag{3.13}$$

The saturation curve of magnetizing inductance is determined by interpolating a set of inductance measurements L_{m0}, L_{m1} and L_{m2} associated to the normalized stator flux ($\frac{\phi_\mathrm{s}}{\phi_\mathrm{rated}}$) equal to 0.2, 1.0, and 1.3, respectively (see Figure 3.3). The expression to interpolate the magnetizing inductance is defined as [Donescu99],

$$L_m(\psi_s) = \frac{L_{m0}}{1 + \alpha\psi_s^\beta} \tag{3.14}$$

where α and β are constants defined as,

$$\alpha = \frac{L_{m0}}{L_{m1}} - 1 \tag{3.15}$$

$$\beta = \frac{log(\frac{L_{m0}}{L_{m2}} - 1) - log(\alpha)}{log(1.30)} \tag{3.16}$$

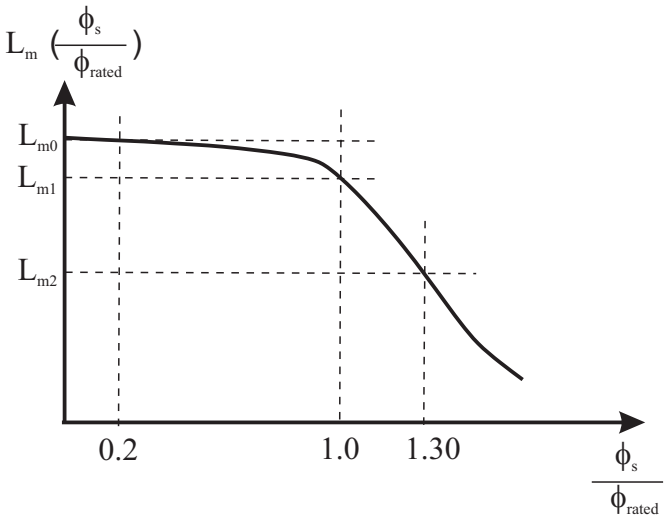

Figure 3.3: Magnetizing inductance versus normalized stator flux.

3.2.3 Control System and DC Drive Motor

Figure 3.4 illustrates an elementary control system for the VFT, which provides power regulation by adjusting the rotor speed and mechanic torque in the DC motor. The power regulator shown in Figure 3.4 measures the power flow throughout the VFT ($\mathrm{P_{VFT}}$) and compares it with a power reference ($\mathrm{P_{ref}}$). The error signal (e_p) is fed to a PI controller and its output represents a speed command (ω_cmd). This PI controller is defined as,

$$\frac{d}{dt}y_\omega = \mathrm{K_{ip}}\, e_\mathrm{p} \tag{3.17}$$

and the speed command

$$\omega_\mathrm{cmd} = y_\omega + \mathrm{K_{pp}}\, e_\mathrm{p} \tag{3.18}$$

where e_p is the power error signal, $\mathrm{K_{ip}}$ is the integral gain of the power regulator and $\mathrm{K_{pp}}$ is the proportional gain of the power regulator.

For the speed regulator shown in Figure 3.4, the error signal is determined by sustracting the speed command ω_cmd to the rotor speed ω_m. A PI controller determines the commanded torque $\mathrm{T_{cmd}}$ from the speed error signal e_ω and a torque limiter prevents the torque command to be within the DC motor capability. In this thesis, the rate of change of the driving torque command is allowed to take values between ± 5 pu. This PI controller is defined as,

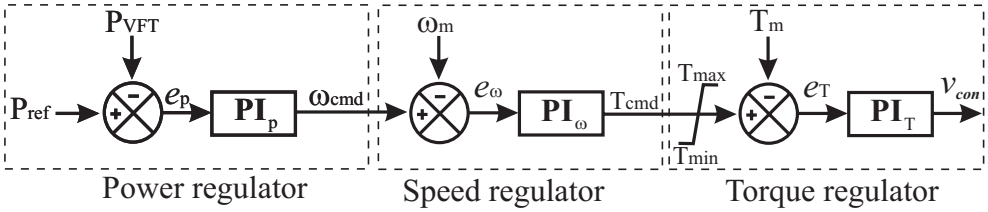

Figure 3.4: VFT control system.

$$\frac{d}{dt}y_{\mathrm{T}} = \mathrm{K_{i\omega}}\, e_{\omega} \tag{3.19}$$

and the torque command

$$\mathrm{T_{cmd}} = y_{\mathrm{T}} + \mathrm{K_{p\omega}}\, e_{\omega} \tag{3.20}$$

where e_{ω} is the speed error signal, $\mathrm{K_{i\omega}}$ is the integral gain of the speed regulator and $\mathrm{K_{p\omega}}$ is the proportional gain of the speed regulator.

A torque regulator determines the control voltage v_{con}, as shown in Figure 3.4. The torque error e_T is fed to a PI controller defined by,

$$\frac{d}{dt}y_v = \mathrm{K_{iT}}\, e_{\mathrm{T}} \tag{3.21}$$

and the control voltage

$$v_{con} = y_v + \mathrm{K_{pT}}\, e_{\mathrm{T}} \tag{3.22}$$

where e_{T} is the torque error signal, $\mathrm{K_{iT}}$ is the integral gain of the torque regulator and $\mathrm{K_{pT}}$ is the proportional gain of the torque regulator.

On the other hand, Figure 3.5 shows a DC motor drive system with its controllers based on Pulse-Width Modulation (PWM) converters. The Voltage Source Converter (VSC) is implemented with a three-phase six pulse rectifier neglecting losses in the semiconductor switches in the VSC. Then, the VSC model taking only the fundamental frequency signal may be represented by the following voltage and current relationships.

$$\begin{bmatrix} e_a \\ e_b \\ e_c \end{bmatrix} = V_{\mathrm{C}} \begin{bmatrix} Sw_a \\ Sw_b \\ Sw_c \end{bmatrix} \tag{3.23}$$

and

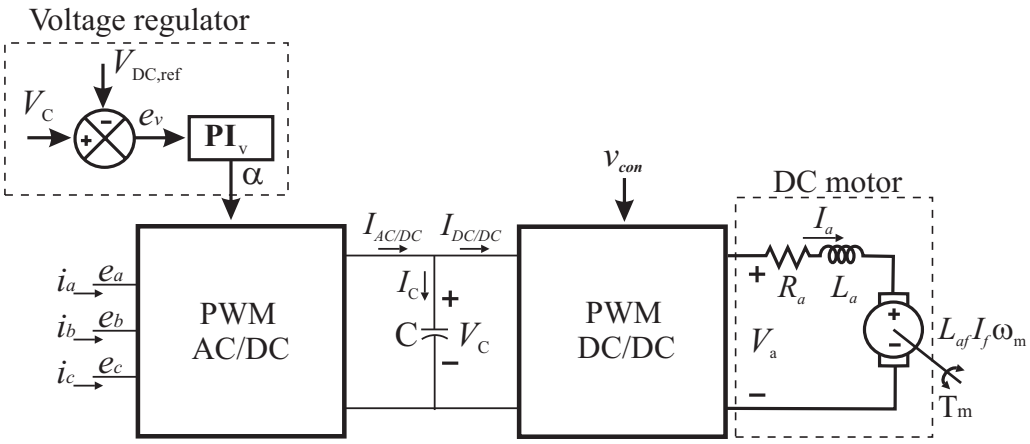

Figure 3.5: DC drive motor system.

$$I_{AC/DC} = \begin{bmatrix} i_a & i_b & i_c \end{bmatrix} \begin{bmatrix} Sw_a \\ Sw_b \\ Sw_c \end{bmatrix} \tag{3.24}$$

where the Sw are the PWM switching functions of each phase defined as,

$$\begin{bmatrix} Sw_a \\ Sw_b \\ Sw_c \end{bmatrix} = \frac{m_a}{2} \begin{bmatrix} sin(\omega_b t + \alpha) \\ sin(\omega_b t - \frac{2\pi}{3} + \alpha) \\ sin(\omega_b t + \frac{2\pi}{3} + \alpha) \end{bmatrix}, \tag{3.25}$$

m_a is the amplitude modulation ratio [Mohan95] and α is the PWM control angle.

The dynamic behavior of the capacitor connected at the DC-link is defined as,

$$\mathrm{C}\frac{d}{dt}V_{\mathrm{C}} = I_{\mathrm{C}} \tag{3.26}$$

where

$$I_{\mathrm{C}} = I_{AC/DC} - I_{DC/DC} \tag{3.27}$$

and

$$I_{DC/DC} = \frac{V_a I_a}{V_{\mathrm{C}}} \tag{3.28}$$

where C is capacitance of the DC-link, $\mathrm{V_C}$ is the voltage at the DC-link, V_a is armature voltage of the DC motor and I_a is armature current of the DC motor.

The capacitor voltage at the DC-link is controlled by the voltage regulator depicted in Figure 3.5. The capacitor voltage V_{C} is compared with a voltage reference $V_{\mathrm{DC,ref}}$ and a PI controller determines the phase angle α from the voltage error signal e_v. This voltage regulator is defined as,

$$\frac{d}{dt}y_{\mathrm{C}} = \mathrm{K_{i}}_{v}\, e_v \tag{3.29}$$

and the phase angle to control the capacitor voltage is,

$$\alpha = y_{\mathrm{C}} + \mathrm{K_{p}}_{v}\, e_v \tag{3.30}$$

where $\mathrm{K_{i}}_{v}$ is the integral gain of the voltage regulator and $\mathrm{K_{p}}_{v}$ is the proportional gain of the voltage regulator.

A full-bridge DC/DC converter controls the armature voltage V_a using a PWM scheme with bipolar voltage switching. The armature voltage is computed as [Mohan95],

$$V_a = \frac{V_{\mathrm{C}}}{v_{tri}} v_{con} \tag{3.31}$$

where v_{tri} is the peak value of sawtooth voltage.

Finally, the DC motor coupled to the shaft of the induction machine is modelled using a separately excited DC configuration [Truman07]. The circuit of the DC motor is described with one ordinary differential equation [Krause94],

$$L_a \frac{d}{dt} I_a = (V_a - R_a I_a - L_{af} I_f \omega_m) \tag{3.32}$$

and the mechanic torque is computed with,

$$\mathrm{T_m} = L_{af} I_f I_a \tag{3.33}$$

where L_a is inductance of the DC motor, R_a is resistance of the DC motor, L_{af} is the mutual inductance of the DC motor and I_f is the DC motor field current.

In this thesis, a single mass representation is considered for the VFT since all the VFT rotating components are located on its vertical rotor shaft. This consideration is usually adequate for hydro units, where turbine and generator are close together on a stiff shaft [Dommel94].

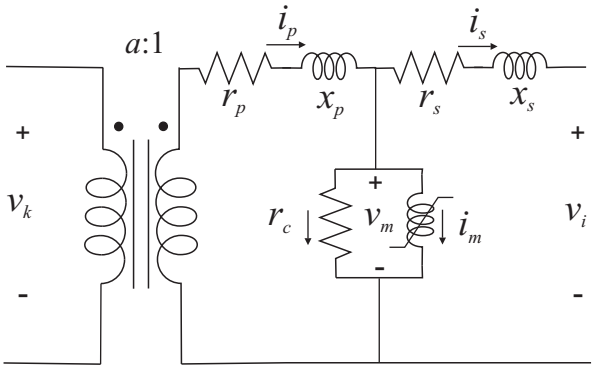

Figure 3.6: Equivalent circuit for single-phase transformer.

3.2.4 Conventional Transformers

Figure 3.6 shows the equivalent circuit for a single-phase transformer with core losses and its saturation characteristic. Three-phase transformers are modelled as three-phase wye-delta transformer banks with the wye connection solidly grounded. Applying Kirchhoff's laws and solving for currents at the primary side i_p and secondary side i_s, then the following equations are derived for one three-phase transformer [García04],

$$\frac{di_p^a}{dt} = \frac{\omega_b}{\mathrm{x}_p}\left[\frac{v_k^a}{a} - (r_p + r_c)i_p^a + r_c(i_s^a + i_m^a)\right] \tag{3.34}$$

$$\frac{di_p^b}{dt} = \frac{\omega_b}{\mathrm{x}_p}\left[\frac{v_k^b}{a} - (r_p + r_c)i_p^b + r_c(i_s^b + i_m^b)\right] \tag{3.35}$$

$$\frac{di_p^c}{dt} = \frac{\omega_b}{\mathrm{x}_p}\left[\frac{v_k^c}{a} - (r_p + r_c)i_p^c + r_c(i_s^c + i_m^c)\right] \tag{3.36}$$

$$\frac{di_s^a}{dt} = \frac{\omega_b}{\mathrm{x}_s}\left[-v_i^{ab} - (r_s + r_c)i_s^a + r_c(i_p^a - i_m^a)\right] \tag{3.37}$$

$$\frac{di_s^b}{dt} = \frac{\omega_b}{\mathrm{x}_s}\left[-v_i^{bc} - (r_s + r_c)i_s^b + r_c(i_p^b - i_m^b)\right] \tag{3.38}$$

$$\frac{di_s^c}{dt} = \frac{\omega_b}{\mathrm{x}_s}\left[-v_i^{ca} - (r_s + r_c)i_s^c + r_c(i_p^c - i_m^c)\right] \tag{3.39}$$

where a transformer ratio, r_p is the resistance at the primary side, r_s is the resistance at the secondary side, r_c is the resistance associated to core losses, i_m is the magnetizing current, x_p is the reactance at the primary side, x_s is the reactance at the secondary

side, v_k is the voltage at the primary side and v_i is the voltage at the secondary side.

Besides, the flux linkage associated with the nonlinear characteristic of the magnetic core can be expressed as,

$$\frac{d\psi_m^a}{dt} = \omega_b r_c(i_p^a - i_s^a - i_m^a) \tag{3.40}$$

$$\frac{d\psi_m^b}{dt} = \omega_b r_c(i_p^b - i_s^b - i_m^b) \tag{3.41}$$

$$\frac{d\psi_m^c}{dt} = \omega_b r_c(i_p^c - i_s^c - i_m^c) \tag{3.42}$$

where i_p^a and i_s^a are the currents at the primary side and secondary side, respectively. The nonlinear characteristic of the conventional transformer is defined with a polynomial representation [García04],

$$i_m^a = 0.000\,7\psi_m^a + 0.000\,83(\psi_m^a)^{19} \tag{3.43}$$

$$i_m^b = 0.000\,7\psi_m^b + 0.000\,83(\psi_m^b)^{19} \tag{3.44}$$

$$i_m^c = 0.000\,7\psi_m^c + 0.000\,83(\psi_m^c)^{19} \tag{3.45}$$

3.2.5 Shunt Reactive Compensators

The dynamic behavior of the three-phase wye capacitor banks connected at the stator and rotor sides of the VFT is defined as,

$$\frac{d}{dt}v^{abc} = \frac{1}{C}\sum i^{abc} \tag{3.46}$$

where C is the capacitance associated with the shunt compensator and $\sum i^{abc}$ is the total current flowing into the compensator for each phase.

3.2.6 Validation of Saturated WRIM

In this section the saturation characteristic of the VFT is incorporated by using and interpolation technique [Donescu99]. Figure 3.7 (a) shows the magnetizing inductance reported in [Merkhouf08] using finite-element field measurements for a VFT. This curve

was obtained from a field simulation carry-out for a four-pole machine rated 100 MW, 17 kV/17kV and 60 Hz. As it can be observed, the magnetizing reactance of the rotary transformer is plotted in terms of the terminal voltage in per unit. Therefore, the expression (3.13) proposed by [Donescu99] to define the saturation curve of the magnetizing inductance must be adequated in order to be a function of the terminal voltage.

Consider that the voltage drop on the stator and rotor resistances can be neglected during no power transfer operation of the WRIM. In addition, the voltage equation on the stator phases can be approximated with,

$$\mathbf{v}_{s,r}^{abc} = \frac{1}{\omega_b}\frac{d}{dt}\boldsymbol{\psi}_{s,r}^{abc} \tag{3.47}$$

Based on (3.47) and assuming a constant stator frequency, it can be consider that the phase voltage magnitude is proportional to the magnitude of the phase flux. Consequently, the stator flux magnitude is proportional to the stator voltage magnitude. Then, it can be considered that the magnetizing inductance dependence on the normalized stator flux is identical to its dependence on the normalized stator voltage [Donescu99]. Therefore, from (3.13) it follows that the resultant stator voltage can be described as a sum of the stator voltages v_s^a, v_s^b and v_s^c as,

$$v_s = \sqrt{\left(-\frac{\sqrt{3}}{2}v_s^b + \frac{\sqrt{3}}{2}v_s^c\right)^2 + \left(v_s^a - \frac{1}{2}v_s^b - \frac{1}{2}v_s^c\right)^2} \tag{3.48}$$

From Figure 3.7 (a), it is determined that $L_{m0} = 13.3$, $L_{m1} = 10.8$ and $L_{m2} = 3.15$ for $v_s = 0.2$, $v_s = 1.0$ and $v_s = 1.3$, respectively. Substituting in (3.15) and (3.16) it follows that $\alpha = 0.23$ and $\beta = 10$. Then, the expression to interpolate the magnetizing inductance (3.14) of the VFT in terms of the terminal voltage is defined as,

$$L_m(v_s) = \frac{L_{m0}}{1 + \alpha v_s^{\beta}} \tag{3.49}$$

Substituting α, β and L_{m0} yields,

$$L_m(v_s) = \frac{13.4}{1 + 0.23 v_s^{10}} \tag{3.50}$$

Figure 3.7 (b) shows the saturation curve of the magnetizing reactance reported in [Merkhouf08] (solid line) and the approximation proposed by (3.50) (dashed line). A

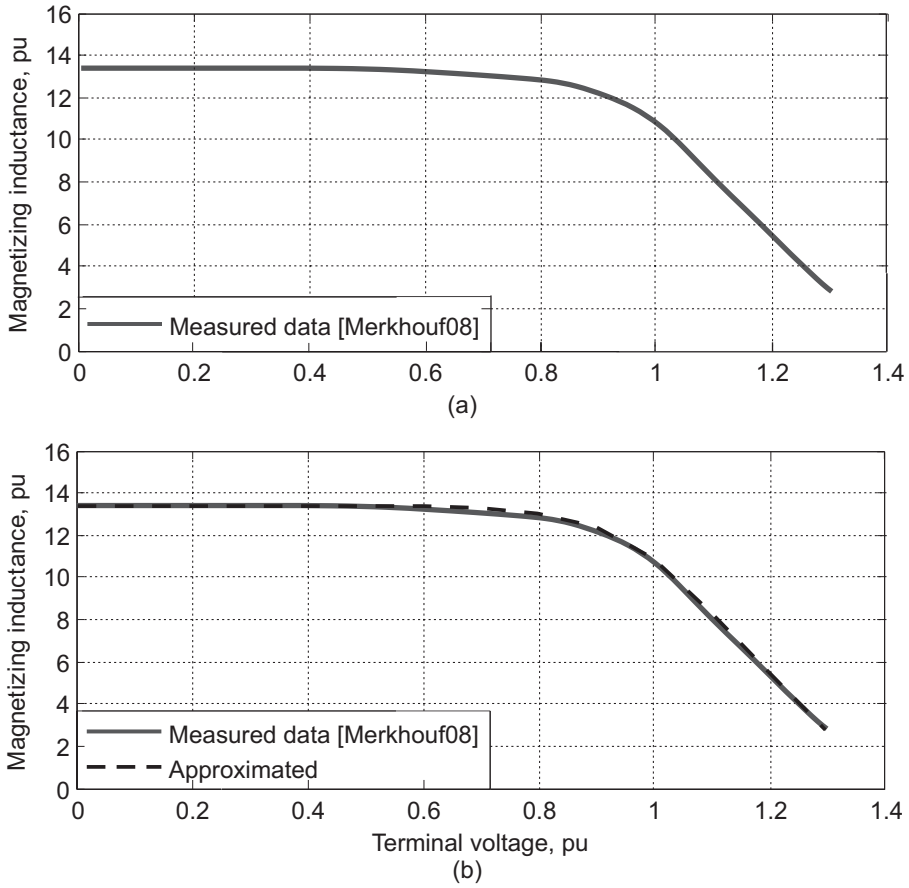

Figure 3.7: Magnetizing inductance of the VFT as a function of the voltage applied: (a).- measured magnetizing inductance and (b).- approximated inductance.

very good agreement can be appreciated with the interpolated magnetizing reactance proposed in this thesis.

On the other hand, the time domain solution obtained with the saturated WRIM model implemented in this work is validated with a PSCAD/EMTDC simulation. The WRIM is coupled to power sources on both stator and rotor sides in order to simulate the rotary machine of the VFT. The parameters used for this simulation are the nominal values of the VFT (see Appendix D). Figure 3.8 shows the stator currents for phases A,B,C for the saturated WRIM and PSCAD simulation during energization with no power transfer. Good agreement are observed during the transient solution and convergence to the steady-state.

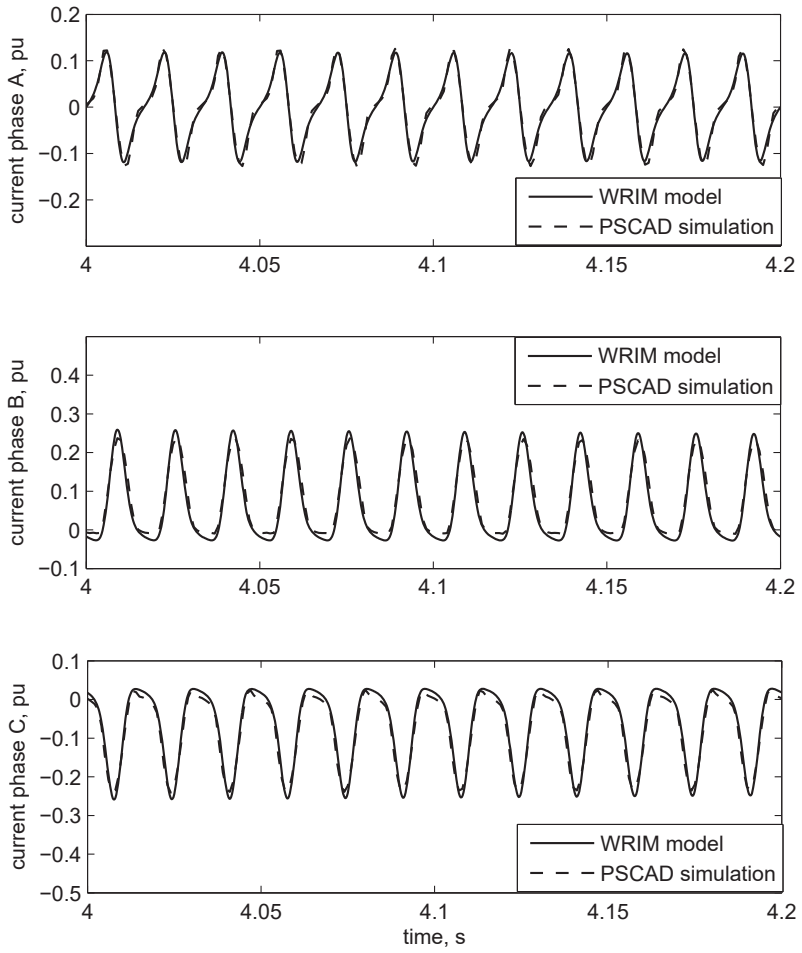

Figure 3.8: Time domain solution of stator currents for saturated WRIM model (solid line) and PSCAD simulation (dashed line).

3.3 Implicit Integration Algorithm for Stiff Systems

Stiffness appears on the modelling of VFT components because the time constants associated with two or more state variables differ by several orders of magnitude, i.e., the modelling of the nonlinear conventional transformer [Solodovnik98] [Contreras07].

Considering the linear system as,

$$\dot{x} = Ax \tag{3.51}$$

where A is a $m \times m$ matrix with eigenvalues λ_i for $i = 1, .., m$ are assumed distinct. Then the linear stiff system problem is defines as [Wean01],

$$Re(\lambda_i) < 0 \tag{3.52}$$

with

$$max|Re(\lambda)| \gg min|Re(\lambda)| \tag{3.53}$$

$$\frac{max|Re(\lambda)|}{min|Re(\lambda)|} = S \gg 1 \tag{3.54}$$

where S is the stiffness ratio that provided a measure of stiffness. Numerical instability is observed whether an unsuitable time step is selected to integrate stiff equations with an explicit integration method. The instability encountered can be overcome with the application of Implicit Integration Algorithms (IIA), such as higher-order methods for stiff systems based on generalizations of Runge-Kutta method, Bulirsch-Stoer method [Press02], Backward Differentiation and Numerical Differentiation Formulations [Shampine97]. The main advantage of IIA relies on adjusting the time step to preserve the stability of the integration methods involved in the solution of stiff problems. These algorithms dynamically reduce the time step when fast transients occur and increase it if the state variables change slowly.

In general, a stiff problem can be defined as

$$\mathbf{M}(t)\dot{\mathbf{x}} = f(t, \mathbf{x}) \tag{3.55}$$

where $\mathbf{M}(t)$ is a non-singular mass matrix, which can be transformed to the equivalent system,

$$\dot{\mathbf{x}} = F(t, \mathbf{x}) = \mathbf{M}^{-1}(t) f(t, \mathbf{x}) \tag{3.56}$$

Matrix $\mathbf{M}(t)$ is dependent on t and, therefore, an iterative Newton method involving the solution of a linear system is normally implemented to solve the stiff problem.

The implicit method used in this work is based on a Numerical Differentiation Formulation in terms of backward differences implemented in MATLAB libraries [Klopfenstein71] and an adjustable time step proposed in [Shampine97] (see Appendix B).

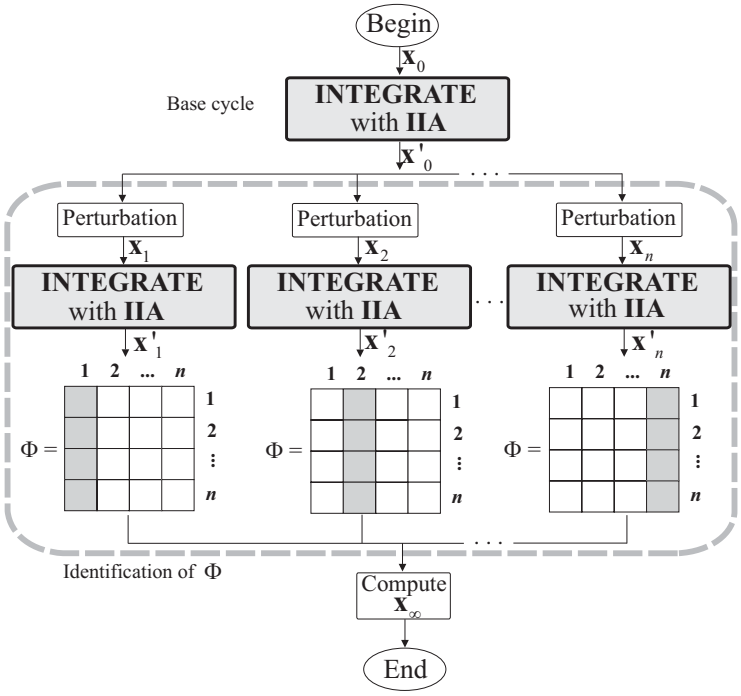

Figure 3.9: The Newton method based on an implicit integration algorithm.

3.3.1 Implicit Algorithm Embedded into the Newton Method

The implicit integration algorithm implemented in this work is included in two specific parts of the acceleration process based on the Newton method: the base cycle and the identification of the transition matrix (see Figure 3.9).

The main tasks involved in the acceleration process described in Figure 3.9 can be summarized as follows,

- First, the stiff set of ODEs is integrated over one period of time with the implicit integration algorithm to obtain a base cycle.

- Then, the initial state vector is perturbed and the stiff set of ODEs is integrated over one period of time to compute one column of matrix $\mathbf{\Phi}$ using the ND procedure. This sequential perturbation is repeated till the whole matrix $\mathbf{\Phi}$ is computed. Therefore, the identification of matrix $\mathbf{\Phi}$ requires the application of the integration routine n times.

- Once matrix $\mathbf{\Phi}$ is calculated, matrix $(\mathbf{I}-\mathbf{\Phi})^{-1}$ is computed and a Newton method is applied to find $\mathbf{x}_\infty$.

Table 3.1: values of gains for sustained oscillation method.

	K_p	T_r	T_d
P	$0.5K_c$		
PI	$0.45K_c$	$\frac{P_c}{1.2}$	
PID	$0.56K_c$	$0.5P_c$	$\frac{P_c}{8}$

It must be brought to attention the fact that the computation of the transition matrix represents the most demanded task in the Newton method. For instance, the acceleration to the periodic steady-state of n state variables requires $n+1$ applications of the integration routine. Consequently, the incorporation of implicit integration algorithms with variable step instead of explicit integration techniques with fixed step has a direct impact on the global efficiency of the Newton method.

3.4 Synchronous Link Test Case

The test case presented in this section consists of two electric systems with rated frequency equal to 60 Hz and a synchronous link based on a VFT (see Figure 3.10). Stator and rotor voltage magnitude is 1.0 pu and the angular difference between both power networks is zero. The control system gains were obtained by tuning the PI controller using the Ziegler-Nichol's method based on the sustained oscillation response [Astrom95]. This method is carried-out through the following steps.

1. Set the system under proportional control with a small gain.
2. Increase proportional gain until the system is oscillatory.
3. Record the controller critical proportional gain $K_p = K_c$ and the oscillation period of the controlled output P_c.
4. Adjust the controller parameters according to Table 3.1.

The additional VFT parameters used in this section are reported in the Appendix D. The whole system is described with a set of 41 ODEs, where the periodic steady-state is computed with the Newton method with both the explicit Runge-Kutta $4\,th$ order algorithm (RK4) and the implicit integration algorithm (IIA) used in this research. Two steady-state scenarios are reported: *i.*- energization of the VFT with no power transfer and *ii.*- nominal step power transfer. The maximum mismatch to locate the

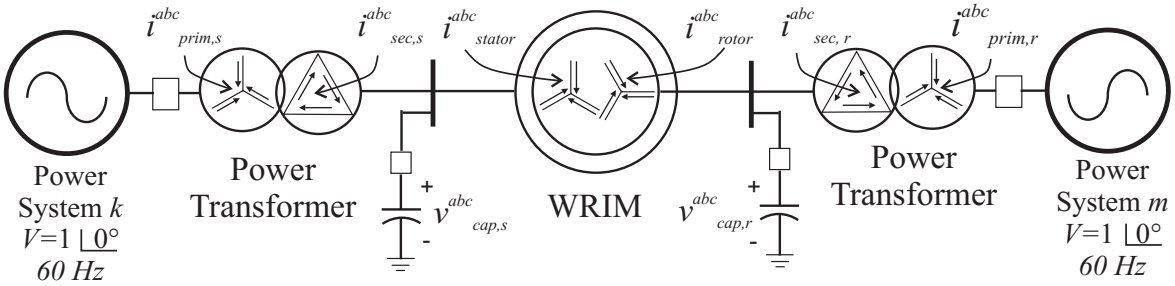

Figure 3.10: Synchronouse link test case.

periodic steady-state is set to 1.0×10^{-10}. The computational effort is measured in a PC dual core at 1.7 GHz and 1 Gb RAM memory. The set of equations that defined this test case are summarized in Appendix E.

3.4.1 Convergence to the Steady-State

Table 3.2 summarizes the number of Newton-Raphson (NR) applications needed to locate the periodic steady-state solution for two steady-state scenarios with both implicit and explicit integration algorithms. A base cycle is computed after five initial cycles of integration and 11 NR applications are required to reach the steady-state for the start-up of the VFT with both IIA and RK4 algorithms. After the steady-state is computed for the energization scenario, the power transfer command in the control system is set to 1.0 pu in order to increase the power transfer to rated capacity. The closed loop control system incorporated to the VFT adjusts the mechanic torque in order to fit the desired power transfer. A new base cycle is determined after five cycles of integration and only 5 NR applications are needed to find the periodic steady-state with both IIA and RK4 algorithms.

Figure 3.11 summarizes the elapsed times needed to compute the periodic steady-state after the energization and the step power command using the RK4 and IIA algorithms. The speedup factors obtained with the IIA and the Newton method to compute periodic steady-state solution are computed with Speedup $= T_{RK4}/T_{IIA}$, where T_{RK4} is the elapsed time needed by the Newton method with the explicit integration algorithm and T_{IIA} is the elapsed time required by the Newton method with the implicit integration algorithm. Speed up factors up to 19 and 21 are obtained with the IIA using a Numerical Differentiation approach for the energization and step power command, respectively. These important differences in the elapsed times measured for these two approaches are due to the small time step required by the explicit RK4 method. For this

Table 3.2: Errors During Convergence of the VFT with Implicit and Explicit Integration Algorithms.

	Energization		Step power command	
NR	IIA	RK4	IIA	RK4
BC	7.6920e-2	7.6920e-2	2.4803e-2	2.4803e-2
1	6.9420e-1	6.9422e-1	3.9919e-1	3.9924e-1
2	5.5138e-1	5.5101e-1	7.5727e-3	7.5743e-3
3	1.1290e-1	1.1305e-1	2.8298e-5	2.8207e-5
4	9.8923e-3	9.8819e-3	2.0571e-8	2.0004e-8
5	1.6995e-4	1.6964e-4	5.252e-11	3.608e-14
6	2.9801e-5	2.9912e-5		
7	3.3519e-5	3.3452e-5		
8	1.2345e-5	1.2844e-5		
9	1.7222e-6	1.5885e-6		
10	1.7394e-9	9.781e-10		
11	2.686e-11	4.440e-14		

test case, a time step equal to $h = 0.2543\,\mu s$ is needed in order to ensure convergence with the RK4 integration routine.

On the other hand, it can be appreciated that a large number of NR applications are required to reach the steady-state during energization of the VFT (see Table 3.2). This important number of NR applications is associated to the quality of the initial conditions provided at the base cycle. Therefore, an alternative is proposed in order to reduce the total number of NR applications by providing adequate initial conditions at the base cycle. This procedure is summarized as follows,

1. Solve n initial cycles of integration with the set of ordinary differential equations taking into account the saturation effects of the nolinear components. The number n is equal to 5 for this test case.

2. Compute a base cycle using the set of ordinary differential equations without incorporating the saturation characteristic of the nonlinear components.

3. Start the acceleration procedure applying the Newton method incorporating the saturation effects to the nonlinear components and using the initial conditions provided in step 2.

Table 3.3 shows the maximum errors during convergence of the VFT for the energization scenario using this alternative to compute a set of initial conditions at the base cycle.

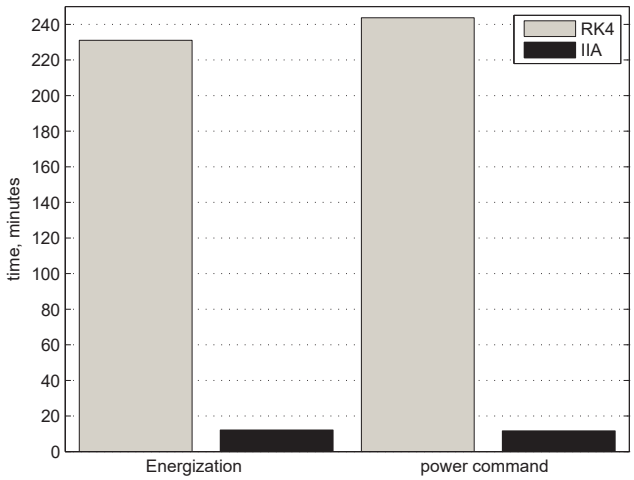

Figure 3.11: Elapsed times for the energization and step power command.

Table 3.3: Maximum mismatches during convergence for the energization of the VFT using a procedure to improve the initial conditions.

	Energization
NR	IIA
BC	1.0288e-1
1	2.3400e-3
2	1.3915e-4
3	1.9687e-5
4	1.8021e-7
5	2.952e-11

It can be observed that only 5 NR applications are needed to reach the periodic steady-state for energization. As a consequence, the total number of NR applications is reduced from 11 to 5. This reduction in the number of NR applications is associated to the improve initial conditions provided to the Newton method.

3.4.2 Reactive power demand

Figure 3.12 shows the reactive power demanded by the WRIM as a function of the active power flow at different rotor frequencies with the stator frequency at 60 Hz. The total reactive power requirement of the WRIM is a combination of reactive power consumed by the stator and rotor leakage reactances and the reactive power consumed by the magnetizing reactance. As an example, it can be observed that reactive power

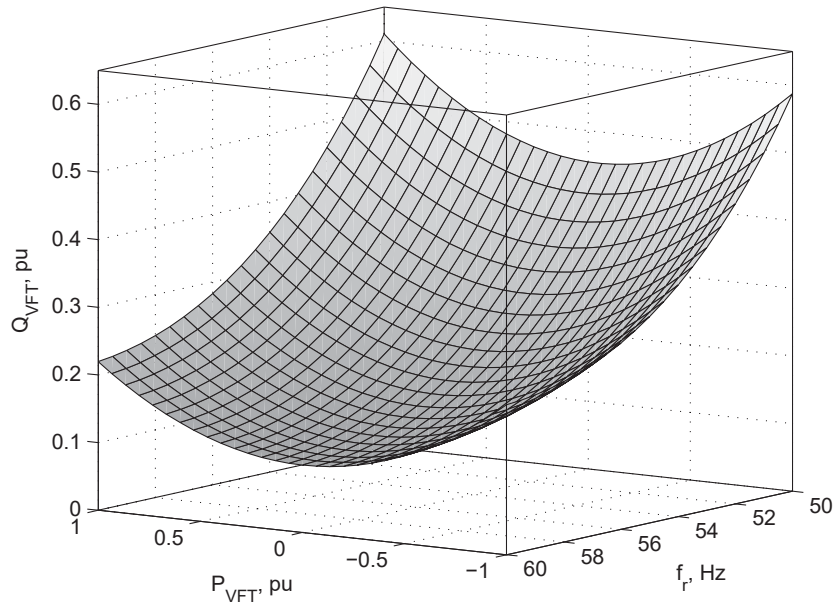

Figure 3.12: Reactive power demanded by the VFT as a function of active power transfer and rotor side frequency with $f_s = 60$ Hz.

consumed by the VFT with $P_{VFT} = 0$, $f_s = 60$ Hz and $f_r = 60$ is about 0.1 pu. This amount of reactive power consumption is associated to the magnetizing reactance of the rotary machine. The total reactive power consumed by the VFT at rated power transfer with stator and rotor line frequencies at 60 Hz is about 0.22 pu. The VFT reactive power demand at rated power transfer is related not only to the magnetizing reactance but also the stator and rotor leakage reactance. Assuming $f_s = 60$ Hz and $f_r = 50$ Hz, the reactive power requirements are about 0.46 pu at 0 power transfer, 0.61 pu at 1.0 pu power transfer and 0.59 pu at -1.0 pu power transfer. Due to the important reactive power requirement of a VFT installation, shunt capacitor banks are required for compensation on the rotor and stator sides.

3.4.3 Harmonics

Keeping in mind that power transformers and the WRIM might contribute under specific operating conditions to the harmonic distortion in the VFT, a harmonic study is carried-out to determine the harmonic content in current and voltages. After computing the periodic steady-state with the Newton method, the harmonic spectrum is computed with the Fast Fourier Transformation (FFT). Figures 3.13 shows the harmonic content

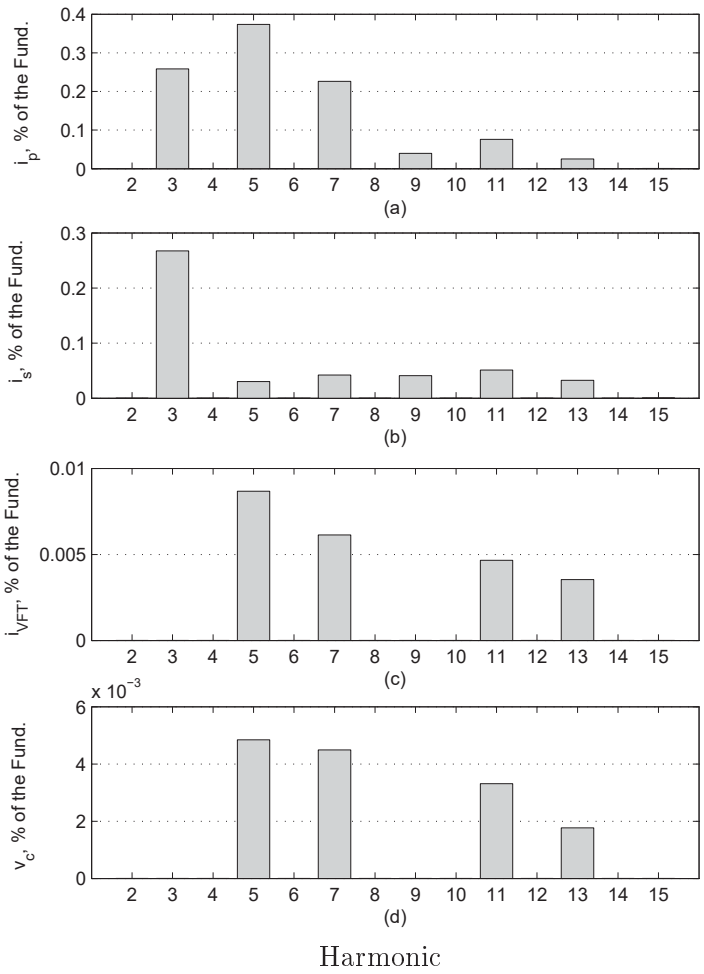

Figure 3.13: Harmonic content in the phase A of the VFT for no power transfer command: (a).- primary side current on the transformer, b).- secondary side current on the transformer, (c).- stator current in WRIM and (b).- voltage on the capacitor bank.

at selected currents and voltages for phase A for a no power transfer condition. Figures 3.13 (a)-(d) show that only odd harmonics below 0.4 % are obtained for these state variables. On the other hand, Figure 3.14 shows the harmonic content for rated power transfer operation. The highest harmonic content for i_p, i_s and i_{VFT} for rated power transfer is 0.012 %, 0.008 % and 0.0007 % for the $3rd$ and $5th$ harmonic, respectively (see Figure 3.14 (a)-(c)). Figure 3.14 (d) shows the harmonic content for voltage at the capacitor bank connected at the stator side. Figure 3.14 (d) shows that the $5th$, $7th$ $11th$ and $13th$ harmonics are below 0.004 % for rated power transfer. It can be observed that the $3rd$ harmonic does not exist due to the fact this harmonic and its multiples are captured inside the delta connection. As expected, the VFT model indicates that

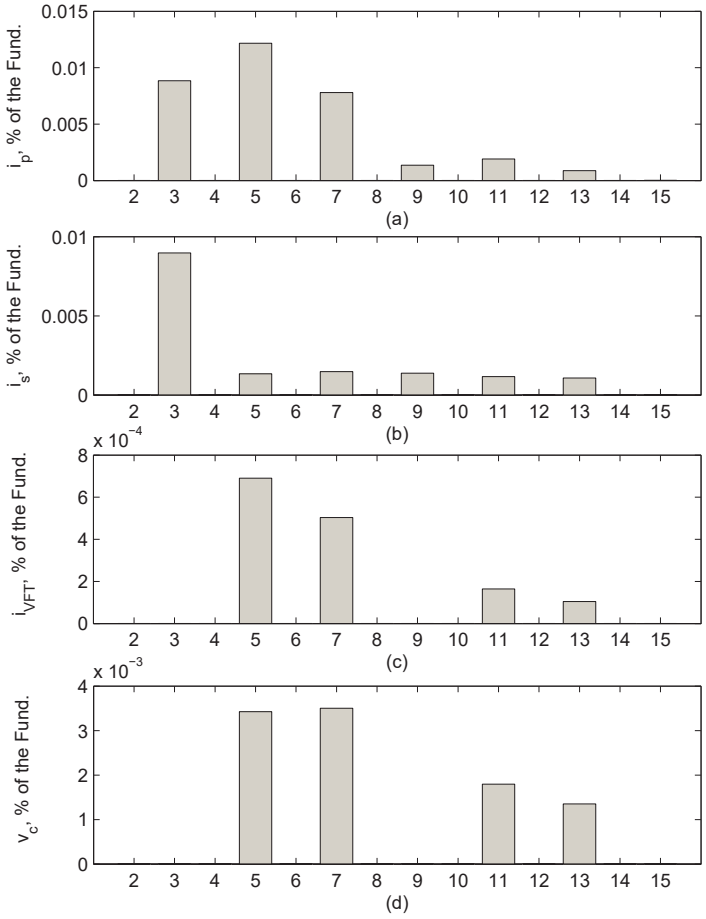

Figure 3.14: Harmonic content in the phase A of the VFT for rated power transfer: (a).- primary side current on the transformer, b).- secondary side current on the transformer, (c).- stator current in WRIM and (b).- voltage on the capacitor bank.

the VFT produces no harmonics for the operation under nominal conditions.

Figure 3.15 shows the total harmonic distortion (%THD) for the energization with no power transfer and for a step power command scenarios. Results are reported only for phase A since similar values were obtained for phases B and C. No significant harmonic distortion has been detected in any of the currents of the conventional transformers, the WRIM or the voltages at the capacitor banks. The highest %THD for the currents at the primary side of the conventional transformer is nearly 0.52 % (see Figure 3.15 (a)). This low level of distortion is due to the fact that both transformers and the WRIM operate at the linear region of their nonlinear saturation curves. Figure 3.16 shows the time domain solution for two state variables within the VFT installation for rated power

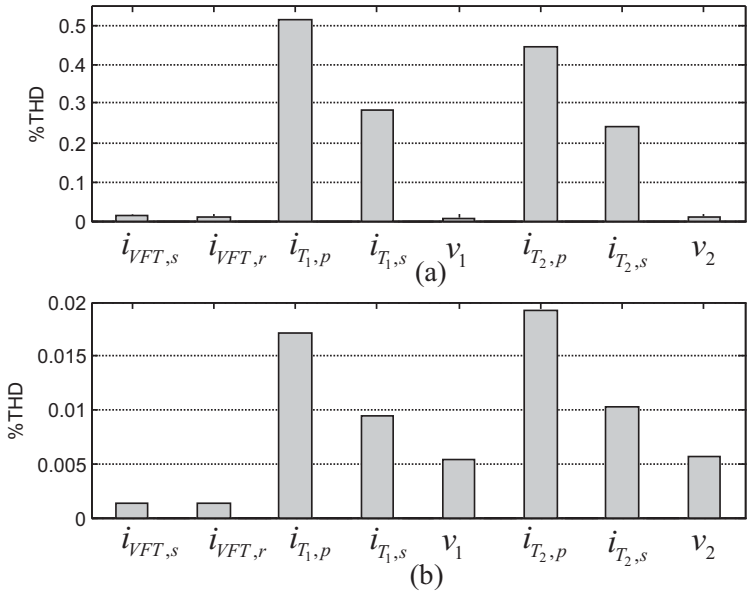

Figure 3.15: %THD on currents and voltages for phase A during (a).- energization and (b).- step power command.

transfer. Figure 3.16 (a) reports the transient and the periodic steady-state solutions of the current on the primary side of the transformer on the stator side. Figure 3.16 (b) shows the dynamic and periodic steady-state solutions of a phase to phase voltage at the capacitor bank on the stator side. It can be noted that after five initial cycles of integration, a base cycle is computed and the periodic steady-state is determined with the Newton method. Figure 3.17 depicts the limit cycles associated to the current on the transformer and the voltage at the capacitor bank on the stator side.

On the other hand, it is of interest to determine the frequencies generated in the VFT by unbalanced supply voltages. Then, the synchronous link test case shown in Figure 3.10 is fed with and unbalanced voltage of 5.7 % on the stator side, while voltage supply on the rotor side remains balanced. The unbalanced condition is 1.1 pu for phase A, 1.0 pu for phase B and 0.9 pu for phase C. The Newton method is used to compute the periodic steady-state and five NR applications are required to reach the steady-state (not shown). After computing the periodic steady-state with the Newton method, the harmonic spectrum is computed with the Fast Fourier Transformation. Figure 3.18 shows the time domain solution for two state variables within the VFT installation for unbalanced voltage of 5.7 %. Figure 3.18 (a) reports the transient and the periodic steady-state solutions of the current on the primary side of the transformer on the stator side. Figure 3.18 (b) shows the dynamic and periodic steady-state solutions of a phase

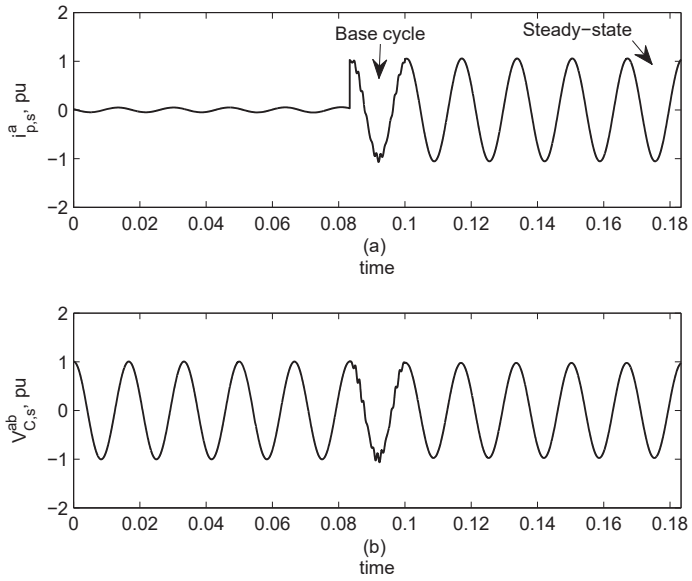

Figure 3.16: Time domain solution for (a).- current on the primary side of the transformer on the stator side and (b).- phase to phase voltage at the capacitor capacitor bank on the stator side.

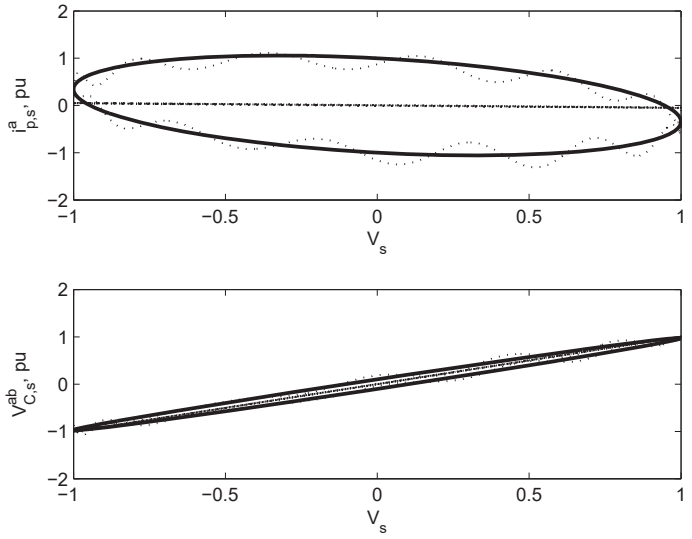

Figure 3.17: Limit cycle for (a).- current on the primary side of the transformer on the stator side and (b).- phase to phase voltage at the capacitor capacitor bank on the stator side.

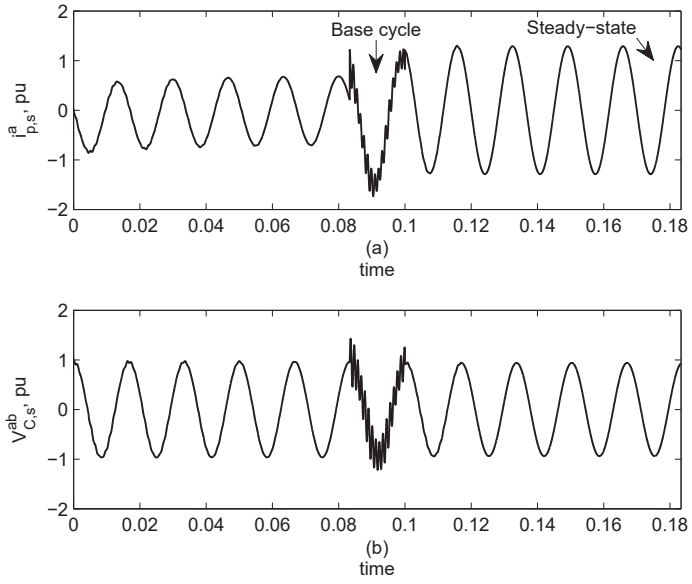

Figure 3.18: Time domain solution for (a).- current on the primary side of the transformer on the stator side and (b).- phase to phase voltage at the capacitor capacitor bank on the stator side.

to phase voltage at the capacitor bank on the stator side. It can be noted that after five initial cycles of integration, a base cycle is computed and the periodic steady-state is determined with the Newton method. Figure 3.19 depicts the limit cycles associated to the current on the transformer and the voltage at the capacitor bank on the stator side.

Figure 3.20 shows the harmonic content of the currents and voltage for phase A,B,C in the VFT for unbalanced operation, where the harmonic content is reported in percent of the fundamental. Figures 3.20 (a) and (b) shows the harmonic content of the primary and secondary side currents in the conventional power transformer at the stator side, respectively. Figure 3.20 (c) shows harmonic content for the currents through the WRIM at stator side, while Figure 3.20 (d) shows the harmonic content for voltages at the capacitor bank connected at the stator side. It can be appreciated that the most significant harmonics are below 0.05 %. Figure 3.21 shows the total harmonic distortion (%THD) for this unbalanced operation. The highest %THD for the current of phase A at the primary side of the conventional transformer connected at stator side is nearly 0.063 %.

It can be observed from Figures 3.20 and 3.21 that no significant harmonics neither

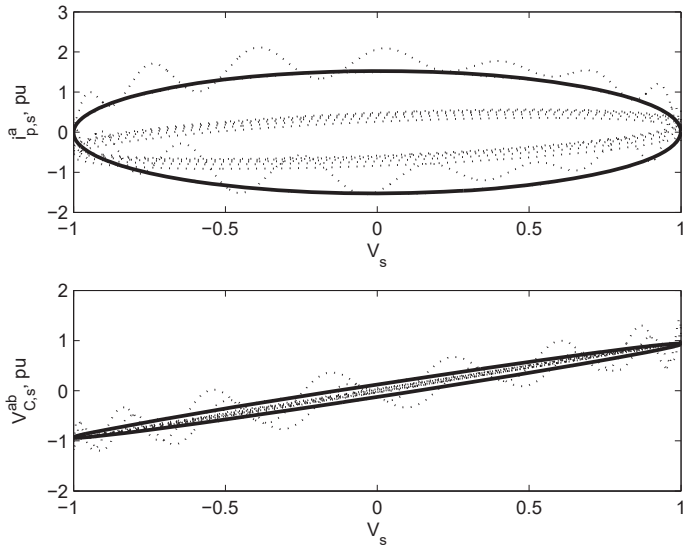

Figure 3.19: Limit cycles for (a).- current on the primary side of the transformer on the stator side and (b).- phase to phase voltage at the capacitor capacitor bank on the stator side.

total harmonic distortion are detected for a voltage umbalanced 5.7 %. These results are expected because the voltage umbalanced is not high enough to force the conventional transformers and the VFT to operated in the nonlinear region of their saturation characteristic. Furthermore, it should be noted that conventional transformers and the VFT are the only nonlinear components of the test case.

In addition, an unbalanced voltage of 11.8 % is supplied on the stator side, while maintaining a balanced three-phase voltage source on the rotor side. The voltage supply on the stator side is defined with 1.5 pu for phase A, 1.0 pu for phase B and 1.2 pu for phase C. The harmonic spectrum of selected state variables of the VFT installation is reported in Figure 3.22. It can be observed from Figures 3.22 (a) and (b) that unbalanced odd harmonics are observed at phases A, B and C. The highest harmonic content in currents at the primary side of the conventional transformer is 3.4% of the fundamental for the *3th* harmonic. Figures 3.22 (c) and (d) show that odd harmonics are below 0.8 %. Furthermore, it can be seen that the $3rd$ harmonic and its multiples appear at current i_{VFT} and voltage v_C due to the unbalanced operating condition. Under unbalanced operation the VFT may provide a low harmonic distortion to the network, but this harmonic contribution depends of the percent of the unbalanced condition. Figure 3.23 shows the total harmonic distortion (%THD) for the unbalanced

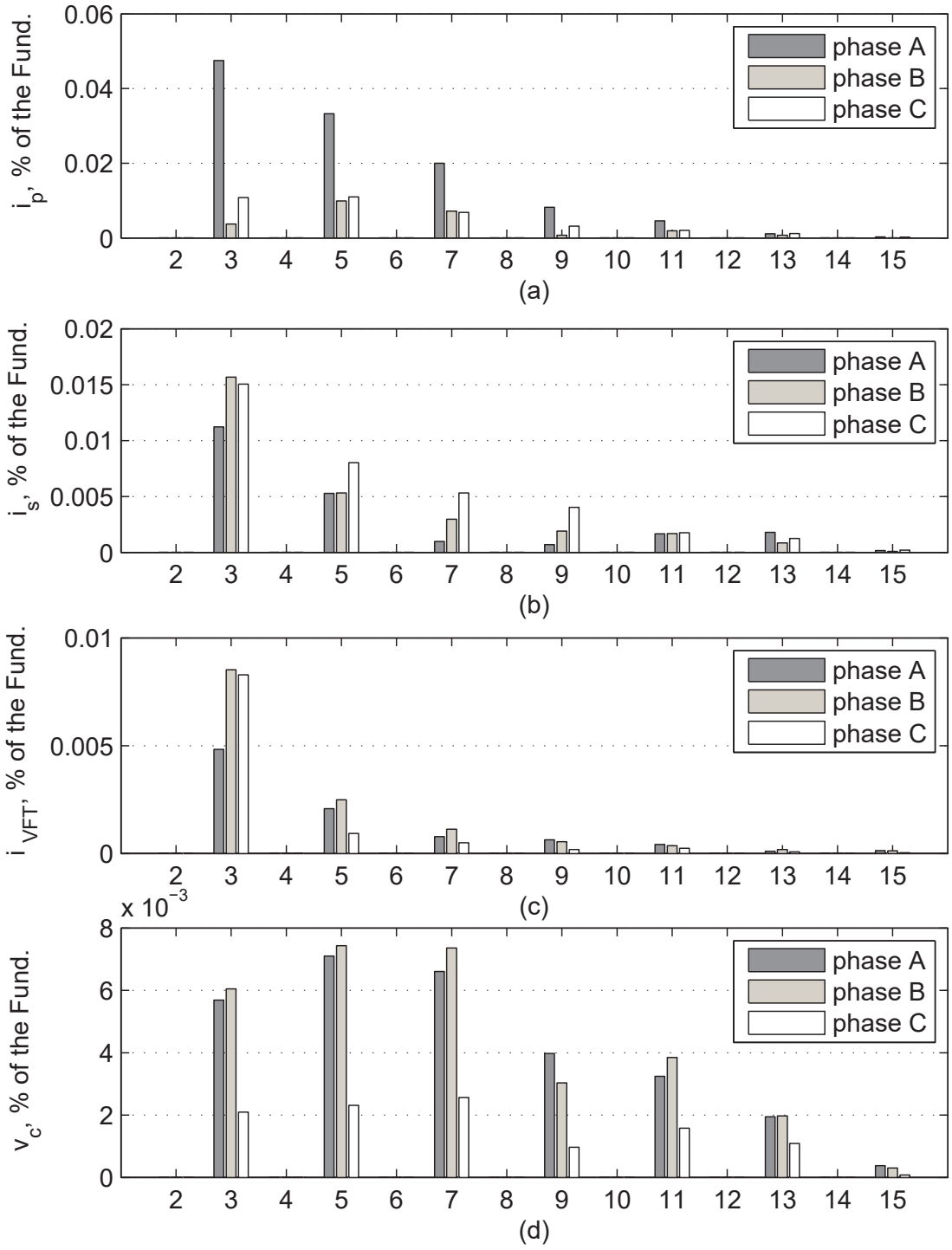

Figure 3.20: Harmonic content in the phase A,B,C of the VFT for voltage unbalanced of 5.7 %: (a).- primary current on the transformer, b).- secondary current on the transformer, (c).- stator current in WRIM and (b).- voltage on the capacitor bank.

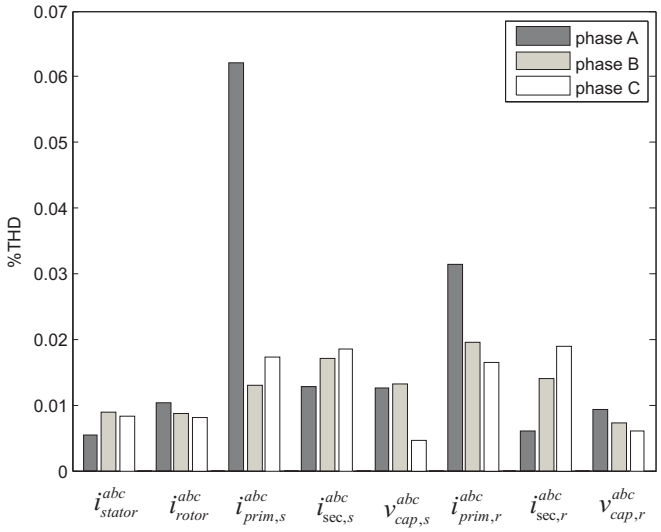

Figure 3.21: %THD on selected currents and voltages for phases A,B,C for a voltage unbalanced of 5.7 %.

operation. The highest %THD for the current of the phase A at the primary side of the conventional transformer connected at stator side is nearly 4.25%.

In opposition to the harmonic distortion results obtanied with a voltage umbalanced 5.7 %, it can be appreciated from Figures 3.22 and 3.23 that a low harmonic distortion is observed for a voltage umbalanced of 11.8 %. As a result of this voltage umbalanced the conventional transformers and the VFT operate at the beginning of the nonlinear region of their saturation characteristic. Despite the fact that the most important harmonics shown in Figure 3.22 are below 5 % of the fundamental, detailed harmonic analyses should be carried-out once additional power electronics controllers would be added to the VFT installation.

3.5 Conclusions

A time domain model in phase-coordinate representation for a variable frequency transformer, suitable for harmonic-oriented studies, has been presented in this chapter. The periodic steady-state solution of the VFT including a saturated wound rotor induction machine, transformers with their nonlinear characteristic, the DC motor drive with its control system and capacitor banks has been computed using the Newton method and an efficient implicit integration algorithm. The steady-state solution is located after 5 applications of the Newton-Raphson procedure using the IIA for the operation of the

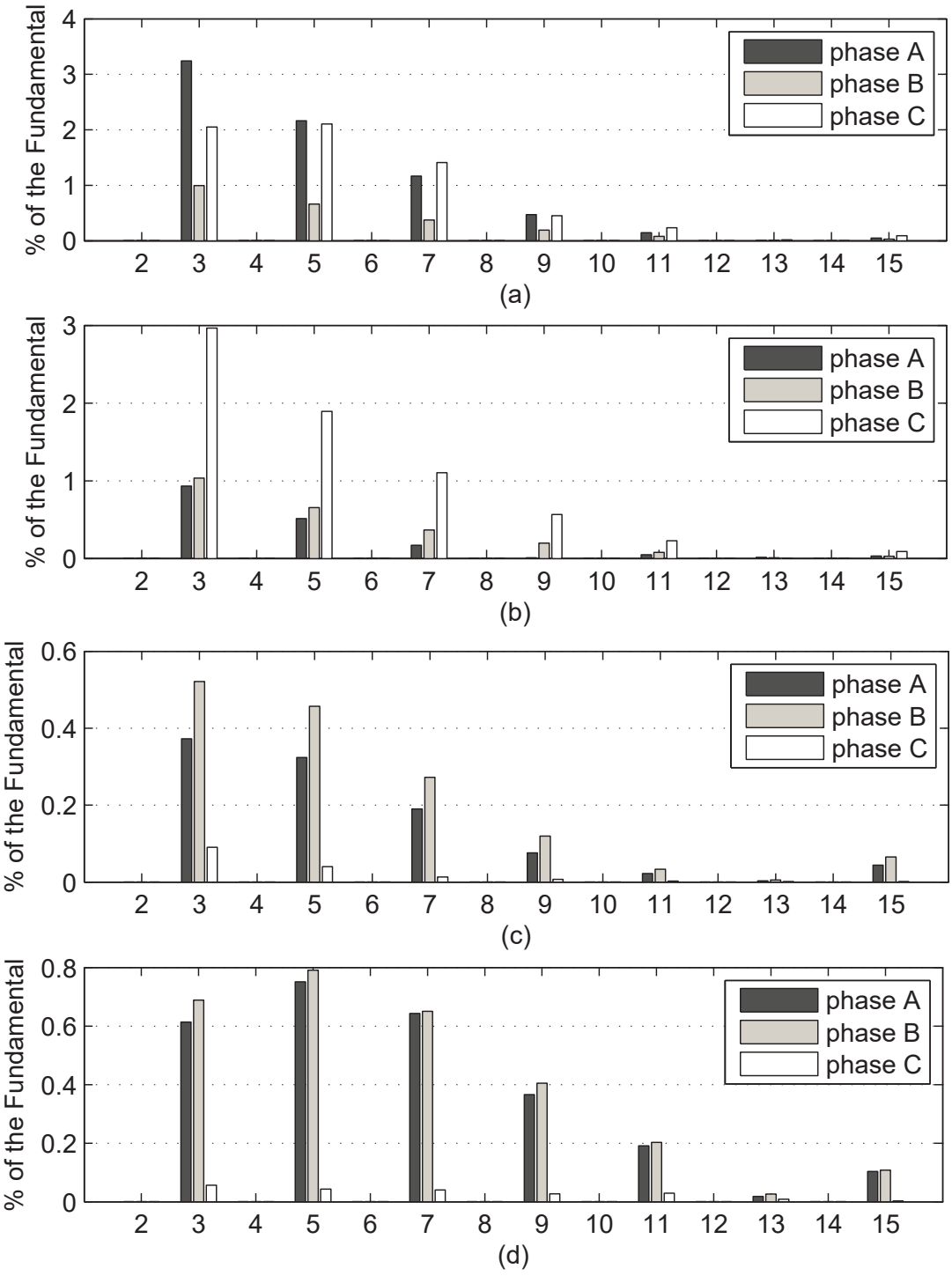

Figure 3.22: Harmonic content in the phase A,B,C of the VFT for voltage unbalanced of 11.8 %: (a).- primary current on the transformer, b).- secondary current on the transformer, (c).- stator current in WRIM and (b).- voltage on the capacitor bank.

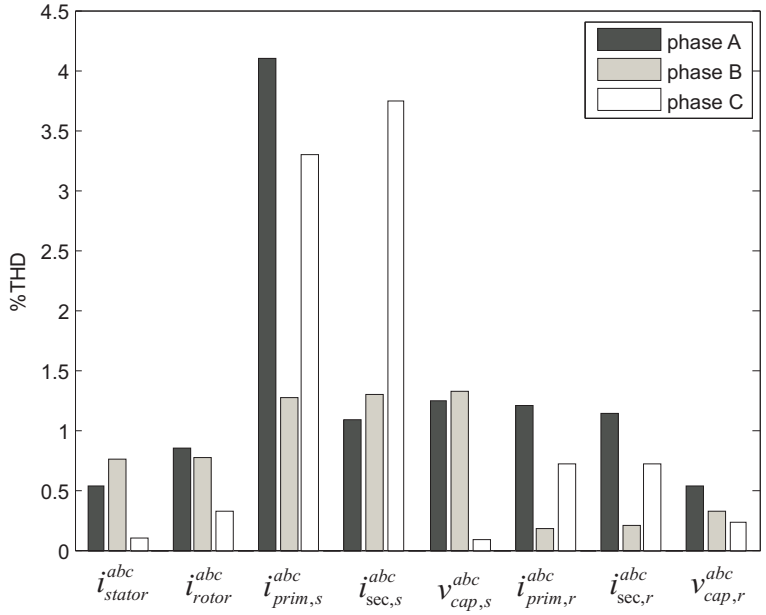

Figure 3.23: %THD on selected currents and voltages for phases A,B,C for a voltage unbalanced of 11.8 %.

VFT for energization and step power command, respectively. Speedup gains of nearly 19 and 21 have been achieved with the Newton method and the IIA for the location of the periodic steady-state. No significant harmonic distortion has been detected during the operation of the VFT because the WRIM and transformers operates in the linear region of their saturation characteristic. A harmonic content of nearly 4.25 % of THD has been observed at selected state variable for an unbalanced power supply condition of order 11.8 %. This level of harmonic distortion is due to the generation of the 3rd harmonic and its multiples associated to the unbalanced voltage. Besides, nonlinear components such as the conventional transformer and the WRIM within the VFT operate in the nonlinear region of their saturation curve because of the voltage level simulated during the unbalanced condition.

Chapter 4

VFT MODEL FOR PLANNING STUDIES IN PSS/E

4.1 Introduction

The problem of supplying sufficient power quantity and quality keeping in mind the safety and reliability of the power system has gained increasing importance due to economic impact on industries and countries. Planning strategies of the power system must be implemented in order to overcome this problem, taking into account technical, economical, political and regional considerations. It becomes clear that each investment decision requires particularly careful planning and research. For this reason, it is important to carry-out planning studies for the operation and control of potential projects involving the variable frequency transformer.

In this Chapter, a reduced order model for the VFT is integrated with the Power System Simulator for Engineering (PSS/E) based on the user written model integration technique. The rotary machine of the VFT is modelled as a Phase-Shifting Transformer (PST) for power flow studies. In addition an equivalent model comprising two ordinary differential equations is define for the mechanical part of the rotary machine to be used in transient analyses. Further, a control system provides a mechanic torque drive on the rotor shaft of the rotary machine to control the power flow throughout the VFT. Conventional transformers and shunt capacitor banks are connected at both stator and rotor side in order to link the rotary machine with the power grids and provide reactive power compensation, respectively. The planning studies reported in this chapter have been carried-out due to the interaction with the Programación de Redes Eléctricas of

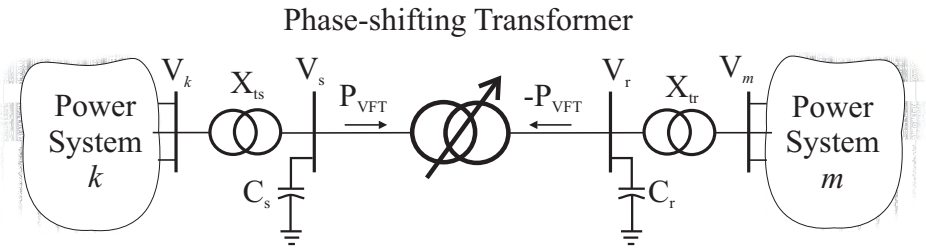

Figure 4.1: VFT power circuit model for power flow analysis.

the CFE.

4.2 VFT model for Planning Studies

A VFT user model for PSS/E software is developed in this section to carry-out power flow and transient studies. The VFT model for power flow solution consists of a phase-shifting transformer, while the VFT representation for transient solutions aggregates two additional ordinary differential equations. In other words, a phase-shifting transformer is used in PSS/E to carry-out power flow studies, while the reduce model of order two described in Chapter 2 is implemented in the PSS/E software for transient stability studies. Despite the fact that higher order model have been described in Chapter 2, the model of order two is good enough to perform transient stability studies. The VFT model includes a control system that adjust the power transfer to the set point provided by the operator. Coupling transformers and capacitor banks are required to link the VFT to the systems and reactive power requirements, respectively.

4.2.1 VFT Model for Power Flow Analysis

In general, the Variable Frequency Transformer behaves as a continuously adjustable phase-shifting transformer. As a consequence, the VFT model for power flow analysis is defined in this chapter as a phase-shifting transformer. The phase angle limits can be set as large as needed to obtain the desired active power flow. Shunt reactive compensation represented with fixed capacitors or FACTS controller can be added to power flow analyses to achieve the desired voltage control. Figure 4.1 illustrates an asynchronous link based on VFT model for power flow studies [Piwko05].

Active power flow across the VFT is proportional to the angle of the rotary machine. The impedances of the rotary machine, power transformers and AC grid determine the

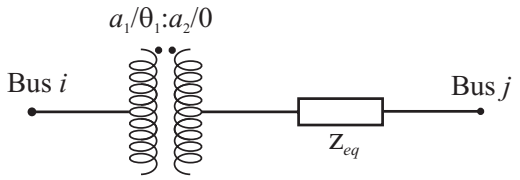

Figure 4.2: Phase-shifting transformer equivalent circuit por PSS/E simulations.

amount of shift angle needed to obtain a given power transfer. The series reactance of the rotary machine and power transformers determines reactive flow through the system as a function of voltage difference between power systems k and m.

A flexible power flow model for the phase-shifting transformer is described in [Siemens07]. Internally, PSS/E represents a two-winding phase-shifting transformer as shown in Figure 4.2 . This model uses tapped zigzag-connected windings to produce an adjustable phase shift between primary and secondary windings. The equivalent turns ratio a may be either constant or variable as the phase shift is altered, depending on the design of the specific unit. PSS/E allows the user to specify both the amplitude winding ratios a_1, a_2, and phase shift θ of every transformer. The phase shift angle θ is the angle by which winding 2 leads winding 1. The PSS/E power flow solutions include logic for automatic adjustment of both a and θ. It must be noted that the automatic adjustment of a does not alter θ and more importantly that PSS/E assumes that a is independent of adjustments of θ.

The phase-shift angle of each phase shifter transformer is adjusted as many times a necessary to keep the real power flow through the phase shifter within the power limits P_{MAX} and P_{MIN}. Phase-shift adjustment is continuous and all phase shifters are adjusted simultaneously, whenever the regulated real power flow of one of them falls outside its scheduled band. Attention must be paid since an unduly narrow band can cause nonconvergence of the power flow solution. A reasonable band is ± 2.5 MW of the total power flow control.

4.2.2 VFT Model for Transient Stability Simulations

A VFT model for dynamic simulations is shown in Figure 4.3 [Piwko05]. In dynamic events, the phase angle of the VFT varies as a function of rotor dynamics and the torque applied by the drive system motor. The VFT control system measures active power and rotor speed signals in order to determine the electromagnetic torque and the speed of the rotor, respectively. The power and speed regulators within the VFT

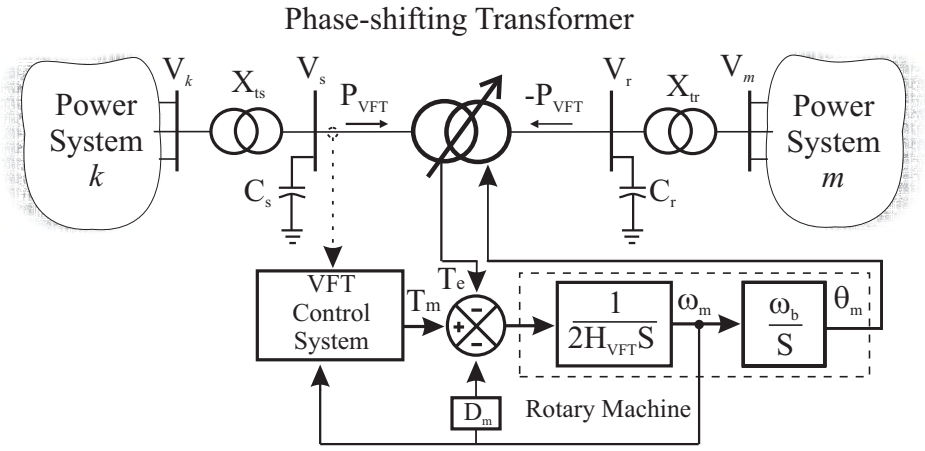

Figure 4.3: VFT model for dynamic simulations for dynamic simulation in PSS/E.

control system use the measured signals to compute a torque command to be applied by the drive motor system to the VFT rotor. The difference between the drive motor torque, damping torque and the electromagnetic torque on the rotary machine produces an accelerating torque. As a result, the rotor inertia equations for the rotary machine are [Kundur94],

$$\frac{d}{dt}\omega_m = \frac{\mathrm{T_e} - \mathrm{T_m} - \mathrm{D_m}\omega_m}{2\mathrm{H_{VFT}}} \tag{4.1}$$

$$\frac{d}{dt}\theta_m = \omega_m\omega_b \tag{4.2}$$

and the relation of electromagnetic torque and electric power is,

$$Te = \frac{\mathrm{P_{VFT}}}{\omega_b} \tag{4.3}$$

where $\mathrm{T_e}$ is the electromagnetic torque, $\mathrm{H_{VFT}}$ is the constant of inertia, $\mathrm{T_m}$ is the mechanic torque supplied by the control system, $\mathrm{D_m}$ is the damping coefficient, ω_m is the rotor speed and θ_m is the rotor position.

4.2.3 Control System

A block diagram of a comprehensive VFT control system is shown in Figure 4.4. The control system consists of three main stages: a power regulator, a speed regulator and a DC drive motor. This structure provides inherent stabilization, as well as enabling direct limits on speed variation of the machine. The power regulator senses power

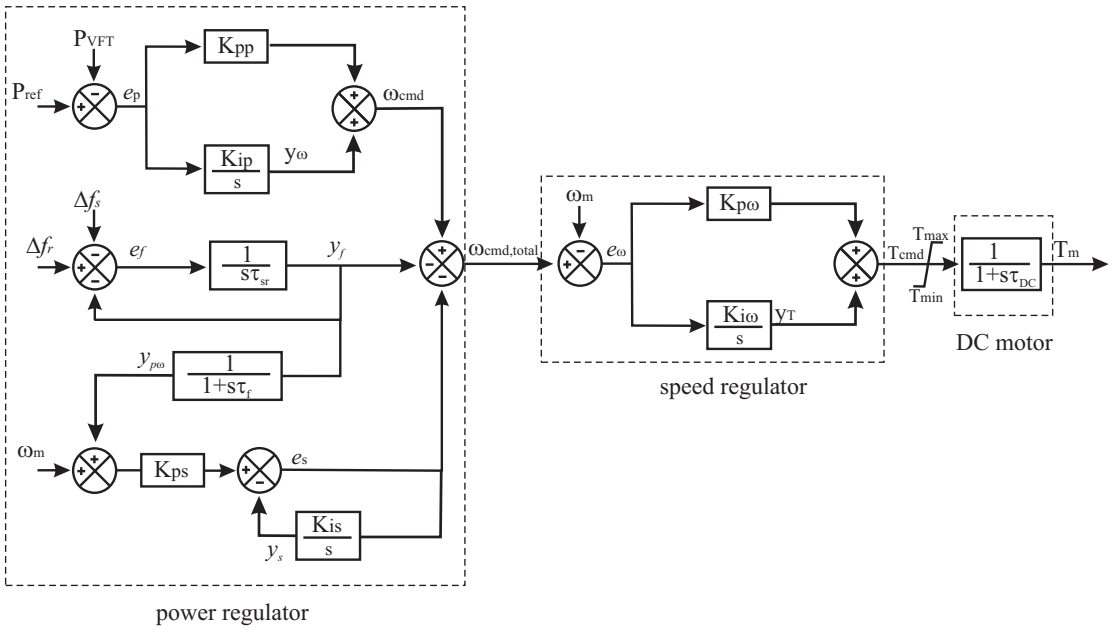

Figure 4.4: VFT control system for transient studies.

flow through the VFT and adjusts the angle until the active power matches the power command. The power flow throughout the VFT ($\mathrm{P_{VFT}}$) is measured and compared it with the power reference ($\mathrm{P_{ref}}$). The error signal (e_p) is fed to a PI controller and its output represents a partial speed command ω_cmd. This power regulator is defined as,

$$\frac{d}{dt}y_\omega = \mathrm{K_{ip}}e_\mathrm{p} \tag{4.4}$$

$$\omega_\mathrm{cmd} = y_\omega + \mathrm{K_{pp}}e_\mathrm{p} \tag{4.5}$$

where $\mathrm{K_{ip}}$ is the integral gain of the power regulator and $\mathrm{K_{pp}}$ is the proportional gain of the power regulator.

A frequency difference signal (e_f) is also provided to the speed command as an open-loop correction for grid frequency difference. If the two grids have different frequency, the rotary machine will continuously rotate to maintain the appropriate effective power angle.

$$\frac{d}{dt}y_f = \frac{(\Delta f_r - \Delta f_s - y_f)}{\tau_{sr}} \tag{4.6}$$

where Δf_r is the change of frequency of the rotor system, Δf_s is the change of frequency

of the stator system and τ_{sr} is the time constant of the correction signal.

Furthermore, a power stabilizing path is added to provide a damping signal to the speed command as follows,

$$\frac{d}{dt}y_{p\omega} = \frac{(y_f - y_{p\omega})}{\tau_f} \tag{4.7}$$

$$\frac{d}{dt}y_s = \mathrm{K_{is}}e_s \tag{4.8}$$

$$e_s = \mathrm{K_{ps}}(\omega_\mathrm{m} - y_{p\omega}) - y_s \tag{4.9}$$

where $\mathrm{K_{is}}$ is the integral gain of the power-stabilizing, $\mathrm{K_{ps}}$ is the proportional gain of the power-stabilizing and τ_f is the time constant of the power-stabilizing. Therefore, the output speed command provided by the power regulator is,

$$\omega_\mathrm{cmd,total} = \omega_\mathrm{cmd} - e_s - y_f \tag{4.10}$$

On the other hand, the speed regulator compares the speed command $\omega_\mathrm{cmd,total}$ determined by the power regulator and the rotor speed ω_m. A PI controller computes the commanded torque $\mathrm{T_{cmd}}$ using the speed error signal e_ω. A torque limiter prevents the torque command to be within the motor capability. The rate of change of the driving torque command is allowed to take values between ± 5 pu. Thus, the speed regulator is described as,

$$\frac{d}{dt}y_\mathrm{T} = \mathrm{K_{i\omega}}(\omega_\mathrm{cmd,total} - \omega_\mathrm{m}) \tag{4.11}$$

and the torque command and the DC drive motor response is,

$$\mathrm{T_{cmd}} = y_\mathrm{T} + \mathrm{K_{p\omega}}(\omega_\mathrm{cmd,total} - \omega_\mathrm{m}) \tag{4.12}$$

The torque drive feeds a first order system that represents the dynamic response of the DC drive motor. The DC drive motor is defined with one differential equation,

$$\frac{d}{dt}\mathrm{T_m} = \frac{\mathrm{T_{cmd}} - \mathrm{T_m}}{\tau_\mathrm{DC}} \tag{4.13}$$

where $\mathrm{K_{i\omega}}$ is the integral gain of the speed regulator, $\mathrm{K_{p\omega}}$ is the proportional gain of the speed regulator and τ_DC is the time constant of the DC drive motor.

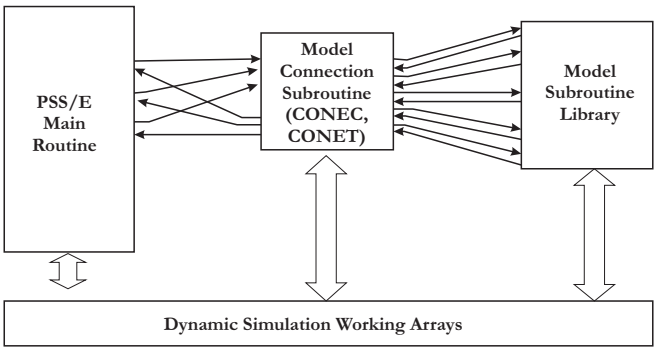

Figure 4.5: Connection of the PSS/E routine with library models.

4.3 Power System Simulator for Engineering

Power System Simulator for Engineering (PSS/E) is a commercial package with an integrated and interactive software, which is used to simulate and analyze the response of electric power systems. PSS/E provides advanced methods of analysis widely used in electrical engineering. Besides, PSS/E has a graphical user interface (GUI), which provides access to steady-state analysis such as power flow, fault analysis, optimal power flow and network equivalent construction. The dynamic simulation provides tools for transient, dynamic and long term stability analysis.

4.3.1 Dynamic Simulation

The dynamic simulation of the model library consists of three main stages (see Figure 4.5). The PSS/E main routine provides support for data input, data output, numerical integration and solution of electric networks. The differential equations of the equipment to be simulated are located in a library of subroutines, where each subroutine includes the time domain representation of a specific device.

The model connection subroutine is called whenever the main routine needs numerical values of the differential equations, while library models are called via linking subroutines CONEC and CONET. Each dynamic simulation requires the incorporation of subroutines CONEC and CONET into the main code.

4.3.2 User Written Model

The PSS/E Model Library contains a wide variety of equipment models which describe the dynamic behavior of a power system component interacting with the whole system.

However, situations may arise in which there is no library model for a particular component. To handle this situation, the PSS/E user is encouraged to write own models following the next steps [Siemens07]:

- Determine a block diagram or a set of differential and algebraic equations associated to the device to be modelled.
- Identify the state variables of the model and determine a procedure for computing the time derivatives.
- Identify input signals of the model.
- Designate arrays to locate constants, state variables and algebraic variables.
- Write the model subroutine in FLEC/FORTRAN code.

Once a model has been written, the FLEC/FORTRAN source code is compiled to generate a model in the PSS/E library. This model is linked by the CONEC subroutine in order to carry-out dynamic simulation.

4.4 Test Case I: Interconnection Link between 9-nodes and 5-nodes Electric Systems

An interconnection link test case comprising a 9-nodes electric system and a 5-nodes electric network is shown in Figure 4.6. The 9-nodes power system consists of three synchronous machines, three power transformers, 6 transmission lines and 3 loads with a total of 315 MW and 115 MVAR. On the other hand, the 5-nodes power network consists of two synchronous machines, 7 transmission lines and 4 loads with a total of 305 MW and 105 MVAR. A VFT is located between nodes 103 and 206 to exchange 100 MW from node 206 towards node 103. The internal nodes of the VFT are labeled as node 400 and node 300. The test system is implemented and studied using the PSS/E software to obtain the power flow analysis and dynamic behavior in the time domain. The interconnection link test case parameters are given in Appendix E.

4.4.1 Power Flow Solution

The power flow solution of the interconnection link with a VFT is shown in Figure 4.7. It can be appreciated that the VFT regulates the active power exchange at 98 MW.

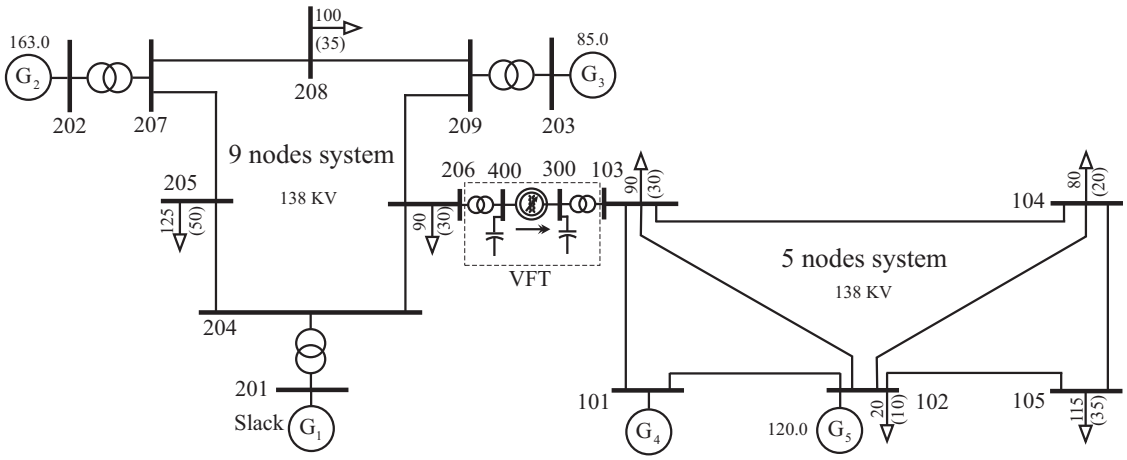

Figure 4.6: Single-line diagram of interconnection link test case.

Table 4.1: Nodal voltages for (a).- 9-nodes system, (b).- 5-nodes system and (c).- VFT.

Nodes	201	202	203	204	205	206	207	208	209
Magnitude, pu	1.04	1.02	1.02	1.02	0.99	0.99	1.02	1.01	1.02
Angle, degrees	0	4.20	-1.72	-5.37	-7.82	-11.37	-1.37	-4.92	-4.43

(a)

Nodes	101	102	103	104	105
Magnitude, pu	1.04	1.02	0.97	0.97	0.94
Angle, degrees	6.07	4.16	2.19	1.02	-1.90

(b)

Nodes	400	300
Magnitude, pu	0.99	0.98
Angle, degrees	-17.08	8.03

(c)

The 2 MW of power mismatch is associated to the control band of the PST model. The VFT rotor node maintains a phase-shift of 32 degrees with respect to stator node. The VFT demands 29.3 MVAR at rated power transfer, while the total reactive power requirement for the interconnection link is 49 MVAR. The VFT power losses are 0.1 MW, while the total losses of the test system are 15.7 MW. As expected, the slack node generates the largest amount of power. It can be appreciated that generators 1 and 3 generates 100 MW of active power, which is transmitted to node 105, via the VFT link.

The nodal voltages for the interconnection link test case are summarized in Table 4.1. Most of the nodal voltages are within an adequate voltage level to operate in the security region. The lowest voltage magnitude is found at node 105 with a voltage value of 0.94 pu.

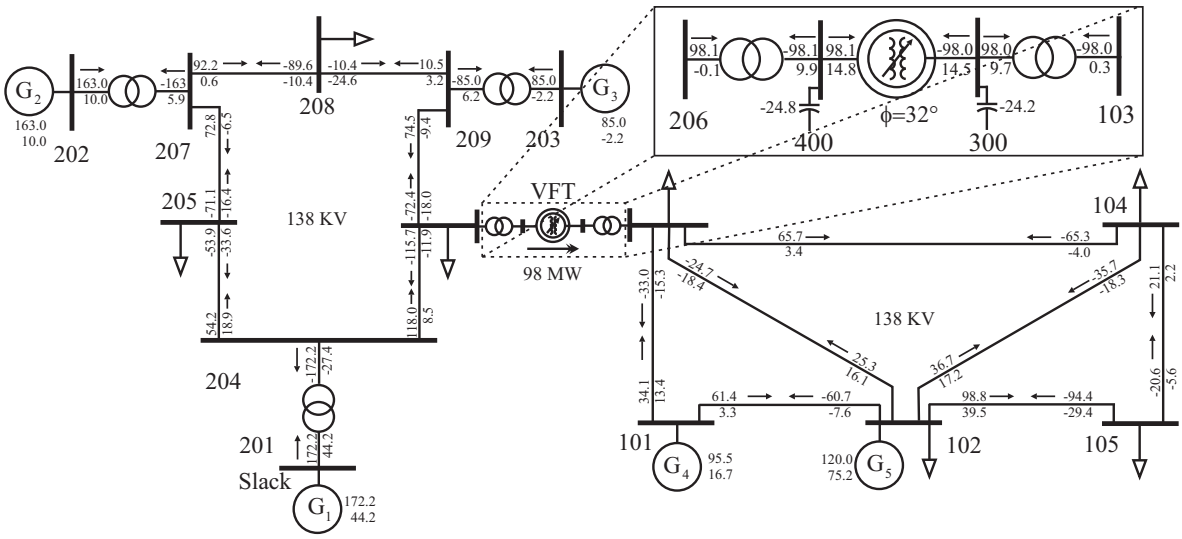

Figure 4.7: Power flow solution obtained with PSS/E for the interconnection link test system with a VFT.

4.4.2 VFT Dynamic Solution

The VFT model developed in this work for a transient studies is subjected to a fault condition in order to study its transient response. A three-phase fault to ground takes place at node 104 at $t = 1$ sec. Once fault is applied, the protections operate in 0.1 sec (6 cycles) and fault is cleared with the opening of the transmission line connected from node 103 to node 104. Figure 4.8 shows the transient solution of rotor angles associated to machines 2 and 3 with respect to machine 1, as well as the transient behavior of the rotor angle of the machine 5 with respect to the machine 4. It can be observed that the machines angles remain in synchronism for this fault scenario. Figure 4.9 (a) shows the power flow exchanged through the VFT, where it can be observed that the power flow throughout the VFT during fault is approximately 15 MW. In addition, it can be seen that power flow transient after fault clearing settles down in approximately two seconds. Figure 4.9 (b) shows the voltages at node 400 and node 300 for the three-phase fault scenario. It can be noted that the VFT voltages return to the same operating point after the fault clearing. Furthermore, low voltages at VFT terminals indicate that the VFT does not isolate the interconnected systems during the fault disturbance.

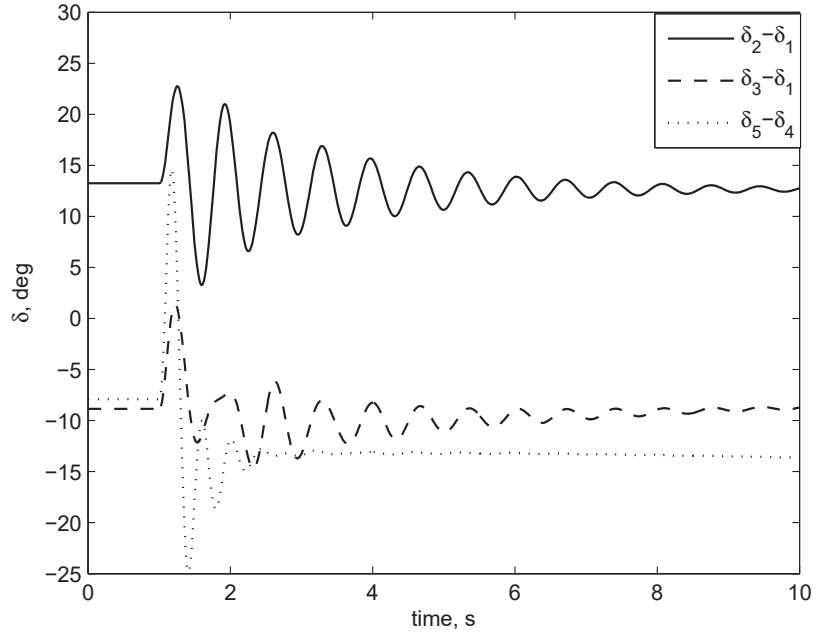

Figure 4.8: Rotor angles of the synchronous machines.

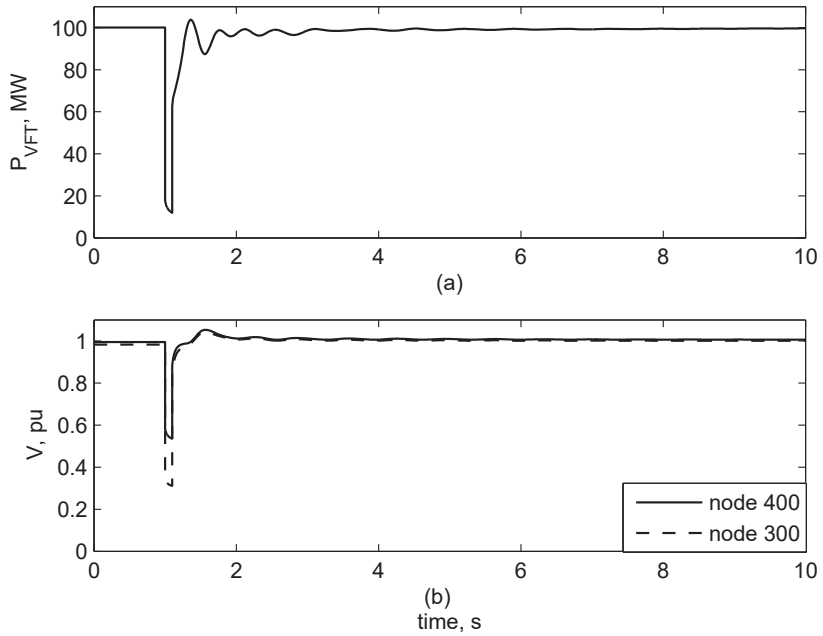

Figure 4.9: Transient behavior for (a).- power flow through the VFT and (b).- voltages at VFT terminals.

Table 4.2: Nodal voltages of the VFT park test for a (a).- 9-nodes system, (b).- 5-nodes system and (c).- VFT nodes.

Nodes	201	202	203	204	205	206	207	208	209
Magnitude, pu	1.06	1.025	1.025	1.03	0.99	0.99	1.025	1.01	1.02
Angle, degrees	0	5.55	-3.93	-6.61	-8.34	-15.57	-0.60	-4.26	-3.93

(a)

Nodes	101	102	103	104	105
Magnitude, pu	1.04	1.02	0.98	0.97	0.95
Angle, degrees	2.07	-1.10	-1.12	-2.62	-5.97

(b)

Nodes	400	300	600	500	800	700
Magnitude, pu	1.00	0.99	1.00	0.99	1.00	0.99
Angle, degrees	-19.39	2.71	-19.39	2.71	-19.39	2.71

(c)

4.4.3 VFT park

The latter test case is modified to include a VFT park with three VFT units. The VFT park controls the active power flow from 9-nodes system to 5-nodes system. The total power exchanged through the VFT park is 200 MW, 66.66 MW for each VFT unit. Figure 4.10 shows the power flow solution for this modified test case. It can be observed that each VFT unit maintains a shift angle of 26.73 degrees. The total reactive supply by the capacitor banks is 149.7 MVAR at rated power transfer whilst the total reactive power needed by the interconnection link is 96.9 MVAR. The VFT park total losses are 0 MW, while the total losses of the test system are 21.6 MW. The results are listed in the report generated by PSS/E.

A three-phase fault to ground at node 104 is simulated in order to analyze the VFT park performance during a transient condition. Figure 4.11 (a) shows the transient solution of rotor angles of machines 2 and 3 with respect to the machine 1, as well as the transient behavior of the rotor angle of the machine 5 with respect to the machine 4. It can be noted that for this contingence condition generators do not lose synchronism. Figure 4.11 (b) shows the total active power flow through the VFT park. This response shows the effectiveness of the VFT model to control the power flow in asynchronous links. Figure 4.11 (c) shows the voltages at node 400 and node 300 of VFT, for the three-phase fault scenario. It can be noted that the VFT voltages return to the same operating point after the fault clearing. Similar response are obtained for VFT_2 and VFT_3. The nodal voltages for the VFT park are given in Table 4.2. It can be appreciated that the

lowest voltage level is observed at node 105 with a voltage magnitude of 0.95 pu.

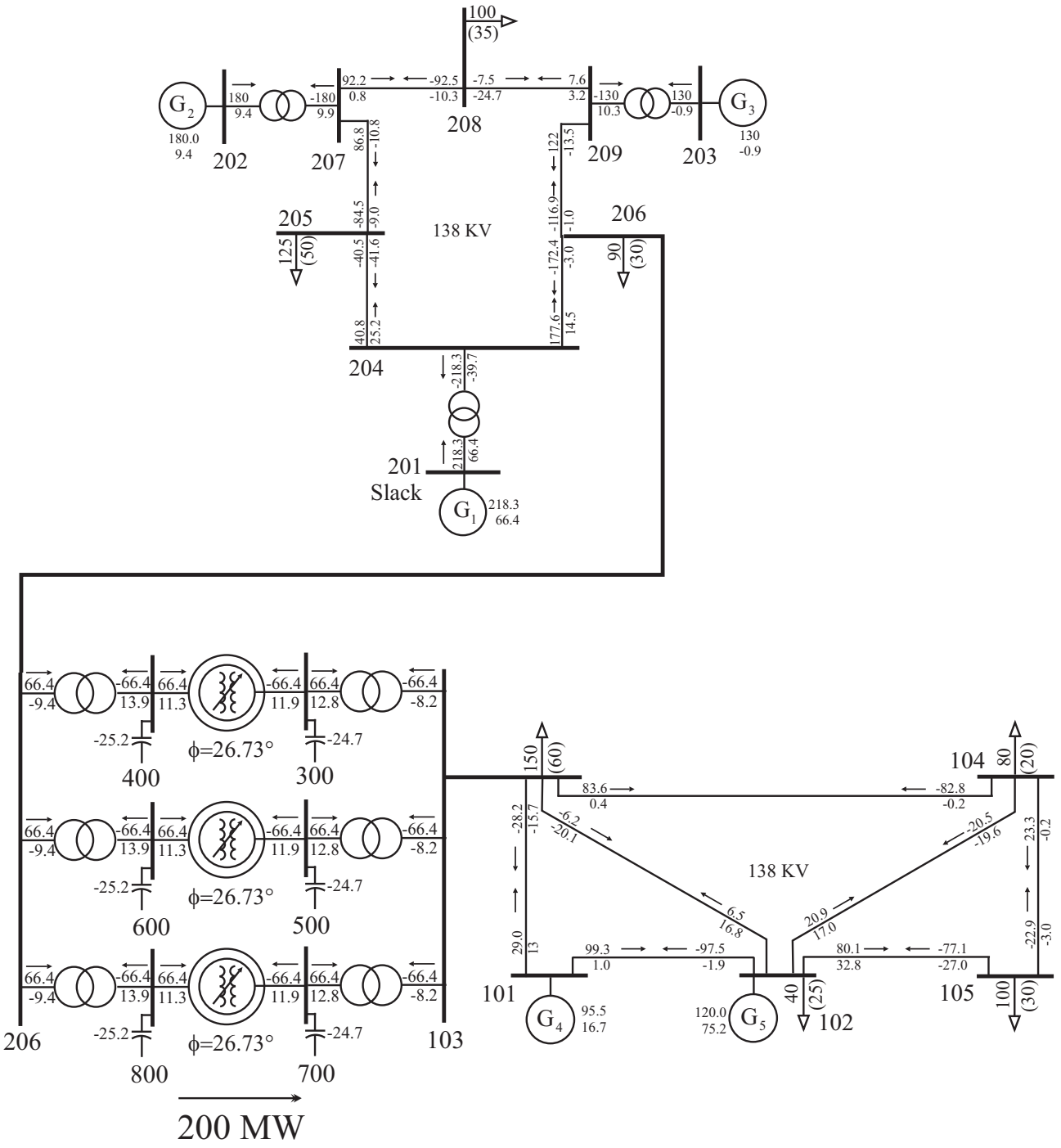

Figure 4.10: VFT park power flow solution.

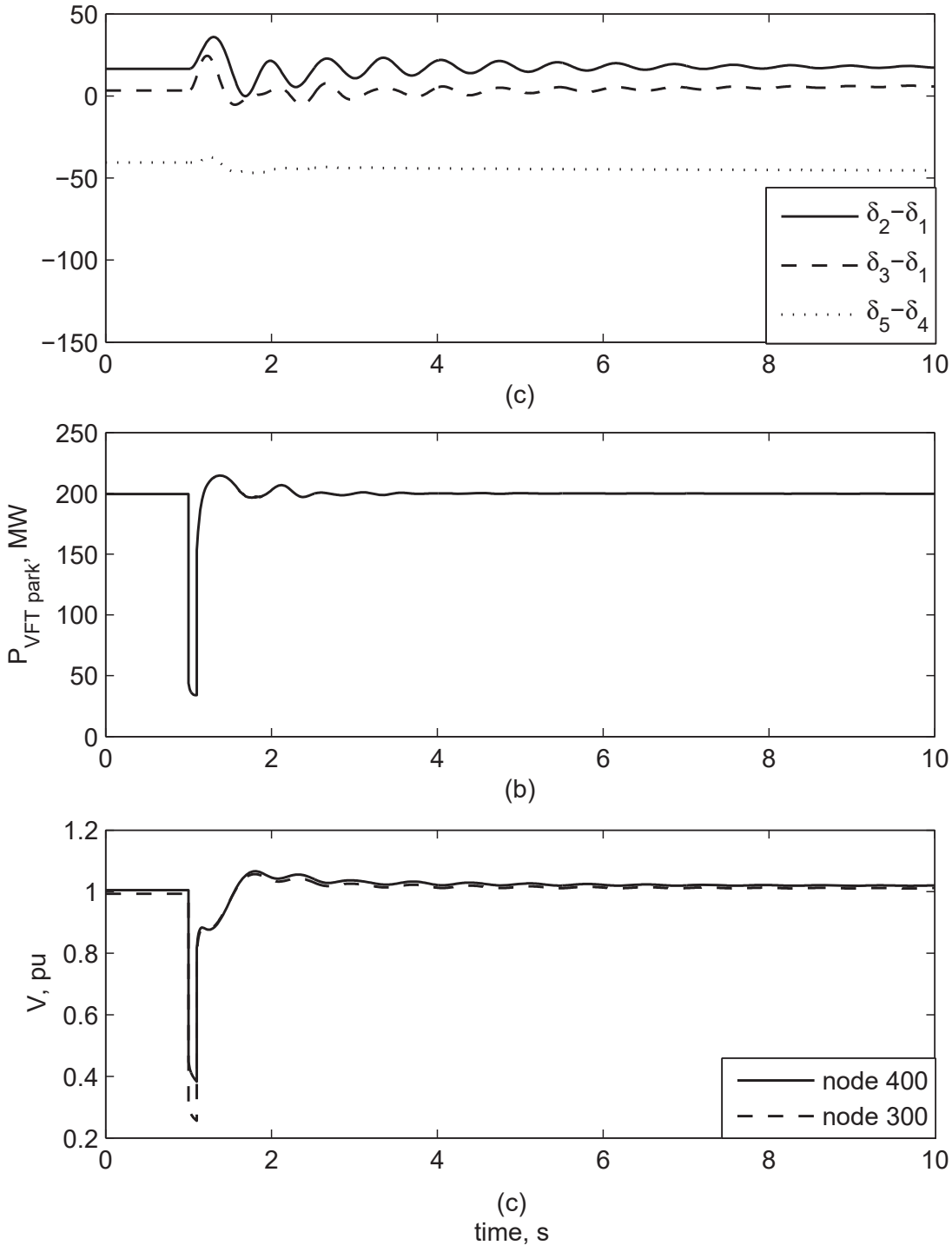

Figure 4.11: Transient behavior for (a).- rotor angles of the machines, (b).- power flow through the VFT park and (c).- voltages at VFT.

Figure 4.12: Mexican interconnection link between INS-CFE and BC-CFE systems based on VFT park.

4.5 Test Case II: Asynchronous Link in the Mexican Power System

In this section, the VFT model implemented for the PSS/E program is used to study a potential project in the Mexican power system. The authorities of the Comisión Federal de Electricidad in México are interested to construct an asynchronous link between the Interconnected National System (INS) and the power network of Baja California (BC). A feasible solution is based on the application of VFT technology. Figure 4.12 shows the location of this prospective project to interconnect the INS and BC systems. Technical specifications of this project are listed below:

- The project relies on the interconnection of the substation Seis de Abril (SSA-230) to the substation "Cucapah" (CUH-230) through a double circuit AC transmission system and two conductors per phase at 230 kV.
- The distance between SSA-230 and CUH-230 is approximately 400 Km, then a

substation called Pinacate (PTE-230) is needed for reactive power compensation at the mid point of the line.

- Pinacate (PTE-230) consists of a Static VAR Compensator (SVC-230) of -150/25 MVAR for voltage regulation at 1.0 pu.
- A VFT park consisting of three units of 100 MW and reactive compensation using three capacitor banks of 25 MVAR per VFT unit is located at the CUH-230 substation.

In order to identify the connections of the VFT park within the CUH-230 substation, CUH-230 is called the terminal node connected to BC and the terminal node CUH-VFT indicates the connection with the INS. The data to carry-out this test case were provided by the department of Programación de Redes Eléctricas of the CFE, México.

4.5.1 Power Flow Analysis

The steady-state analysis of the Mexican interconnection link is carried-out for three main operating conditions: *i*).- Power transfer exchanged equal to 0 MW, *ii*).- rated power transfer of 300 MW in the VFT park and *iii*).- a fault at the substation CUH-VFT and the opening of a transmission line between the CUH-VFT substation and PTE-230 substation. Power flow solutions for this test case are reported in Figure 4.13. It can be observed that for a power transfer equal to 0 MW the capacitor banks are not connected and the reactive power consumption of the VFT Park is 14.5 MVAR. Besides, the SVC consumes its maximum reactive power and maintains the SVC-230 node voltage at 1,001 pu.

For the rated power transfer scenario, the ISN exports 300 MW to the BC system throughout the VFT park (see Figure 4.13 (b)). The reactive power consumption of the VFT Park is 132 MVAR, while the capacitor banks supply 233.7 MVAR. Then, 110.7 MVAR is fed to BC and INS power systems. The SVC controller at PTE-230 consumes 79.4 MVAR to control the voltage of PTE-230 substation at 1 pu. It can be seen that most of the power flow imported to the BC power system is consumed by the STB-230 and MXI-230 substations.

For the fault test case at CUH-VFT substation, one transmission line circuit between CUH-VFT and PTE-230 is opened, remaining only one transmission line to transmit the entire bulk of energy (see Figure 4.13 (c)). The SVC injects 22.2 MVAR into the

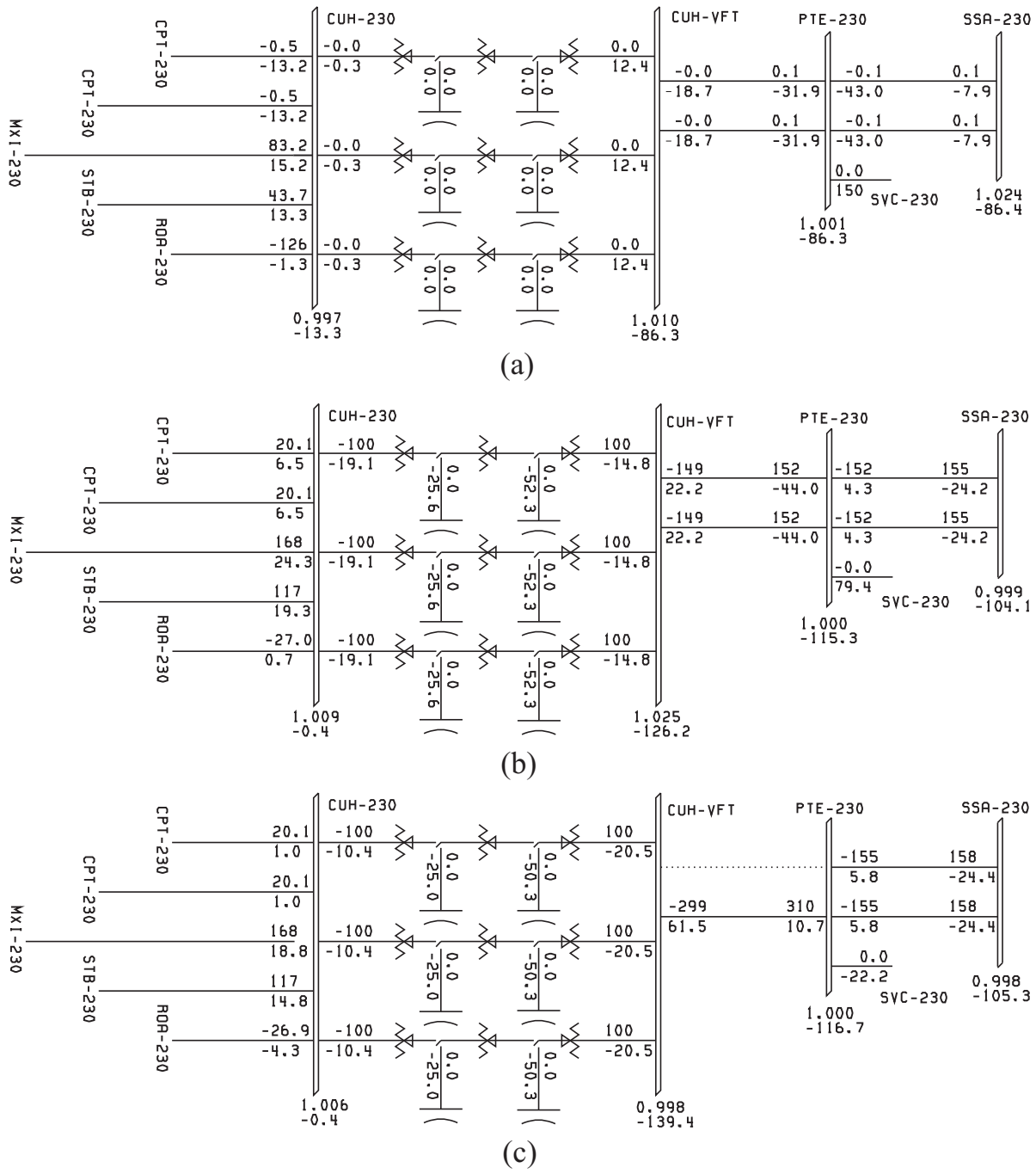

Figure 4.13: Power flow solution for three operating scenarios: (a).- 0 MW power transfer, (b).- 300 MW power transfer and (c).- fault at substation CUH-VFT.

Table 4.3: Power losses in the Mexican link.

Base case	Losses in the link	Losses in the system
0 MW	0.2 MW	1,052.52 MW
300 MW	10 MW	1,084.00 MW
fault	16 MW	1,092.87 MW

Table 4.4: Voltages in the link for different scenarios.

Case base	CUH-230	CUH2-VFT	PTE-230	SSA-230
0 MW	$0.997\angle -13.3$	$1.010\angle -86.3$	$1.001\angle -86.3$	$1.024\angle -86.4$
300 MW	$1.009\angle -0.4$	$1.025\angle -126.2$	$1.000\angle -115.3$	$0.999\angle -104.1$
fault	$1.006\angle -0.4$	$0.998\angle -139.4$	$1.000\angle -116.7$	$0.998\angle -105.3$

network to control the voltage of the PTE-230 substation at 1 pu. The power transfer to the BC system remains at 300 MW, while VFT Park consumes 133.2 MVAR. The reactive power injected by the capacitor banks to the system is 225.9 MVAR.

Table 4.3 summarizes the total power losses for the three operating conditions, whilst Table 4.4 shows the node voltages at the main substations of the Mexican interconnection link. As expected, the fault test case presents the most significant losses with 1092.87 MW because the unfaulted transmission line carries the entire power flow. It can be seen from Table 4.4 that all the substations voltages remain within the security and permissible limits of operation. The angles are very large due to the fact that slack node is located at a great geographical distance.

4.5.2 Transient-Fault Analysis

A three-phase fault is applied at CUH-VFT substation at $t = 2$ seconds and the protection system operate in 0.1 sec (6 cycles). The fault is cleared with the opening of the transmission line connected from the CUH-VFT to PTE-230. The transient solution after a three-phase fault in the CUH-VFT substation is shown in the Figures 4.14, 4.15 and 4.16. On the one hand, Figure 4.14 shows the total power flow through the VFT park. It can be observed that the VFT park recovers the nominal power flow condition in approximately 4 seconds after fault clearing. Figure 4.15 shows the power flow through the AC transmission system from CUH-VFT to PTE-230. It can be appreciated that the 310 MW is transported throughout this transmission line after fault clearing. On the other hand, the reactive power compensation provided by the SVC is shown in Figure 4.16. The SVC pre-fault conditions is 79.4 MVAR inductive and after

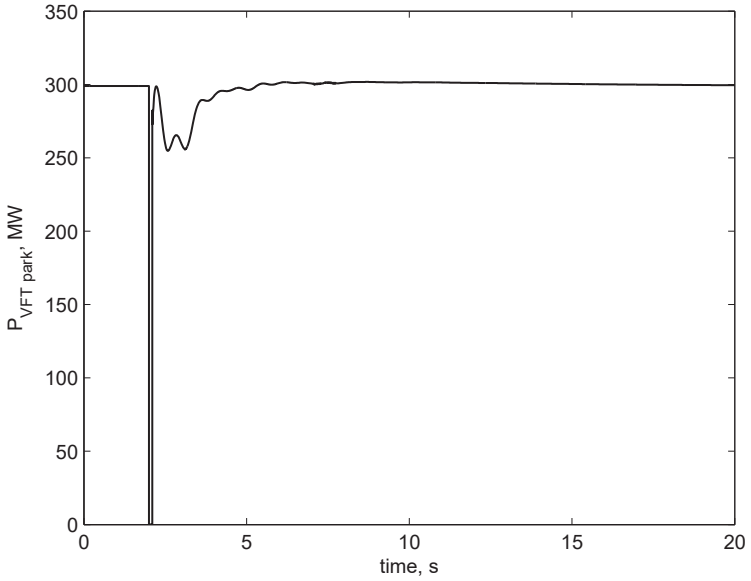

Figure 4.14: Power Flow through the VFT park.

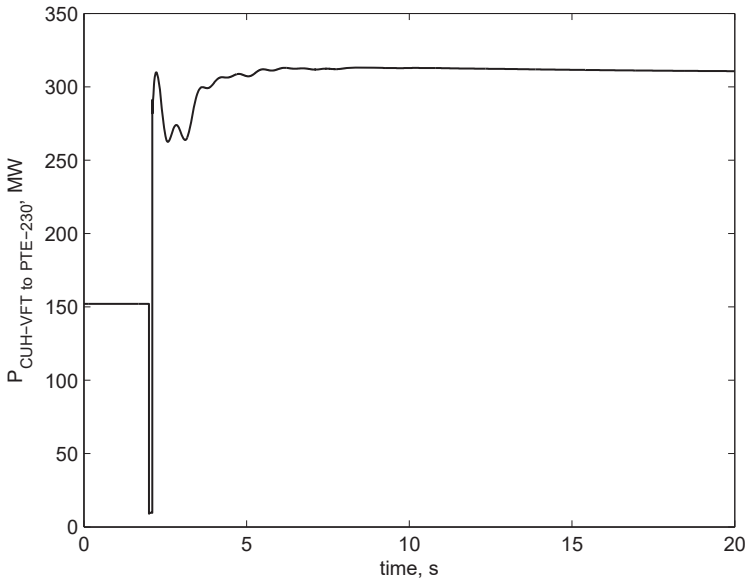

Figure 4.15: Power flow in the AC transmission system between CUH-VFT and PTE-230 nodes.

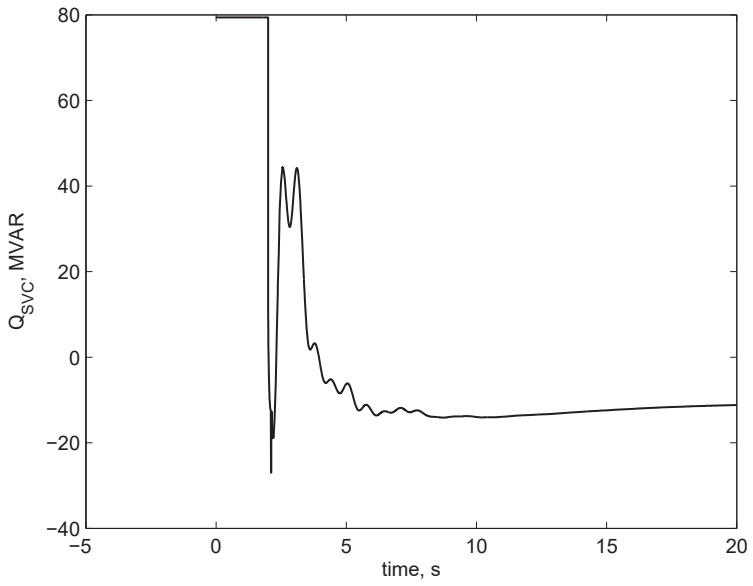

Figure 4.16: Shunt compensation in the Pinacate substation.

fault clearing reaches 22.2 MVAR capacitive. The transient behavior of the SVC shows an increase of reactive power of 101.6 MVAR. Power swings during the transient are observed in these Figures. The power swings are due to the low response of the turbine governor in the synchronous machines of the BC system.

4.6 Test Case III: Mexican Interconnection Link Test System for not Rated Power Transfer

The interconnection link test case reported in the previous test case is now operated with a power transfer of 225 MW. Each VFT is operated with a different power transfer command in order to exchange a total power transfer of 225 MW, where the individual power transfer commands in the VFT park are $\text{VFT}_1 = 75$ MW, $\text{VFT}_2 = 100$ MW and $\text{VFT}_2 = 50$ MW.

4.6.1 Power Flow Analysis

The steady-state analysis of the Mexican interconnection link is carried-out for three main operating conditions: i).- Power transfer exchanged equal to 0 MW, ii).- power transfer of 225 MW in the VFT park and iii).- a fault at the substation CUH-VFT

Table 4.5: Power losses in the Mexican link.

Base case	Losses in the link	Losses in the system
0 MW	0.2 MW	1,052.52 MW
225 MW	6 MW	1,043.50 MW
fault	9 MW	1,047.50 MW

Table 4.6: Voltages in the link for different scenarios.

Case base	CUH-230	CUH-VFT	PTE-230	SSA-230
0 MW	$0.997\angle -13.3$	$1.010\angle -86.3$	$1.001\angle -86.3$	$1.024\angle -86.4$
225 MW	$1.011\angle -4.6$	$1.042\angle -105.4$	$1.000\angle -97.3$	$1.008\angle -89.1$
fault	$1.011\angle -4.6$	$1.036\angle -114.3$	$1.000\angle -98.0$	$1.008\angle -89.6$

and the opening of a transmission line between the CUH-VFT substation and PTE-230 substation. Power flow solutions for this test case are reported in Figure 4.17. It can be observed that for a power transfer equal to 0 MW the capacitor banks are not connected and the reactive power consumption of the VFT Park is 14.5 MVAR. Besides, the SVC consumes its maximum reactive power and maintains the SVC-230 node voltage at 1,001 pu.

For the power transfer scenario, the ISN exports 225 MW to the BC system throughout the VFT park (see Figure 4.17 (b)). The reactive power consumption of the VFT Park is 100.1 MVAR, while the capacitor banks supply 231.8 MVAR. Then, 131.7 MVAR is fed to BC and INS power systems. The SVC controller at PTE-230 consumes 146 MVAR to control the voltage of PTE-230 substation at 1 pu. It can be seen that most of the power flow imported to the BC power system is consumed by the STB-230 and MXI-230 substations.

For the fault test case at CUH-VFT substation, one transmission line circuit between CUH-VFT and PTE-230 is opened, remaining only one transmission line to transmit the entire bulk of energy (see Figure 4.17 (c)). The SVC injects 66.5 MVAR into the network to control the voltage of the PTE-230 substation at 1 pu. The power transfer to the BC system remains at 225 MW, while VFT Park consumes 98.9 MVAR. The reactive power injected by the capacitor banks to the system is 239.1 MVAR.

Table 4.5 summarizes the total power losses for the three operating conditions, whilst Table 4.6 shows the node voltages at the main substations of the Mexican interconnection link. As expected, the fault test case presents the most significant losses with 1047.50 MW because the unfaulted transmission line carries the entire power flow. It can be seen from Table 4.6 that all the substations voltages remain within the security

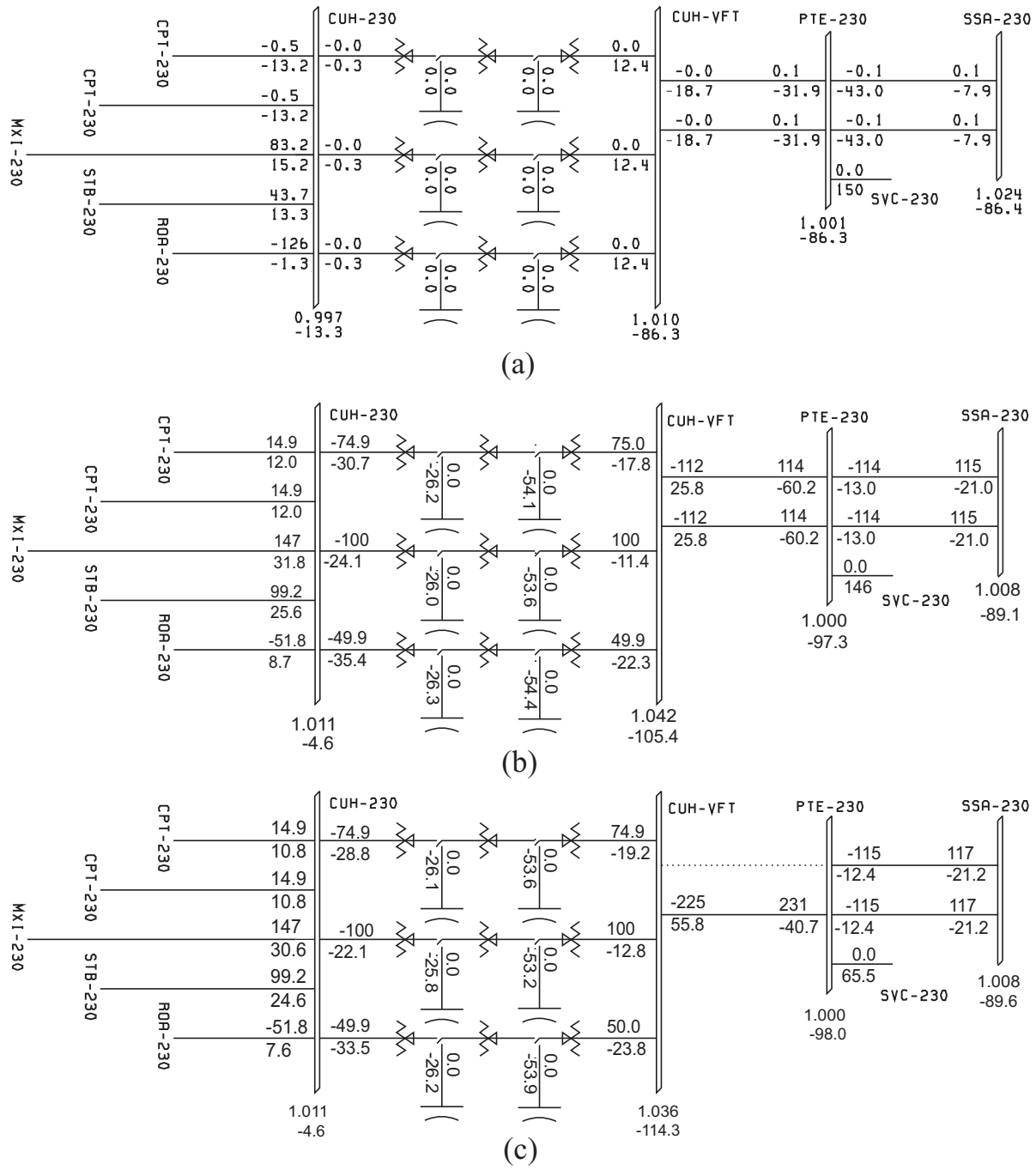

Figure 4.17: Power flow solution for the Mexican interconnection link operated at not rated power transfer: (a).- 0 MW power transfer, (b).- 225 MW power transfer and (c).- fault at substation CUH-VFT.

Table 4.7: Power flows and phase-shift angle in the rotary machine for (a).- power transfer of 300 MW and (b).- power transfer of 225 MW.

	0 MW			300 MW			fault		
	VFT_1	VFT_2	VFT_3	VFT_1	VFT_2	VFT_3	VFT_1	VFT_2	VFT_3
P_{VFT}, MW	0	0	0	100	100	100	100	100	100
Q_{VFT}, MVAR	11.9	11.9	11.9	24.3	24.3	24.3	24.1	24.1	24.1
θ_{VFT}, degrees	-73	-73	-73	-143	-143	-143	-156.8	-156.8	-156.8

(a)

	0 MW			225 MW			fault		
	VFT_1	VFT_2	VFT_3	VFT_1	VFT_2	VFT_3	VFT_1	VFT_2	VFT_3
P_{VFT}, MW	0	0	0	75	100	49.9	74.9	100	50
Q_{VFT}, MVAR	11.9	11.9	11.9	19.9	24.5	16.6	19.8	24.5	16.4
θ_{VFT}, degrees	-73	-73	-73	-113.5	-117.8	-109.2	-122.4	-126.7	-118.2

(b)

and permissible limits of operation. The angles are very large due to the fact that slack node is located at a great geographical distance.

Table 4.7 shows the power flows and phase-shift angle in the rotary machines of the VFT park. Table 4.7 (a) indicates the active power through each VFT, reactive power consumed by each VFT and phase-shift angle of the VFT for 300 MW of power transfer. It can be observed that each VFT unit provides 100 MW. Besides, each VFT unit consume 24.3 MVAR at rated power transfer, while 12 MVAR are consumed for the no power transfer scenario. It can be noted that the phase-shift angle of the VFT is a function of the power transfer and voltage angles on the rotor and stator sides. Table 4.7 (b) shows the active power through of each VFT, reactive power consumed by each VFT and the phase-shift angle across the VFT. It can be observed that the reactive power consumed by the VFT is a function of the active power through the VFT. While the control system of each VFT maintains the active power at the reference power transfer, the reactive power varies from 16.6 MVAR to 24.5 MVAR.

4.6.2 Transient-Fault Analysis

A three-phase fault is applied at CUH-VFT substation at t=2 seconds and the protection system operate in 0.1 sec (6 cycles). The fault is cleared with the opening of the transmission line connected from the CUH-VFT to PTE-230. The transient solution after a three-phase fault in the CUH-VFT substation is shown in the Figures 4.18, 4.19 and 4.20. On the one hand, Figure 4.18 shows the total power flow through the

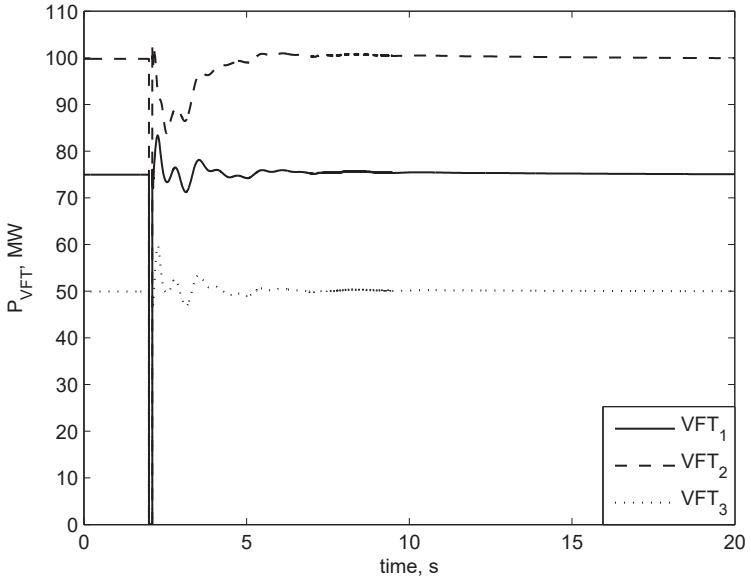

Figure 4.18: Power Flow through the VFT park.

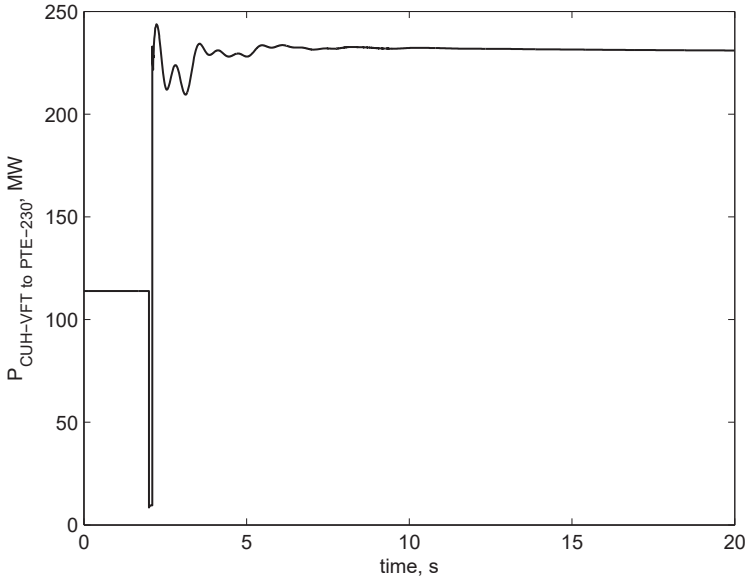

Figure 4.19: Power flow in the AC transmission system between CUH-VFT and PTE-230 nodes.

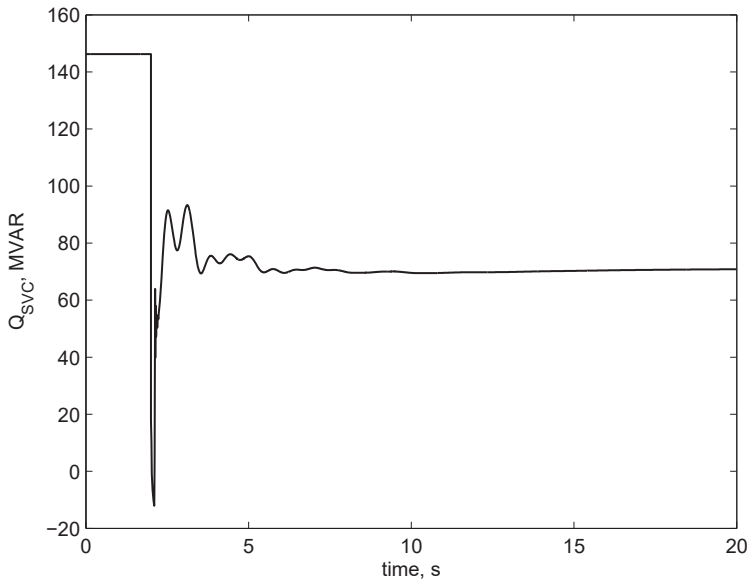

Figure 4.20: Shunt compensation in the Pinacate substation.

VFT park. It can be observed that the VFT park recovers the nominal power flow condition in approximately 3 seconds after fault clearing. Figure 4.19 shows the power flow through the AC transmission system from CUH-VFT to PTE-230. It can be appreciated that the 231 MW is transported throughout this transmission line after fault clearing. On the other hand, the reactive power compensation provided by the SVC is shown in Figure 4.20. The SVC pre-fault condition is 146 MVAR inductive and after fault clearing reaches 65.5 MVAR inductive. Then the SVC control system determines a reduction of 80.5 MVAR. Power swings during transient are observed in these figures. Power swings observed in Figure 4.18 to Figure 4.20 are due to the low response of the turbine governor in the synchronous machines of the BC system.

4.7 Conclusions

A variable frequency transformer model for power flow and transient analyses in PSS/E software is presented in this chapter. The VFT model for steady-state analysis is developed with a phase-shifting transformer model considering a continuos phase shift from -180° to 180°. The VFT model for power flow solution is implemented with a PST model library. The VFT model for transient stability includes a control system that regulates the power flow by adjusting the rotor speed. The power flow analysis of a

VFT park including a realistic power system is including in this chapter. A test case consisting of an asynchronous link in the Mexican power system is presented to show the applicability of the VFT solution to control power flow exchange.

Chapter 5

CONCLUSIONS

This thesis has focused on the investigation and development of models and analysis techniques of interconnection links based on the Variable Frequency Transformer. A procedure to determine the stability of steady-state solutions has been presented in this work using a sequential continuation scheme, eigenvalues analysis and the Newton method. VFT models to carry-out stability, harmonic-oriented and planning studies have been presented. General conclusions of the research carried-out and possible future work guidelines for further improvements and developments are given in this chapter as follows.

5.1 General Conclusions

Stability analyses of variable frequency transformers based on a sequential continuation scheme, eigenvalues and the Newton method were implemented. The continuation scheme was implemented using an efficient predictor-corrector scheme, where the correction was accomplished with the Newton method. This acceleration procedure is based on the application of a Newton-Raphson method and the Poincaré map. More important, eigenvalues were computed with the transition matrix identified with the Newton method using a Direct Approach or a Numerical Differentiation procedure. Indeed, all the information required to implement the stability analysis was provided by the Newton method. Furthermore, a comprehensive VFT park model based on an alternative topology to operate a set of VFT was proposed to study the stability of interconnection links. The VFT park model allows the simulation of multi-unit VFTs operated in parallel in order to increase the power transfer between two electric power

networks with different frequencies or different control strategies. The stability analysis implemented in this thesis was applied to determine the stability of interconnection links using a VFT park. Stability diagrams were reported for changes of the VFT parameters, power transfer and frequency on both sides of the interconnection link. Non-stable regions have been identified for changes of frequency of the asynchronous networks and power transfer. Sustained oscillations on the VFT power transfer have been observed when the VFT park operates in the non-stable region. Stability diagrams show that instability is very likely to occur in VFTs if the rotor circuit is connected to a weak power network presenting variations of frequency. For this reason, it is recommended to connect the rotor side of the VFT to the power system that shows less frequency variations.

A powerful blend based on an implicit integration algorithm and the Newton method was proposed to determine the periodic steady-state solution of nonlinear equations with stiff problems. This alternative allows the efficient computation of the transition matrix involved in the Newton method. A Variable Frequency Transformer model for harmonic-oriented studies using a phase-coordinate representation was developed in this thesis. The nonlinear characteristic associated to the saturation effect in the WRIM was incorporated with an extrapolation formulation for the magnetizing reactance. The application of the Newton method to compute the periodic steady-state solution of the VFT park showed good results in terms of computational effort and number of NR applications. The incorporation of the implicit integration algorithm into the Newton method paved the way to efficiently solve power networks with stiff problems. This time domain approach showed to be particularly useful for the swift determination of the periodic steady-state of the variable frequency transformer because of the inherently large inertia of its rotary machine, which caused prolonged transient response after a system disturbance.

In addition, a VFT model was developed for its application to planning studies of power systems using the PSS/E software. The VFT for power flow studies was implemented with a phase-shifting transformer model included in the PSS/E library. In order to carry-out transient stability studies, the reduced moder of order 2 for the WRIM was implemented using a user written code. A prospective interconnection link in the Mexican power systems was analyzed with the models implemented in PSS/E for power flow and transient stability analyses. These steady-state and dynamic simulations corroborate previous studies carried-out by the department of Programación de Redes

Eléctricas of the CFE using a software developed by General Electric. Therefore, the asynchronous link between the interconnection national system of CFE and the Baja California power network is feasible using a VFT park consisting of three VFT units, for a rated power transfer capability of 300 MW.

It was found that the VFT may demand an important amount of reactive power compensation. The VFT has a magnetizing reactance and leakage reactances that consumes reactive power due to magnetization requirements and as a function of current passing through it, respectively. Therefore, the total reactive power requirement of the rotary machine is a combination of power consumed by the stator and rotor leakage reactances and the reactive power consumed by the magnetizing reactance. The total reactive power demanded by the VFT for no power transfer is mainly related to the magnetizing reactance of the rotary machine, while the total reactive power demanded at rated power transfer is related to the stator and rotor leakage reactance and magnetizing reactance. For this reason, capacitor banks or FACTS controllers must be installed to alleviate reactive power compensation demanded by the VFT and adjacent transmission systems. This reactive power demand represents an inherent requirement of this rotary machine. Therefore, attention must be paid to the economic investments needed to deploy a solution based on VFTs or any other technology.

Finally, it is worthy to mention that the VFT presents important advantages and some drawbacks compared with mature technology such as HVDC or more recent FACTS developments such as HVDC-VSC. So far, two VFT installations are in operation, one more has been commisioned and another one is currently being studied. It is expected that the new VFT installations would be commisioned worldwide in the new future. HVDC and HVDC-VSC solutions offer a fast response to transient disturbances due to the operation of power electronics controllers, while VFT shows relatively slow response due to the large inertia of its rotary machine. However, this characteristic may help to improve the system transient stability by providing a natural damping capability. Regarding harmonic generation, VFT technology offers solutions based on a rotary machine with no harmonic distortion operating under rated conditions and, as a consequence, there is no need to incorporated sophisticated harmonic filter schemes. Further research work must be carried-out to develop economic and technical analyses of VFT and HVDC technologies, with special interest on important subjects such as the transient response power transmission loses and the impact on the stability margins.

5.2 Future Work

The initial objectives of this thesis have been successfully reached through the development of this thesis. However, results also open new questions and new possible improvements. This possible future work is listed as follows:

1. Variable frequency transformer models have demonstrated to be capable to control power flow in asynchronous systems. In order to extend the research reported in this thesis, an interesting suggestion for future research work may be to include the power swing damping characteristic in the control system of the VFT models.

2. Detailed VFT park model can be used to carry-out transient stability studies of large scale systems.

3. Extensive studies on the interaction of the VFT and FACTS controllers are required for prospective VFT projects.

4. Further investigation on the development of new solutions to the interconnection links market using HVDC, HVDC-VSC and VFTs.

5. There are some important niches in the wind power generation which could be satisfied with the application of VFT-based solutions such as interconnection of wind parks using this technology.

6. Application of bifurcation theory for the study of nonlinear phenomena in VFT installations.

Appendix A

Newton Method

The time domain representation of a non-linear electric system can be described as,

$$\dot{\mathbf{x}} = f(t, \mathbf{x}),\ \mathbf{x}(t_0) = \mathbf{x}_0 \tag{A.1}$$

where $\mathbf{x}$ is a m-dimensional state vector and $\mathbf{x}_0$ is the initial condition. If the set of ODEs has a periodic driving force so that $f(t, \cdot)$ is also T-periodic, then it can be represented as a limit cycle for $\mathbf{x}_\infty$ in terms of another periodic element of or in terms of an arbitrary function of period T [Parker89].

Assuming a single transient orbit that starts at x_i and ends at x_{i+1} after one cycle of integration known as cycle base, its dynamic behavior is conveniently described by its intercepts on the Poincaré map Σ (see Figure 2.9). If a disturbance Δx of the state variable is applied at the limit cycle x_∞, then (A.1) takes the form,

$$\dot{x} + \Delta\dot{x} = f(t, x + \Delta x) \tag{A.2}$$

The linearization of (A.2) taking first order terms in the Taylor series expansion results in,

$$\dot{x} + \Delta\dot{x} \approx f(t, x) + J(t, x)\Delta x \tag{A.3}$$

where the matrix of partial derivatives J represents the Jacobian matrix of (2.28). Simplifying (A.3) it follows that

$$\Delta\dot{x} \approx J(t, x)\Delta x \tag{A.4}$$

It has been surmised in [Semlyen95] that the general matrix solution $\Delta x(t)$ at $t = T$ is,

$$\Delta x(T) = \Phi(T)\Delta x(0) \tag{A.5}$$

where

$$\Phi(T) = e^{\int_0^T J(t)dt} \tag{A.6}$$

and Φ is the transition matrix or identification matrix.

The computation of the state variable at the limit cycle using a Newton method is defined as,

$$x_\infty = x_i + (I - \Phi)^{-1}(x_{i+1} - x_i) \tag{A.7}$$

where x_∞ is the state variable at the limit cycle, I is the identity matrix, x_i is the state variable at the beginning of the base cycle and x_{i+1} is the state variable at the end of the base cycle. The identification of matrix Φ can be implemented by mean of Direct Approach (DA) or Numerical Differentiation (ND) procedures [Semlyen95].

A.1 The DA Procedure

The direct approach procedure computes the transition matrix $\mathbf{\Phi}$ by integrating the Jacobian $J(t, x)$ involved in the variational problem (A.4) with a set of sequential perturbations. The initial vectors $\Delta\mathbf{x}_0$ are defined with the following expression [Semlyen95],

$$\Delta\mathbf{x}_i = e_i = [0...1...0]_i^T \tag{A.8}$$

where $i = 1, 2, ..., m$ and e_i are are the column vectors of the identity matrix I. Then from (A.6), the following relation holds for a m-order problem,

$$\Delta\mathbf{x}_{i+1} = \mathbf{\Phi}\Delta\mathbf{x}_i \tag{A.9}$$

Substituting (A.8) in (A.9) results in the following expression,

$$\Delta\mathbf{x}_{i+1} = \mathbf{\Phi}e_i \tag{A.10}$$

Then the identification of the transition matrix $\mathbf{\Phi}$ by columns results in,

$$\mathbf{\Phi} = \Delta \mathbf{x}_{i+1} \tag{A.11}$$

A.2 The ND Procedure

A different approach to the calculation of matrix $\mathbf{\Phi}$ by columns relies on the application of a sequential perturbation in the initial vector of the state variables calculated at the base cycle, where the perturbation is expressed as [Semlyen95],

$$\mathbf{x}_i = \mathbf{x}_0 + \xi e_i = \mathbf{x}_0 + \xi [0...1...0]_i^T \tag{A.12}$$

and ξ is a small value of around $1e^{-6}$ p.u.

This method is based on the numerical differentiation defined as,

$$\mathbf{x}_i - \mathbf{x}_0 = \xi e_i \tag{A.13}$$

Using (A.13) in the expression for an m-order problem described by (A.9), results in the following relationship,

$$\Delta \mathbf{x}_{i+1} = \mathbf{\Phi} \xi e_i \tag{A.14}$$

Consequently, if $i = 1, 2, ..., m$ then $\mathbf{\Phi}$ can be obtained from (A.14),

$$\mathbf{\Phi} = \frac{1}{\xi} \Delta \mathbf{x}_{i+1} \tag{A.15}$$

Appendix B

Implicit Integration Algorithm

A Numerical Differentiation Formulation has the form [Klopfenstein71],

$$\sum_{m=1}^{k} \frac{1}{m} \nabla^m \mathbf{x}_{n+1} - hF(t_{n+1}, \mathbf{x}_{n+1}) - k\gamma_k(\mathbf{x}_{n+1} - \mathbf{x}^0_{n+1}) = 0 \tag{B.1}$$

where ∇^m is the backward difference operator, $\mathbf{x}_{n+1}$ are the state variables at the end of the Newton iteration, $\mathbf{x}^0_{n+1}$ are the state variables at the beginning of the Newton iteration, h is the step size, k is a scalar parameter and γ_k is given by $\gamma_k = \sum_{j=1}^{k} \frac{1}{j}$.

Considering the identity [Shampine97],

$$\sum_{m=1}^{k} \frac{1}{m} \nabla^m \mathbf{x}_{n+1} = \gamma_k(\mathbf{x}_{n+1} - \mathbf{x}^0_{n+1}) + \sum_{m=1}^{k} \gamma_m \nabla^m \mathbf{x}_n \tag{B.2}$$

then (B.1) takes the form,

$$0 = (1-k)\gamma_k(\mathbf{x}_{n+1} - \mathbf{x}^0_{n+1}) + \sum_{m=1}^{k} \gamma_m \nabla^m \mathbf{x}_n - hF(t_{n+1}, \mathbf{x}_{n+1}) \tag{B.3}$$

The new values for the state variables computed with a Newton iteration are,

$$\mathbf{x}^{i+1}_{n+1} = \mathbf{x}^i_{n+1} + \Delta\mathbf{x}^i_{n+1} \tag{B.4}$$

which can be solved using (B.3) as follows,

$$\left(I - \frac{h}{(1-k)\gamma_k} J\right) \Delta \mathbf{x}^i_{n+1} = \frac{h}{(1-k)\gamma_k} F(t_{n+1}, \mathbf{x}^i_{n+1}) - \frac{h}{(1-k)\gamma_k} \sum_{m=1}^{k} \gamma_m \nabla^m \mathbf{x}_n - (\mathbf{x}^i_{n+1} - \mathbf{x}^0_{n+1}) \tag{B.5}$$

where J represents an approximation of the Jacobian of $F(t, \mathbf{x})$.

B.1 Adjustable Time Step

The variable time step required for the time domain solution has been implemented in this work accordingly with the proposal presented in [Shampine97]. The main steps needed to adjust the time step using backward differences and a numerical differentiation formulation are summarized below,

- For the time instant t_n, there are $\mathbf{x}(t_{n-j})$ values previously computed at time step $t_{n-j} = t_n - jh$ for $j = 0, 1, ..., k$. Then, the interpolating polynomial is formed as,

$$P(t) = \mathbf{x}(t_n) + \sum_{j=1}^{k} \nabla^j \mathbf{x}(t_n) \frac{1}{j! h^j} \prod_{m=0}^{j-1} (t - t_{n-m}) \tag{B.6}$$

- If $\nabla^j P(t_n) = \nabla^j \mathbf{x}(t_n)$ and the solution is held by the current values $\mathbf{x}(t_n)$, a table D of backward differences is formed as $D = [\nabla P(t_n), \nabla^2 P(t_n), ..., \nabla^k P(t_n)]$. On the other hand, if a new step is considered in the interpolating polynomial such that $h^* \neq h$, a new table D^* of backward differences can be defined.

- By equating the two interpolating polynomial obtained with the tables of backward differences, then the next identity is obtained

$$\sum_{j=1}^{k} \nabla^{*j} P(t_n) \frac{1}{j! h^{*j}} \prod_{m=0}^{j-1} (t - t^*_{n-m}) = \sum_{j=1}^{k} \nabla^j P(t_n) \frac{1}{j! h^j} \prod_{m=0}^{j-1} (t - t_{n-m}) \tag{B.7}$$

- The evaluation of the identity (B.7) at $t = t^*_{n-r}$ for $r = 1, ..., k$ leads to the system of equations $D^* U_{jr} = D R_{jr}$, where U_{jr} and R_{jr} are defined as follows,

$$U_{jr} = \frac{1}{j!h^{*j}} \prod_{m=0}^{j-1} (t^*_{n-r} - t^*_{n-m}) = \frac{1}{j!} \prod_{m=0}^{j-1} (m - r) \tag{B.8}$$

$$R_{jr} = \frac{1}{j!} \prod_{m=0}^{j-1} (m - r\frac{h^*}{h}) \tag{B.9}$$

where matrix U_{jr} satisfies $U^2_{jr} = \mathrm{I}$. Then, $D^* = D(R_{jr}U_{jr})$ represents the scheme used for changing the time step and R must be formed each time the step size is changed.

Appendix C

Stability of Periodic Solutions

Figure C.1 shows a single-phase nonlinear test case to determine the stability of a periodic steady-state solution based on Floquet theory, the Newton method and the variation of a parameter. The test case comprises of a voltage source $v_s = 1.0 \times sin(\omega t)$, with $\omega = 2\pi 60$. Besides, three transmission lines are represented with equivalent impedances where $r_1 = r_2 = r_3 = 0.01$ pu and $x_1 = x_2 = x_3 = 0.1$ pu. Shunt capacitors are located at nodes 1 and 2 with $C_1 = C_2 = 0.1$ pu. Nonlinear branches comprises a resistance $r_4 = r_5 = 0.1$ pu and the nonlinear current is defined with a polynomial representation $i = \phi^n$, with $n = 3$.

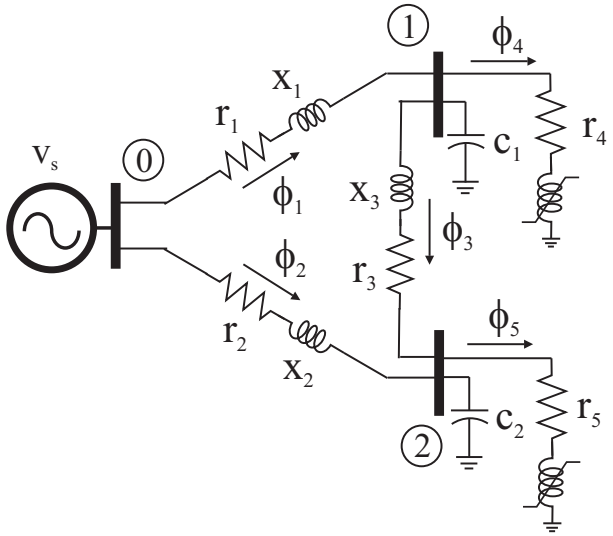

Figure C.1: Single-phase nonlinear test system.

Applying Kirchhoff's laws and solving for flux linkages and voltage nodes is follows,

$$\begin{aligned}
\tfrac{d}{dx}\phi_1 &= \omega(v_s - \mathrm{r}_1\tfrac{\phi_1}{\mathrm{x}_1} - v_{c1}) \\
\tfrac{d}{dx}\phi_2 &= \omega(v_s - \mathrm{r}_1\tfrac{\phi_2}{\mathrm{x}_1} - v_{c2}) \\
\tfrac{d}{dx}\phi_3 &= \omega(v_{c1} - \mathrm{r}_1\tfrac{\phi_3}{\mathrm{x}_1} - v_{c2}) \\
\tfrac{d}{dx}\phi_4 &= \omega(v_{c1} - \mathrm{r}_2\phi_4^3) \\
\tfrac{d}{dx}\phi_5 &= \omega(v_{c2} - \mathrm{r}_2\phi_5^3) \\
\tfrac{d}{dx}v_{c1} &= \tfrac{\omega}{\mathrm{c}_1}(\tfrac{\phi_1}{\mathrm{x}_1} - \tfrac{\phi_3}{\mathrm{x}_1} - \phi_4^3) \\
\tfrac{d}{dx}v_{c2} &= \tfrac{\omega}{\mathrm{c}_2}(\tfrac{\phi_2}{\mathrm{x}_1} + \tfrac{\phi_3}{\mathrm{x}_1} - \phi_5^3)
\end{aligned} \tag{C.1}$$

The Jacobian used in the Direct Approach procedure is defined as,

$$J = \begin{bmatrix}
\omega(-\mathrm{r}_1\frac{\dot{\phi}_1}{\mathrm{x}_1} - \dot{v}_{c1}) \\
\omega(-\mathrm{r}_1\frac{\dot{\phi}_2}{\mathrm{x}_1} - \dot{v}_{c2}) \\
\omega(\dot{v}_{c1} - \mathrm{r}_1\frac{\dot{\phi}_3}{\mathrm{x}_1} - \dot{v}_{c2}) \\
\omega(\dot{v}_{c1} - 3\mathrm{r}_2\phi_4^2\dot{\phi}_4) \\
\omega(\dot{v}_{c2} - 3\mathrm{r}_2\phi_5^2\dot{\phi}_5) \\
\frac{\omega}{\mathrm{c}_1}(\frac{\dot{\phi}_1}{\mathrm{x}_1} - \frac{\dot{\phi}_3}{\mathrm{x}_1} - 3\phi_4^2\dot{\phi}_4) \\
\frac{\omega}{\mathrm{c}_2}(\frac{\dot{\phi}_2}{\mathrm{x}_1} + \frac{\dot{\phi}_3}{\mathrm{x}_1} - 3\phi_5^2\dot{\phi}_5)
\end{bmatrix} \tag{C.2}$$

C.1 Steady-State

An explicit RK4 method is applied to carry-out the integration of the nonlinear system. The time step is h=3.2552e-5 and the maximum mismatch is set to 1×10^{-10} to locate the periodic steady-state solution. Table C.1 summarizes the maximum mismatches during convergence to the periodic steady-state solution using the Newton method with a Numerical Differentiation (ND) and a Direct Approach (DA) procedure, respectively. Five initial cycles of integration are run in order to determine the base cycle.

Table C.1: Errors during convergence to the periodic steady-state solution.

NR	ND	DA
BC	2.498774e-2	2.498774e-2
1	2.883177e-4	2.883010e-4
2	8.068438e-11	8.100116e-11

The state variables at the periodic steady-state,

$$x_\infty = \begin{bmatrix} -7.0522e-2 \\ -7.0522e-2 \\ -2.8634e-14 \\ -9.2292e-1 \\ -9.2292e-1 \\ -1.0999e-2 \\ -1.0999e-2 \end{bmatrix} \tag{C.3}$$

and

$$x_\infty = \begin{bmatrix} -7.0522e-2 \\ -7.0522e-2 \\ 9.8052e-17 \\ -9.2292e-1 \\ -9.2292e-1 \\ -1.0999e-2 \\ -1.0999e-2 \end{bmatrix} \tag{C.4}$$

which are obtained with the ND and DA procedures, respectively.

C.2 Transition Matrix

The transition matrices obtained with the Newton method using a ND and DA procedures are,

$$\Phi_{\text{ND}} = \begin{bmatrix} 0.0181 & -0.2820 & 0.2334 & 0.1180 & 0.0668 & 0.0432 & 0.0051 \\ -0.2820 & 0.0181 & -0.2334 & 0.0668 & 0.1180 & 0.0051 & 0.0432 \\ 0.2334 & -0.2334 & 0.0667 & -0.0512 & 0.0512 & -0.0380 & 0.0380 \\ 0.4597 & 0.2586 & -0.2010 & 0.3343 & -0.0569 & -0.0439 & -0.0056 \\ 0.2586 & 0.4597 & 0.2010 & -0.0569 & 0.3343 & -0.0056 & -0.0439 \\ -4.2988 & -0.4984 & 3.8004 & 1.1476 & 0.1556 & -0.3381 & -0.1162 \\ -0.4984 & -4.2988 & -3.8004 & 0.1556 & 1.1476 & -0.1162 & -0.3381 \end{bmatrix} \tag{C.5}$$

$$\Phi_{\mathrm{DA}} = \begin{bmatrix} 0.0181 & -0.2820 & 0.2334 & 0.1180 & 0.0668 & 0.0432 & 0.0051 \\ -0.2820 & 0.0181 & -0.2334 & 0.0668 & 0.1180 & 0.0051 & 0.0432 \\ 0.2334 & -0.2334 & 0.0667 & -0.0512 & 0.0512 & -0.0380 & 0.0380 \\ 0.4597 & 0.2586 & -0.2010 & 0.3343 & -0.0569 & -0.0439 & -0.0056 \\ 0.2586 & 0.4597 & 0.2010 & -0.0569 & 0.3343 & -0.0056 & -0.0439 \\ -4.2988 & -0.4984 & 3.8004 & 1.1476 & 0.1556 & -0.3381 & -0.1162 \\ -0.4984 & -4.2988 & -3.8004 & 0.1556 & 1.1476 & -0.1162 & -0.3381 \end{bmatrix} \tag{C.6}$$

C.3 Floquet Multipliers

The Floquet multipliers are the eigenvalues of the transition matrices (C.5) and (C.6). Then, the Floquet multipliers for the ND and DA procedures are,

$$\mu_{\mathrm{ND}} = \begin{bmatrix} -4.5061e-1+5.4422e-1i \\ -4.5061e-1-5.4422e-1i \\ -2.1962e-1+6.8683e-1i \\ -2.1962e-1-6.8683e-1i \\ 5.3349e-1 \\ 4.6052e-1 \\ 4.4186e-1 \end{bmatrix} \tag{C.7}$$

and

$$\mu_{\mathrm{DA}} = \begin{bmatrix} -4.5061e-1+5.4422e-1i \\ -4.5061e-1-5.4422e-1i \\ -2.1962e-1+6.8683e-1i \\ -2.1962e-1-6.8683e-1i \\ 5.3349e-1 \\ 4.6052e-1 \\ 4.4186e-1 \end{bmatrix} \tag{C.8}$$

The maximum absolute value of μ for the ND and DA procedures are $max\,|\mu_i| = 7.2109e-1 < 1$. Therefore, this magnitude of the Floquet multiplier indicates that the periodic steady-state solution found is stable.

C.4 Variation of Capacitance C_2

A variation of the parameter C_2 is carried-out in order to determine the stability of this new condition. The capacitance C_2 is modified from $C_1 = 0.1$ pu to $C_2 = 0.2$ pu and the (C.3) and (C.4) are used as a solution predicted by the predictor scheme. The corrector involved in the sequential continuation scheme is achieved by applying the Newton method to the initial conditions provided by the predictor. Then, Table C.2 summarizes the maximum mismatches during convergence to this new periodic steady-state solution using the Newton method with a ND and a DA procedures, respectively.

Table C.2: Errors during convergence to the periodic steady-state solution for $C_2 = 0.2$ pu.

NR	ND	DA
BC	1.680823e-2	1.680823e-2
1	6.735934e-6	6.736434e-6
2	8.321711e-13	2.764906e-13

The new state variables at the steady-state are,

$$x_\infty = \begin{bmatrix} -6.8895e-2 \\ -6.6561e-2 \\ 2.3337e-3 \\ -9.2451e-1 \\ -9.2678e-1 \\ -1.2161e-2 \\ -1.2974e-2 \end{bmatrix} \tag{C.9}$$

and

$$x_\infty = \begin{bmatrix} -6.8895e-2 \\ -6.6561e-2 \\ 2.3337e-3 \\ -9.2451e-1 \\ -9.2678e-1 \\ -1.2161e-2 \\ -1.2974e-2 \end{bmatrix} \tag{C.10}$$

for ND and DA procedures, respectively.

C.5 Transition Matrix

The transition matrix for ND and DA procedure are,

$$\Phi_{\mathrm{ND}} = \begin{bmatrix} 0.0969 & -0.3808 & 0.0558 & 0.0980 & 0.0937 & 0.0314 & -0.0382 \\ -0.3815 & -0.1131 & -0.2651 & 0.0934 & 0.1540 & -0.0190 & -0.0117 \\ 0.0551 & -0.2658 & 0.2126 & -0.0046 & 0.0603 & -0.0504 & 0.0265 \\ 0.3825 & 0.3612 & -0.0213 & 0.3518 & -0.0846 & -0.0320 & 0.0370 \\ 0.3614 & 0.5943 & 0.2329 & -0.0842 & 0.2934 & 0.0185 & 0.0098 \\ -3.1241 & 1.9172 & 5.0413 & 0.8349 & -0.4697 & -0.0601 & -0.4136 \\ 1.9177 & 0.5979 & -1.3197 & -0.4677 & -0.1099 & -0.2080 & -0.5311 \end{bmatrix} \tag{C.11}$$

and

$$\Phi_{\mathrm{DA}} = \begin{bmatrix} 0.0969 & -0.3808 & 0.0558 & 0.0980 & 0.0937 & 0.0314 & -0.0382 \\ -0.3815 & -0.1131 & -0.2651 & 0.0934 & 0.1540 & -0.0190 & -0.0117 \\ 0.0551 & -0.2658 & 0.2126 & -0.0046 & 0.0603 & -0.0504 & 0.0265 \\ 0.3825 & 0.3612 & -0.0213 & 0.3518 & -0.0846 & -0.0320 & 0.0370 \\ 0.3614 & 0.5943 & 0.2329 & -0.0842 & 0.2934 & 0.0185 & 0.0098 \\ -3.1241 & 1.9172 & 5.0413 & 0.8349 & -0.4697 & -0.0601 & -0.4136 \\ 1.9177 & 0.5979 & -1.3197 & -0.4677 & -0.1099 & -0.2080 & -0.5311 \end{bmatrix} \tag{C.12}$$

C.6 Floquet Multipliers

The Floquet multipliers obtained with transition matrices (C.11) and (C.12) are,

$$\mu_{\mathrm{ND}} = \begin{bmatrix} -6.7339e-1+2.1508e-1i \\ -6.7339e-1-2.1508e-1i \\ 8.3211e-2+7.1497e-1i \\ 8.3211e-2-7.1497e-1i \\ 5.3349e-1 \\ 4.5829e-1 \\ 4.3893e-1 \end{bmatrix} \tag{C.13}$$

and

$$\mu_{\mathrm{DA}} = \begin{bmatrix} -6.7339e-1+2.1508e-1i \\ -6.7339e-1-2.1508e-1i \\ 8.3211e-2+7.1497e-1i \\ 8.3211e-2-7.1497e-1i \\ 5.3349e-1 \\ 4.5829e-1 \\ 4.3893e-1 \end{bmatrix} \tag{C.14}$$

The maximum absolute value of μ for the ND and DA procedures is $max\,|\mu_i| = 7.1980e-1 < 1$. Therefore, this value indicates that the stedy state solution is stable. This variation of the parameter strategy is repeated as many times as necessary to determine a desired stability diagram.

Appendix D

Parameters for VFT Models

The VFT and the control system parameters used in the chapters 2 and 3 are shown in Table D.1.

Table D.1: VFT parameters based on 100 MVA rating.

VFT		Control system				DC link and DC motor		Additional parameters	
X_T	10%	K_{pp}	7.00	K_{pT}	1.2	C	0.35 pu	$r_s = r_r$	0.002 pu
X_{VFT}	12%	K_{ip}	0.08	K_{iT}	75	R_a	3.45 pu	$r_{Ts,i} = r_{Tr,i}$	0.009 pu
B shunt	20%	$K_{p\omega}$	0.06	K_{pv}	0.9	L_a	1.173 pu	$x_{Tpc1} = x_{Tpc2}$	0.008 pu
$X_{mag,VFT}$	10 pu	$K_{i\omega}$	0.20	K_{iv}	25	L_{af}	44.5 pu	$r_{Tpc1} = r_{Tpc2}$	0.0098 pu
H	26 pu − s	τ	0.01					D_m	0.540

Table D.2 shows the parameter for the 2250 HP induction machine. These parameters are used in the Chapter 2 for validation of the wound rotor induction machine.

Table D.2: 2250 HP wound rotor indcution machine parameters.

Machine rating										
			T_B	$I_{B(abc)}$	r_s	x_{ls}	X_m	x_{lr}	r_r	J
HP	Volts	RPM	(N.m)	(amps)	(ohms)	(ohms)	(ohms)	(ohms)	(ohms)	$(kg \cdot m)$
2250	2300	1786	8.9×10^3	421.2	0.029	0.226	13.04	0.226	0.022	63.87

Appendix E

Representation of VFT Models in State Space

The models developed in the chapters 2 and 3 can be represented in the general form of state space. The following sections show the general representation of these models.

E.1 VFT Models for Stability Studies

The set of equations can be written in the following form by using vector-matrix notation,

$$\dot{\mathbf{x}} = \mathbf{A}\mathbf{x} + \mathbf{B}\mathbf{u} \tag{E.1}$$

where

$$\mathbf{x} = \left[\begin{array}{cccccccc} \psi^e_{qs,i} & \psi^e_{ds,i} & \psi^e_{qr,i} & \psi^e_{dr,i} & \frac{\omega_{m,i}}{\omega_b} & \theta_{m,i} & y_\omega & y_{\mathrm{T}} \quad \mathrm{T}_{m,i} \end{array} \right]^{\mathrm{T}} \tag{E.2}$$

$$\mathbf{u} = \left[\begin{array}{cccccccc} V^e_{qs,i} & V^e_{ds,i} & V_{qr,i} & V_{dr,i} & 0 & (\omega^e_s - \omega^e_r) & P_{ref,i} & P_{VFT} \quad 0 \end{array} \right]^{\mathrm{T}} \tag{E.3}$$

$$\mathbf{A} = \frac{\omega_b}{X_D}\begin{bmatrix} -r_s X_r & -\frac{\omega_s^e}{\omega_b}X_D & r_s x_m & 0 & 0 & 0 & 0 & 0 & 0 \\ \frac{\omega_s^e}{\omega_b}X_D & -r_s X_r & 0 & r_s x_m & 0 & 0 & 0 & 0 & 0 \\ r_r x_m & 0 & -r_r X_s & -\mathrm{S}X_D & 0 & 0 & 0 & 0 & 0 \\ 0 & r_r x_m & \mathrm{S}X_D & -r_r X_s & 0 & 0 & 0 & 0 & 0 \\ 0 & 0 & \frac{x_m \psi_{ds,i}^e}{2\mathrm{H}} & -\frac{x_m \psi_{qs,i}^e}{2\mathrm{H}} & \frac{\mathrm{D_m X_D}}{2\mathrm{H}} & 0 & 0 & 0 & -\frac{1}{2\mathrm{H}} \\ 0 & 0 & 0 & 0 & \omega_b X_D & 0 & 0 & 0 & 0 \\ 0 & 0 & 0 & 0 & 0 & 0 & 0 & 0 & 0 \\ 0 & 0 & 0 & 0 & 0 & 0 & K_{i\omega} & 0 & 0 \\ 0 & 0 & 0 & 0 & -K_{i\omega} - \frac{K_{p\omega}}{\tau} & 0 & \frac{K_{p\omega}}{\tau} & \frac{1}{\tau} & -\frac{1}{\tau} \end{bmatrix} \tag{E.4}$$

and

$$\mathbf{B} = \begin{bmatrix} 1 & 0 & 0 & 0 & 0 & 0 & 0 & 0 & 0 \\ 0 & 1 & 0 & 0 & 0 & 0 & 0 & 0 & 0 \\ 0 & 0 & cos(-\theta_{m,i}) & -sin(-\theta_{m,i}) & 0 & 0 & 0 & 0 & 0 \\ 0 & 0 & sin(-\theta_{m,i}) & cos(-\theta_{m,i}) & 0 & 0 & 0 & 0 & 0 \\ 0 & 0 & 0 & 0 & 0 & 0 & 0 & 0 & 0 \\ 0 & 0 & 0 & 0 & 0 & 1 & 0 & 0 & 0 \\ 0 & 0 & 0 & 0 & 0 & 0 & K_{ip} & -K_{ip} & 0 \\ 0 & 0 & 0 & 0 & 0 & 0 & K_{i\omega}K_{pp} & -K_{i\omega}K_{pp} & 0 \\ 0 & 0 & 0 & 0 & 0 & 0 & \frac{K_{p\omega}K_{pp}}{\tau} & -\frac{K_{p\omega}K_{pp}}{\tau} & 0 \end{bmatrix} \tag{E.5}$$

with

$$\mathrm{S} = \frac{\omega_s^e - \omega_{m,i}}{\omega_b} \tag{E.6}$$

where ψ is the flux linkage, the superscript e denotes the synchronous reference frame, the subscript i indicates the WRIM number ($i = 1, ..., n$), ω_b is the base angular velocity, ω_s^e is the stator angular velocity, r_s is the stator resistance, r_r is the rotor resistance, I_{qs}^e is the quadrature-axis stator current, I_{ds}^e is the direct-axis stator current, I_{qr}^e is the quadrature-axis rotor current, I_{dr}^e is the direct-axis rotor current, V_{qs}^e is the quadrature-axis stator voltage, V_{ds}^e is the direct-axis stator voltage, V_{qr}^e is the quadrature-axis rotor voltage, V_{dr}^e is the direct-axis rotor voltage, T_e is the electromagnetic torque, T_m is the

mechanic torque, ω_m is the rotor speed, θ_m is the rotor position, H is the constant of inertia, D_m is the damping coefficient and ω_r^e is the rotor angular velocity.

The currents through the WRIM in terms of the flux linkages are,

$$\begin{bmatrix} I_{qs,i}^e \\ I_{ds,i}^e \\ I_{qr,i}^e \\ I_{dr,i}^e \end{bmatrix} = \frac{1}{X_D} \begin{bmatrix} X_r & 0 & -x_m & 0 \\ 0 & X_r & 0 & -x_m \\ -x_m & 0 & X_s & 0 \\ 0 & -x_m & 0 & X_s \end{bmatrix} \begin{bmatrix} \psi_{qs,i}^e \\ \psi_{ds,i}^e \\ \psi_{qr,i}^e \\ \psi_{dr,i}^e \end{bmatrix} \tag{E.7}$$

with $X_s = x_s + x_m$, $X_r = x_r + x_m$, $X_D = X_s X_r - x_m^2$. Moreover, x_s is the stator leakage reactance, x_r is the rotor leakage reactance and x_m is the magnetizing reactance [Krause94].

WRIM Fourth-Order Model

For the reduced fourth order model the set of equations (E.21) is conformed as,

$$\mathbf{x} = \begin{bmatrix} \psi_{qr,i}^e & \psi_{dr,i}^e & \frac{\omega_{m,i}}{\omega_b} & \theta_{m,i} & y_\omega & y_\mathrm{T} & \mathrm{T}_{m,i} \end{bmatrix}^\mathrm{T} \tag{E.8}$$

$$\mathbf{u} = \begin{bmatrix} V_{qr,i} & V_{dr,i} & 0 & (\omega_s^e - \omega_r^e) & P_{ref,i} & P_{VFT} & 0 \end{bmatrix}^\mathrm{T} \tag{E.9}$$

$$\mathbf{A} = \frac{\omega_b}{X_D} \begin{bmatrix} -r_r X_s & -\mathrm{S}X_D & 0 & 0 & 0 & 0 & 0 \\ \mathrm{S}X_D & -r_r X_s & 0 & 0 & 0 & 0 & 0 \\ \frac{x_m \psi_{ds,i}^e}{2\mathrm{H}} & -\frac{x_m \psi_{qs,i}^e}{2\mathrm{H}} & \frac{\mathrm{D_m X_D}}{2\mathrm{H}} & 0 & 0 & 0 & -\frac{1}{2\mathrm{H}} \\ 0 & 0 & \omega_b X_D & 0 & 0 & 0 & 0 \\ 0 & 0 & 0 & 0 & 0 & 0 & 0 \\ 0 & 0 & 0 & 0 & K_{i\omega} & 0 & 0 \\ 0 & 0 & -K_{i\omega} - \frac{K_{p\omega}}{\tau} & 0 & \frac{K_{p\omega}}{\tau} & \frac{1}{\tau} & -\frac{1}{\tau} \end{bmatrix} \tag{E.10}$$

and

$$\mathbf{B} = \begin{bmatrix} cos(-\theta_{m,i}) & -sin(-\theta_{m,i}) & 0 & 0 & 0 & 0 & 0 \\ sin(-\theta_{m,i}) & cos(-\theta_{m,i}) & 0 & 0 & 0 & 0 & 0 \\ 0 & 0 & 0 & 0 & 0 & 0 & 0 \\ 0 & 0 & 0 & 1 & 0 & 0 & 0 \\ 0 & 0 & 0 & 0 & K_{ip} & -K_{ip} & 0 \\ 0 & 0 & 0 & 0 & K_{i\omega} K_{pp} & -K_{i\omega} K_{pp} & 0 \\ 0 & 0 & 0 & 0 & \frac{K_{p\omega} K_{pp}}{\tau} & -\frac{K_{p\omega} K_{pp}}{\tau} & 0 \end{bmatrix} \tag{E.11}$$

The stator and rotor currents can be computed as,

$$\begin{bmatrix} I^e_{qs,i} \\ I^e_{ds,i} \\ I^e_{qr,i} \\ I^e_{dr,i} \end{bmatrix} = \begin{bmatrix} X_D & -r_s X_r & 0 & 0 \\ r_s X_r & X_D & 0 & 0 \\ 0 & -r_s x_m & X_D & 0 \\ -r_s x_m & 0 & 0 & X_D \end{bmatrix}^{-1} \begin{bmatrix} 0 & -X_r & -x_m & 0 \\ X_r & 0 & 0 & -x_m \\ 0 & x_m & X_s & 0 \\ -x_m & 0 & 0 & X_s \end{bmatrix} \begin{bmatrix} V^e_{qs,i} \\ V^e_{ds,i} \\ \psi^e_{qr,i} \\ \psi^e_{dr,i} \end{bmatrix} \tag{E.12}$$

WRIM Second-Order Model

For the second order model the set of equations (E.21) is,

$$\mathbf{x} = \begin{bmatrix} \frac{\omega_{m,i}}{\omega_b} & \theta_{m,i} & y_\omega & y_{\mathrm{T}} & \mathrm{T}_{m,i} \end{bmatrix}^{\mathrm{T}} \tag{E.13}$$

$$\mathbf{u} = \begin{bmatrix} T_{e,i} & (\omega^e_s - \omega^e_r) & P_{ref,i} & P_{VFT} & 0 \end{bmatrix}^{\mathrm{T}} \tag{E.14}$$

$$\mathbf{A} = \frac{\omega_b}{X_D} \begin{bmatrix} \frac{\mathrm{D_m X_D}}{\mathrm{2H}} & 0 & 0 & 0 & -\frac{1}{\mathrm{2H}} \\ \omega_b X_D & 0 & 0 & 0 & 0 \\ 0 & 0 & 0 & 0 & 0 \\ 0 & 0 & K_{i\omega} & 0 & 0 \\ -K_{i\omega} - \frac{K_{p\omega}}{\tau} & 0 & \frac{K_{p\omega}}{\tau} & \frac{1}{\tau} & -\frac{1}{\tau} \end{bmatrix} \tag{E.15}$$

and

$$\mathbf{B} = \begin{bmatrix} 1 & 0 & 0 & 0 & 0 \\ 0 & 1 & 0 & 0 & 0 \\ 0 & 0 & K_{ip} & -K_{ip} & 0 \\ 0 & 0 & K_{i\omega}K_{pp} & -K_{i\omega}K_{pp} & 0 \\ 0 & 0 & \frac{K_{p\omega}K_{pp}}{\tau} & -\frac{K_{p\omega}K_{pp}}{\tau} & 0 \end{bmatrix} \tag{E.16}$$

The stator and rotor currents can be computed as,

$$\begin{bmatrix} I^e_{qs,i} \\ I^e_{ds,i} \\ I^e_{qr,i} \\ I^e_{dr,i} \end{bmatrix} = \begin{bmatrix} X_s & -r_s & x_m & 0 \\ r_s & X_s & 0 & x_m \\ x_m & 0 & X_r & -\mathrm{S}^{-1} r_r \\ 0 & x_m & \mathrm{S}^{-1} r_r & X_r \end{bmatrix}^{-1} \begin{bmatrix} V^e_{qs,i} \\ V^e_{ds,i} \\ -\mathrm{S}^{-1} V^e_{qr,i} \\ \mathrm{S}^{-1} V^e_{dr,i} \end{bmatrix} \tag{E.17}$$

E.1.1 Capacitor Banks and Conventional Transformers

The transients associated with the remaining components of the VFT park can be neglected in order to obtain a set of algebraic equations. The transient associated to these components decays very rapidly and there is little justification for modeling their effects in transient stability studies [Kundur94]. Hence, the transformers' currents on the stator and rotor side of each WRIM can be computed applying Kirchhoff's current law at nodes V_s and V_r as follows,

$$\begin{bmatrix} I_{qTs,i} \\ I_{dTs,i} \\ I_{qTr,i} \\ I_{dTr,i} \end{bmatrix} = \begin{bmatrix} 0 & \omega_s^e \mathrm{C}_{s,i} & 0 & 0 \\ -\omega_s^e \mathrm{C}_{s,i} & 0 & 0 & 0 \\ 0 & 0 & 0 & \omega_r^e \mathrm{C}_{r,i} \\ 0 & 0 & -\omega_r^e \mathrm{C}_{r,i} & 0 \end{bmatrix} \begin{bmatrix} V_{qs,i}^e \\ V_{ds,i}^e \\ V_{qr,i}^e \\ V_{dr,i}^e \end{bmatrix} + \begin{bmatrix} I_{qs,i}^e \\ I_{ds,i}^e \\ I_{qr,i}^e \\ I_{dr,i}^e \end{bmatrix} \tag{E.18}$$

where C_s is the capacitance at the stator side and C_r is the capacitance at the rotor side. The voltages at the points of common coupling (PCC) V_{pc1} and V_{pc2} can be expressed algebraically by applying Kirchhoff's voltage law on the stator and rotor sides as follows,

$$\begin{bmatrix} V_{q\mathrm{pc1}} \\ V_{d\mathrm{pc1}} \\ V_{q\mathrm{pc2}} \\ V_{d\mathrm{pc2}} \end{bmatrix} = - \begin{bmatrix} r_{\mathrm{Tpc1}} & x_{\mathrm{Tpc1}} & 0 & 0 \\ -x_{\mathrm{Tpc1}} & r_{\mathrm{Tpc1}} & 0 & 0 \\ 0 & 0 & r_{\mathrm{Tpc2}} & x_{\mathrm{Tpc2}} \\ 0 & 0 & -x_{\mathrm{Tpc2}} & r_{\mathrm{Tpc2}} \end{bmatrix} \begin{bmatrix} \sum_{i=1}^{n} I_{qTs,i} \\ \sum_{i=1}^{n} I_{dTs,i} \\ \sum_{i=1}^{n} I_{qTr,i} \\ \sum_{i=1}^{n} I_{dTr,i} \end{bmatrix} + \begin{bmatrix} V_{qk} \\ V_{dk} \\ V_{qm} \\ V_{dm} \end{bmatrix} \tag{E.19}$$

where I_{qTs} is the quadrature-axis current through the conventional transformer connected to WRIM at the stator side, I_{dTs} is the direct-axis current through the conventional transformer connected to WRIM at the stator side, I_{qTr} is the quadrature-axis current through the conventional transformer connected to WRIM at the rotor side, I_{dTr} is the direct-axis current through the conventional transformer connected to WRIM at the rotor side, V_{qk} is the quadrature-axis voltage at power systems k, V_{dk} is the direct-axis voltage at power systems k, V_{qm} is the quadrature-axis voltage at power systems m and V_{dm} is the direct-axis voltage at power systems m. In addition, r_{Tpc1} and x_{Tpc1} are the resistance and reactance of the power transformer connected at power network k, while r_{Tpc2} and x_{Tpc2} are the resistance and reactance of the power transformer connected at power network m.

The new values for voltages V_s and V_r at each WRIM to be used in the next integration step can be computed applying Kirchhoff's voltage law. Then,

$$\begin{bmatrix} V^e_{qs,i} \\ V^e_{ds,i} \\ V_{qr,i} \\ V_{dr,i} \end{bmatrix} = - \begin{bmatrix} r_{\mathrm{T}s} & x_{\mathrm{T}s} & 0 & 0 \\ -x_{\mathrm{T}s} & r_{\mathrm{T}s} & 0 & 0 \\ 0 & 0 & r_{\mathrm{T}r} & x_{\mathrm{T}r} \\ 0 & 0 & -x_{\mathrm{T}r} & r_{\mathrm{T}r} \end{bmatrix} \begin{bmatrix} I_{qTs,i} \\ I_{dTs,i} \\ I_{qTr,i} \\ I_{dTr,i} \end{bmatrix} + \begin{bmatrix} V_{q\mathrm{pc1}} \\ V_{d\mathrm{pc1}} \\ V_{q\mathrm{pc2}} \\ V_{d\mathrm{pc2}} \end{bmatrix} \tag{E.20}$$

where $r_{\mathrm{T}s}$ and $x_{\mathrm{T}s}$ are the resistance and reactance of the conventional power transformer connected at the stator side, $r_{\mathrm{T}r}$ and $x_{\mathrm{T}r}$ are the resistance and reactance of the conventional power transformer connected at the rotor side.

E.2 VFT Model in Phase-Coordinate Representation

The VFT model for phase coordinate-representation is a set of 41 ODEs, then the set of equations can be written in the following form by using vector-matrix notation,

$$\dot{\mathbf{x}} = \boldsymbol{f}(\boldsymbol{x}, \boldsymbol{t}) \tag{E.21}$$

$$\mathbf{x} = \begin{bmatrix} \boldsymbol{x}_1 & \boldsymbol{x}_2 & \boldsymbol{x}_3 & \boldsymbol{x}_4 & \boldsymbol{x}_5 & \boldsymbol{x}_6 \end{bmatrix} \tag{E.22}$$

Then the state variables are,

$$\boldsymbol{x}_1 = \begin{bmatrix} i^{abc}_k & i^{abc}_m & \frac{\omega_m}{\omega_b} & \theta_m \end{bmatrix}^{\mathrm{T}} \tag{E.23}$$

$$\boldsymbol{x}_2 = \begin{bmatrix} i^{abc}_{pri,k} & i^{abc}_{sec,k} & \psi^{abc}_{mag,k} \end{bmatrix}^{\mathrm{T}} \tag{E.24}$$

$$\boldsymbol{x}_3 = \begin{bmatrix} i^{abc}_{pri,m} & i^{abc}_{sec,m} & \psi^{abc}_{mag,m} \end{bmatrix}^{\mathrm{T}} \tag{E.25}$$

$$\boldsymbol{x}_4 = \begin{bmatrix} v^{abc}_{C,k} & i^{abc}_{C,m} \end{bmatrix}^{\mathrm{T}} \tag{E.26}$$

$$\boldsymbol{x}_5 = \begin{bmatrix} i_a & i_b & i_c & V_C & I_a \end{bmatrix}^{\mathrm{T}} \tag{E.27}$$

$$\boldsymbol{x}_6 = \begin{bmatrix} y_v & y_{\mathrm{C}} & y_\omega & y_{\mathrm{T}} \end{bmatrix}^{\mathrm{T}} \tag{E.28}$$

with the function defines as,

$$\boldsymbol{f}(\boldsymbol{x},\boldsymbol{t}) = \begin{bmatrix} \boldsymbol{f}_1 & \boldsymbol{f}_2 & \boldsymbol{f}_3 & \boldsymbol{f}_4 & \boldsymbol{f}_5 & \boldsymbol{f}_6 \end{bmatrix}^{\mathrm{T}} \tag{E.29}$$

where

$$\boldsymbol{f}_1 = \omega_b \left[\mathbf{L}^{-1}(\mathbf{v}^{abc}_{k,m} - (\mathbf{r}_{k,m} + \mathbf{G}_{k,m}) \cdot \mathbf{i}^{abc}_{k,m})\right] \tag{E.30}$$

$$\boldsymbol{f}_2 = \begin{bmatrix} \frac{\omega_b}{\mathrm{x}_p}\left(\frac{v^a_k}{a} - (r_p + r_c)i^a_{p,k} + r_c(i^a_{s,k} + 0.000\,7\psi^a_{m,k} + 0.000\,83(\psi^a_{m,k})^{19})\right) \\ \frac{\omega_b}{\mathrm{x}_p}\left(\frac{v^b_k}{a} - (r_p + r_c)i^b_{p,k} + r_c(i^b_{s,k} + 0.000\,7\psi^b_{m,k} + 0.000\,83(\psi^b_{m,k})^{19})\right) \\ \frac{\omega_b}{\mathrm{x}_p}\left(\frac{v^c_k}{a} - (r_p + r_c)i^c_{p,k} + r_c(i^c_{s,k} + 0.000\,7\psi^c_{m,k} + 0.000\,83(\psi^c_{m,k})^{19})\right) \\ \frac{\omega_b}{\mathrm{x}_s}\left(-v^{ab}_{C,k} - (r_s + r_c)i^a_{s,k} + r_c(i^a_{p,k} - (0.000\,7\psi^a_{m,k} + 0.000\,83(\psi^a_{m,k})^{19}))\right) \\ \frac{\omega_b}{\mathrm{x}_s}\left(-v^{bc}_{C,k} - (r_s + r_c)i^b_{s,k} + r_c(i^b_{p,k} - (0.000\,7\psi^b_{m,k} + 0.000\,83(\psi^b_{m,k})^{19}))\right) \\ \frac{\omega_b}{\mathrm{x}_s}\left(-v^{ca}_{C,k} - (r_s + r_c)i^c_{s,k} + r_c(i^c_{p,k} - (0.000\,7\psi^c_{m,k} + 0.000\,83(\psi^c_{m,k})^{19}))\right) \\ \omega_b r_c(i^a_{p,k} - i^a_{s,k} - (0.000\,7\psi^a_{m,k} + 0.000\,83(\psi^a_{m,k})^{19})) \\ \omega_b r_c(i^b_{p,k} - i^b_{s,k} - (0.000\,7\psi^b_{m,k} + 0.000\,83(\psi^b_{m,k})^{19})) \\ \omega_b r_c(i^c_{p,k} - i^c_{s,k} - (0.000\,7\psi^c_{m,k} + 0.000\,83(\psi^c_{m,k})^{19})) \end{bmatrix} \tag{E.31}$$

$$\boldsymbol{f}_3 = \begin{bmatrix} \frac{\omega_b}{\mathrm{x}_p}\left(\frac{v^a_m}{a} - (r_p + r_c)i^a_{p,m} + r_c(i^a_{s,m} + 0.000\,7\psi^a_{m,m} + 0.000\,83(\psi^a_{m,m})^{19})\right) \\ \frac{\omega_b}{\mathrm{x}_p}\left(\frac{v^b_m}{a} - (r_p + r_c)i^b_{p,m} + r_c(i^b_{s,m} + 0.000\,7\psi^b_{m,m} + 0.000\,83(\psi^b_{m,m})^{19})\right) \\ \frac{\omega_b}{\mathrm{x}_p}\left(\frac{v^c_m}{a} - (r_p + r_c)i^c_{p,m} + r_c(i^c_{s,m} + 0.000\,7\psi^c_{m,m} + 0.000\,83(\psi^c_{m,m})^{19})\right) \\ \frac{\omega_b}{\mathrm{x}_s}\left(-v^{ab}_{C,m} - (r_s + r_c)i^a_{s,m} + r_c(i^a_{p,m} - (0.000\,7\psi^a_{m,m} + 0.000\,83(\psi^a_{m,m})^{19}))\right) \\ \frac{\omega_b}{\mathrm{x}_s}\left(-v^{bc}_{C,m} - (r_s + r_c)i^b_{s,m} + r_c(i^b_{p,m} - (0.000\,7\psi^b_{m,m} + 0.000\,83(\psi^b_{m,m})^{19}))\right) \\ \frac{\omega_b}{\mathrm{x}_s}\left(-v^{ca}_{C,m} - (r_s + r_c)i^c_{s,m} + r_c(i^c_{p,m} - (0.000\,7\psi^c_{m,m} + 0.000\,83(\psi^c_{m,m})^{19}))\right) \\ \omega_b r_c(i^a_{p,m} - i^a_{s,m} - (0.000\,7\psi^a_{m,m} + 0.000\,83(\psi^a_{m,m})^{19})) \\ \omega_b r_c(i^b_{p,m} - i^b_{s,m} - (0.000\,7\psi^b_{m,m} + 0.000\,83(\psi^b_{m,m})^{19})) \\ \omega_b r_c(i^c_{p,m} - i^c_{s,m} - (0.000\,7\psi^c_{m,m} + 0.000\,83(\psi^c_{m,m})^{19})) \end{bmatrix} \tag{E.32}$$

$$\boldsymbol{f}_4 = \begin{bmatrix} \frac{\omega_b}{\mathrm{x}_C}\left(i^a_{s,k} - i^c_{s,k} - i^a_k - i_a + i_c\right) \\ \frac{\omega_b}{\mathrm{x}_C}\left(i^b_{s,k} - i^a_{s,k} - i^b_k - i_b + i_a\right) \\ \frac{\omega_b}{\mathrm{x}_C}\left(i^c_{s,k} - i^b_{s,k} - i^c_k - i_c + i_b\right) \\ \frac{\omega_b}{\mathrm{x}_C}\left(i^a_{s,m} - i^c_{s,m} - i^a_m\right) \\ \frac{\omega_b}{\mathrm{x}_C}\left(i^b_{s,m} - i^a_{s,m} - i^b_m\right) \\ \frac{\omega_b}{\mathrm{x}_C}\left(i^c_{s,m} - i^b_{s,m} - i^c_m\right) \end{bmatrix} \tag{E.33}$$

$$\boldsymbol{f}_5 = \begin{bmatrix} \left(v^{ab}_{C,k} - r_l i_a - (V^{Sw}_C(1) - V^{Sw}_C(2))\right)\frac{1}{\mathrm{L}_l} \\ \left(v^{bc}_{C,k} - r_l i_b - (V^{Sw}_C(2) - V^{Sw}_C(3))\right)\frac{1}{\mathrm{L}_l} \\ \left(v^{ca}_{C,k} - r_l i_c - (V^{Sw}_C(3) - V^{Sw}_C(1))\right)\frac{1}{\mathrm{L}_l} \\ \left(\begin{bmatrix} i_a & i_b & i_c \end{bmatrix}\begin{bmatrix} Sw_a \\ Sw_b \\ Sw_c \end{bmatrix} - \frac{V_a I_a}{V_\mathrm{C}}\right)\frac{1}{\mathrm{C}} \\ (\frac{V_\mathrm{C}}{v_{tri}} y_v + \mathrm{K_{pT}}(\mathrm{T_{mcd}} - \mathrm{L_{af}i_f I_a}) - R_a I_a - L_{af} I_f \omega_m)\frac{1}{L_a} \end{bmatrix} \tag{E.34}$$

$$\boldsymbol{f}_6 = \begin{bmatrix} \mathrm{K_{iT}}(y_\mathrm{T} + \mathrm{K_{pw}}(y_\omega + \mathrm{K_{pp}}(\mathrm{P_{cmd}} - \mathrm{P_e}) - \frac{\omega_m}{\omega_b}) - L_{af} i_f I_a) \\ \mathrm{K_{iv}}(\mathrm{V_C} - \mathrm{V_{ref}}) \\ \mathrm{K_{ip}}(\mathrm{P_{cmd}} - \mathrm{P_e}) \\ K_{iw}(y_\omega + \mathrm{K_{pp}}(\mathrm{P_{cmd}} - \mathrm{P_e}) - \frac{\omega_m}{\omega_b}) \end{bmatrix} \tag{E.35}$$

with

$$\mathbf{L} = \begin{bmatrix} \mathbf{L}_s & \mathbf{L}_{sr} \\ \mathbf{L}^\mathrm{T}_{sr} & \mathbf{L}_r \end{bmatrix} \tag{E.36}$$

and

$$\mathbf{L}_s = \begin{bmatrix} L_{ls} + L_m & -\frac{1}{2}L_m & -\frac{1}{2}L_m \\ -\frac{1}{2}L_m & L_{ls} + L_m & -\frac{1}{2}L_m \\ -\frac{1}{2}L_m & -\frac{1}{2}L_m & L_{ls} + L_m \end{bmatrix} \tag{E.37}$$

$$\mathbf{L}_r = \begin{bmatrix} L_{lr} + L_m & -\frac{1}{2}L_m & -\frac{1}{2}L_m \\ -\frac{1}{2}L_m & L_{lr} + L_m & -\frac{1}{2}L_m \\ -\frac{1}{2}L_m & -\frac{1}{2}L_m & L_{lr} + L_m \end{bmatrix} \tag{E.38}$$

$$\mathbf{L}_{sr} = \begin{bmatrix} cos\theta_m & cos(\theta_m + \frac{2\pi}{3}) & cos(\theta_m - \frac{2\pi}{3}) \\ cos(\theta_m - \frac{2\pi}{3}) & cos\theta_m & cos(\theta_m + \frac{2\pi}{3}) \\ cos(\theta_m + \frac{2\pi}{3}) & cos(\theta_m - \frac{2\pi}{3}) & cos\theta_m \end{bmatrix} \tag{E.39}$$

where the inductances L_{ls}, L_{lr} and L_m are the stator leakage, rotor leakage indutances and magnetizing inductance, respectively. Besides, $\mathrm{T_e}$ is the electromagnetic torque, H is the constant of inertia, $\mathrm{T_m}$ is the mechanic torque supplied by the control system, $\mathrm{D_m}$ is the damping coefficient, the Sw are the PWM switching functions of each phase defined as,

$$\begin{bmatrix} Sw_a \\ Sw_b \\ Sw_c \end{bmatrix} = \frac{m_a}{2} \begin{bmatrix} sin(\omega_b t + \alpha) \\ sin(\omega_b t - \frac{2\pi}{3} + \alpha) \\ sin(\omega_b t + \frac{2\pi}{3} + \alpha) \end{bmatrix}, \tag{E.40}$$

m_a is the amplitude modulation ratio [Mohan95] and α is the PWM control angle, C is capacitance of the DC-link, L_a is inductance of the DC motor, R_a is resistance of the DC motor, L_{af} is the mutual inductance of the DC motor, I_f is the DC motor field current, a transformer ratio, r_p is the resistance at the primary side, r_s is the resistance at the secondary side, r_c is the resistance associated to core losses, i_m is the magnetizing current, x_p is the reactance at the primary side, x_s is the reactance at the secondary side, v_k is the voltage at the primary side, v_i is the voltage at the secondary side, $\mathrm{K_{ip}}$ is the integral gain of the power regulator, $\mathrm{K_{pp}}$ is the proportional gain of the power regulator, $\mathrm{K_{i\omega}}$ is the integral gain of the speed regulator, $\mathrm{K_{p\omega}}$ is the proportional gain of the speed regulator, $\mathrm{K_{iT}}$ is the integral gain of the torque regulator, $\mathrm{K_{pT}}$ is the proportional gain of the torque regulator, $\mathrm{K_{i}}_v$ is the integral gain of the voltage regulator and $\mathrm{K_{p}}v$ is the proportional gain of the voltage regulator.

Appendix F

Test Systems Files for PSS/E

A power flow raw data file which describes the test system of 9 nodes and 5 nodes are presented bellow.

0, 100.00 / PSS/E-29.0 SUN, JAN 23 2011 11:48
SISTEMA DE PRUEVA VFT
UMSNH-CFE
101,'NORTH ', 138.0000,3, 0.000, 0.000, 2, 2,1.04000, 6.0698, 1
102,'SOUTH ', 138.0000,2, 0.000, 0.000, 2, 2,1.02500, 4.2048, 1
103,'LAKE ', 138.0000,1, 0.000, 0.000, 2, 2,0.97875, 2.2993, 1
104,'MAIN ', 138.0000,1, 0.000, 0.000, 2, 2,0.97092, 1.1228, 1
105,'ELM ', 138.0000,1, 0.000, 0.000, 2, 2,0.94359, -1.8358, 1
201,'GEN-1 ', 16.5000,3, 0.000, 0.000, 1, 1,1.04000, 0.0000, 1
202,'GEN-2 ', 18.0000,2, 0.000, 0.000, 1, 1,1.02500, 4.0971, 1
203,'GEN-3 ', 13.8000,2, 0.000, 0.000, 1, 1,1.02500, -1.8559, 1
204,'BUS-4 ', 138.0000,1, 0.000, 0.000, 1, 1,1.01966, -5.4322, 1
205,'BUS-5 ', 138.0000,1, 0.000, 0.000, 1, 1,0.99198, -7.8991, 1
206,'NOD_6 ', 138.0000,1, 0.000, 0.000, 1, 1,0.98976, -11.5340, 1
207,'BUS-7 ', 138.0000,1, 0.000, 0.000, 1, 1,1.02364, -1.4748, 1
208,'BUS-8 ', 138.0000,1, 0.000, 0.000, 1, 1,1.01214, -5.0410, 1
209,'BUS-9 ', 138.0000,1, 0.000, 0.000, 1, 1,1.02720, -4.5675, 1
300,'VFT2 ', 17.2000,1, 0.000, 25.000, 3, 3,0.98281, 8.2635, 1
400,'VFT1 ', 17.2000,1, 0.000, 25.000, 3, 3,0.99462, -17.3695, 1
0 / END OF BUS DATA, BEGIN LOAD DATA
102,'1 ',1, 2, 2, 20.000, 10.000, 0.000, 0.000, 0.000, 0.000, 2
103,'2 ',1, 2, 2, 90.000, 30.000, 0.000, 0.000, 0.000, 0.000, 1
104,'3 ',1, 2, 2, 80.000, 20.000, 0.000, 0.000, 0.000, 0.000, 1
105,'4 ',1, 2, 2, 115.000, 35.000, 0.000, 0.000, 0.000, 0.000, 2
205,'1 ',1, 5, 51, 125.000, 50.000, 0.000, 0.000, 0.000, 0.000, 1
206,'1 ',1, 6, 61, 90.000, 30.000, 0.000, 0.000, 0.000, 0.000, 1
208,'1 ',1, 8, 81, 100.000, 35.000, 0.000, 0.000, 0.000, 0.000, 1
0 / END OF LOAD DATA, BEGIN GENERATOR DATA
101,'4 ', 93.458, 17.298, 300.000, -300.000,1.04000, 0, 100.000, 0.00000, 0.15048, 0.00000, 0.00000,
1.00000,1, 100.0, 300.000, 0.000, 2,1.0000
102,'5 ', 120.000, 75.300, 300.000, -300.000,1.02500, 0, 100.000, 0.00000, 0.23002, 0.00000, 0.00000,

1.00000,1, 100.0, 120.000, 0.000, 2,1.0000
201,'1 ', 174.286, 45.000, 300.000, -300.000,1.04000, 0, 100.000, 0.00000, 0.15048, 0.00000, 0.00000,
1.00000,1, 100.0, 300.000, 0.000, 1,1.0000
202,'2 ', 163.000, 10.163, 300.000, -300.000,1.02500, 0, 100.000, 0.00000, 0.23002, 0.00000, 0.00000,
1.00000,1, 100.0, 163.000, 0.000, 1,1.0000
203,'3 ', 85.000, -1.828, 300.000, -40.000,1.02500, 0, 100.000, 0.00000, 0.23206, 0.00000, 0.00000,
1.00000,1, 100.0, 85.000, 0.000, 1,1.0000
0 / END OF GENERATOR DATA, BEGIN BRANCH DATA
101, -102,'1 ', 0.02000, 0.06000, 0.00000, 0.00, 0.00, 0.00, 0.00000, 0.03000, 0.00000, 0.03000,1, 0.00, 2,1.0000
101, -103,'2 ', 0.08000, 0.24000, 0.00000, 0.00, 0.00, 0.00, 0.00000, 0.02500, 0.00000, 0.02500,1, 0.00, 2,1.0000
102, -103,'3 ', 0.06000, 0.18000, 0.00000, 0.00, 0.00, 0.00, 0.00000, 0.02000, 0.00000, 0.02000,1, 0.00, 2,1.0000
102, -104,'4 ', 0.06000, 0.18000, 0.00000, 0.00, 0.00, 0.00, 0.00000, 0.02000, 0.00000, 0.02000,1, 0.00, 2,1.0000
102, -105,'5 ', 0.04000, 0.12000, 0.00000, 0.00, 0.00, 0.00, 0.00000, 0.01500, 0.00000, 0.01500,1, 0.00, 2,1.0000
103, -104,'6 ', 0.01000, 0.03000, 0.00000, 0.00, 0.00, 0.00, 0.00000, 0.01000, 0.00000, 0.01000,1, 0.00, 1,1.0000
104, -105,'7 ', 0.08000, 0.24000, 0.00000, 0.00, 0.00, 0.00, 0.00000, 0.02500, 0.00000, 0.02500,1, 0.00, 1,1.0000
204, 205,'1 ', 0.01000, 0.08500, 0.00000, 0.00, 0.00, 0.00, 0.00000, 0.08800, 0.00000, 0.08800,1, 0.00, 1,1.0000
204, 206,'1 ', 0.01700, 0.09200, 0.00000, 0.00, 0.00, 0.00, 0.00000, 0.07900, 0.00000, 0.07900,1, 0.00, 1,1.0000
205, 207,'1 ', 0.03200, 0.16100, 0.00000, 0.00, 0.00, 0.00, 0.00000, 0.15300, 0.00000, 0.15300,1, 0.00, 1,1.0000
206, 209,'1 ', 0.03900, 0.17000, 0.00000, 0.00, 0.00, 0.00, 0.00000, 0.17900, 0.00000, 0.17900,1, 0.00, 1,1.0000
207, 208,'1 ', 0.00850, 0.07200, 0.00000, 0.00, 0.00, 0.00, 0.00000, 0.07450, 0.00000, 0.07450,1, 0.00, 1,1.0000
208, 209,'1 ', 0.01190, 0.10080, 0.00000, 0.00, 0.00, 0.00, 0.00000, 0.10450, 0.00000, 0.10450,1, 0.00, 1,1.0000
0 / END OF BRANCH DATA, BEGIN TRANSFORMER DATA
300, 103, 0,'1 ',1,1,1, 0.00000, 0.00000,2,'VFT_LAKE',1, 106,1.0000 0.00000, 0.10000, 100.00
1.00000, 0.000, 0.000, 150.00, 165.00, 165.00, 0, 0, 1.10000, 0.90000, 1.10000, 0.90000, 33,
0, 0.00000, 0.00000 1.00000, 0.000
201, 204, 0,'1 ',1,1,1, 0.00000, 0.00000,1,' ',1, 1,1.0000 0.00000, 0.05760, 100.00
1.00000, 0.000, 0.000, 0.00, 0.00, 0.00, 0, 0, 1.50000, 0.90000, 1.10000, 0.51000, 33,
0, 0.00000, 0.00000 1.00000, 0.000
202, 207, 0,'1 ',1,1,1, 0.00000, 0.00000,1,' ',1, 1,1.0000 0.00000, 0.06250, 100.00
1.00000, 0.000, 0.000, 0.00, 0.00, 0.00, 0, 0, 1.50000, 0.51000, 1.10000, 0.90000, 33,
0, 0.00000, 0.00000 1.00000, 0.000
203, 209, 0,'1 ',1,1,1, 0.00000, 0.00000,1,' ',1, 1,1.0000 0.00000, 0.05860, 100.00
1.00000, 0.000, 0.000, 0.00, 0.00, 0.00, 0, 0, 1.50000, 0.51000, 1.10000, 0.90000, 33,
0, 0.00000, 0.00000 1.00000, 0.000
400, 206, 0,'1 ',1,1,1, 0.00000, 0.00000,2,'N6_VFT ',1, 106,1.0000 0.00000, 0.10000, 100.00
1.00000, 0.000, 0.000, 150.00, 165.00, 165.00, 0, 0, 1.10000, 0.90000, 1.10000, 0.90000, 33,
0, 0.00000, 0.00000 1.00000, 0.000
300, 400, 0,'1 ',1,1,1, 0.00000, -0.18000,2,'VFT ',1, 106,1.0000 0.00134, 0.12000, 100.00
1.00000, 0.000, 32.679, 150.00, 165.00, 165.00, 3, 0,180.0000,-180.000,-99.9000,-100.000, 33,
0, 0.00000, 0.00000 1.00000, 0.000
0 / END OF TRANSFORMER DATA, BEGIN AREA DATA
0 / END OF AREA DATA, BEGIN TWO-TERMINAL DC DATA
0 / END OF TWO-TERMINAL DC DATA, BEGIN VSC DC LINE DATA
0 / END OF VSC DC LINE DATA, BEGIN SWITCHED SHUNT DATA
0 / END OF SWITCHED SHUNT DATA, BEGIN IMPEDANCE CORRECTION DATA
0 / END OF IMPEDANCE CORRECTION DATA, BEGIN MULTI-TERMINAL DC DATA
0 / END OF MULTI-TERMINAL DC DATA, BEGIN MULTI-SECTION LINE DATA
0 / END OF MULTI-SECTION LINE DATA, BEGIN ZONE DATA
0 / END OF ZONE DATA, BEGIN INTER-AREA TRANSFER DATA
0 / END OF INTER-AREA TRANSFER DATA, BEGIN OWNER DATA
0 / END OF OWNER DATA, BEGIN FACTS DEVICE DATA

0 / END OF FACTS DEVICE DATA

The data of machines and controllers are,

201 'GENROU' 1 9.48000 0.200000E-01 0.990000 0.350000E-01 9.55 1 2.10000 1.98000 0.220000 0.350000
0.160000 0.150000 0.100000 0.250000 /
202 'GENROU' 2 9.48000 0.200000E-01 0.990000 0.350000E-01 3.33 1 2.10000 1.98000 0.220000 0.350000
0.160000 0.150000 0.100000 0.250000 /
203 'GENROU' 3 7.60000 0.300000E-01 0.500000 0.400000E-01 2.35 1 1.52000 1.48000 0.156000 0.289000
0.966000E-01 0.828000E-01 0.757000E-01 0.273000 /
101 'GENROU' 4 7.60000 0.300000E-01 0.500000 0.400000E-01 5.33 1 1.52000 1.48000 0.156000 0.289000
0.966000E-01 0.828000E-01 0.757000E-01 0.273000 /
102 'GENROU' 5 5.96000 0.330000E-01 0.580000 0.600000E-01 2.35 1 1.54000 1.51000 0.279000 0.399000
0.190000 0.126000 0.270000E-01 0.157000 /
201 'EXAC4' 1 0.200000E-01 0.170000 -.170000 1.50000 11.8000 495.000 0.600000E-01 5.54200 -4.98800
0.123000/
202 'EXAC4' 2 0.200000E-01 0.170000 -.170000 1.50000 11.8000 495.000 0.600000E-01 5.54200 -4.98800
0.123000/
203 'IEEEX1' 3 0.200000E-01 300.000 0.500000E-01 0.00000 0.00000 7.40000 -6.20000 1.00000 1.80000
0.500000 1.80000 0.00000 0.00000 0.00000 0.00000 0.00000 /
101 'IEEEX1' 4 0.200000E-01 300.000 0.500000E-01 0.00000 0.00000 7.40000 -6.20000 1.00000 1.80000
0.500000 1.80000 0.00000 0.00000 0.00000 0.00000 0.00000 /
102 'EXST1' 5 0.405000E-02 0.200000 -.190000 2.20000 42.0000 1000.00 0.00000 12.0000 -12.0000 0.00000
0.00000 1.00000 /
201 'GGOV1' 1 1 0 0.500000E-01 1.00000 0.500000E-01 -.500000E-01 0.700000 0.100000E-01 1.00000
15.0000 1.00000 0.00000 0.500000 1.00000 0.200000E-01 8.00000 3.50000 0.00000 1.00000 0.500000
0.200000 0.613027 0.00000 0.100000 -1.00000 0.100000E-02 0.100000E-01 1.00000 5.00000 261.000 0.00000
4.00000 5.00000 99.0000 -99.0000 /
202 'GGOV1' 2 1 0 0.500000E-01 1.00000 0.500000E-01 -.500000E-01 0.700000 0.100000E-01 1.00000
15.0000 1.00000 0.00000 0.500000 1.00000 0.200000E-01 8.00000 3.50000 0.00000 1.00000 0.500000
0.200000 0.613027 0.00000 0.100000 -1.00000 0.100000E-02 0.100000E-01 1.00000 5.00000 261.000 0.00000
4.00000 5.00000 99.0000 -99.0000 /
203 'IEEEST' 3 3 0 0.00000 0.00000 0.00000 0.00000 0.00000 0.00000 0.100000E-01 0.500000E-01 0.400000E-01
0.400000E-01 5.60000 5.60000 -.100000 0.500000E-01 -.500000E-01 0.00000 0.00000 /
101 'GGOV1' 4 1 0 0.500000E-01 1.00000 0.500000E-01 -.500000E-01 0.700000 0.100000E-01 1.00000 15.0000
1.00000 0.00000 0.500000 1.00000 0.200000E-01 8.00000 3.50000 0.00000 1.00000 0.500000 0.200000 0.613027
0.00000 0.100000 -1.00000 0.100000E-02 0.100000E-01 1.00000 5.00000 261.000 0.00000 4.00000 5.00000 99.0000
-99.0000 /
202 'GGOV1' 5 1 0 0.500000E-01 1.00000 0.500000E-01 -.500000E-01 0.700000 0.100000E-01 1.00000 15.0000
1.00000 0.00000 0.500000 1.00000 0.200000E-01 8.00000 3.50000 0.00000 1.00000 0.500000 0.200000 0.613027
0.00000 0.100000 -1.00000 0.100000E-02 0.100000E-01 1.00000 5.00000 261.000 0.00000 4.00000 5.00000 99.0000
-99.0000 /
0 'USRMDL' 0 'VFT' 8 0 6 42 12 43
400 300 1 400 300 1 100.000 24.300 0.150 0.300 0.010 0.020 0.003 0.055 0.020 0.100 0.055 0.060 1.000
0.100 0.050 0.050 500.000 500.000 0.020 75.000 4.000 0.200 0.025 1800.000 48.000 3.150 2.730 2.500 5.000
0.700 0.950 3.000 0.300 1.150 0.010 0.010 0.010 0.010 0.300 1.500 1.500 0.010/

Bibliography

[Adams08] J. Adams et al. "Planning for Uncertainty: NYISO Planning Process and Smart Grid", in *Proc. IEEE Power Engineering Society General Meeting*, Pittsburgh USA, pp. 1-4, July 2008.

[Ajjarapu92] V. Ajjarapu and B. Lee, "Bifurcation Theory and its Application to Nonlinear Dynamical Phenomena in an Electrical Power System", *IEEE Transactions on Power Systems*, vol. 7, No. 1, pp. 424-431, Feb. 1992.

[Andersen05] B. R. Andersen, "VSC Transmission Tutorial", *CIGRE meeting*, Bangalore, India, pp. 1-22, Sept. 2005.

[Aprille72] T. J. Aprille and T. N. Trick, "A Computer Algorithm to Determine the Steady State Response of Nonlinear Oscillator", *IEEE Transactions on Circuit Theory*, vol. 9, No. 4, pp. 354-360, 1972.

[Arrillaga98a] J. Arrillaga, *High Voltage Direct Current Transmission*, IEE Power and Energy Series, London U. K. 1998.

[Arrillaga98b] J. Arrillaga and B. Smith, *AC-DC Power System Analysis*, the Institution of Electrical Engineers, London U.K. 1998.

[Astrom95] K. Astrom and T. Hagglund, *PID Controllers: Theory, Desing and Tuning*, Swedden: Instrument Society of America, 1995.

[Bagen07] B. Bagen, D. Jacobson, G. Lane and H. M. Turanli, "Evaluation of the Performance of Back-to-Back HVDC Converter and Variable Frequency Transformer for Power Flow Control in a Weak Interconnection", in *Proc. IEEE Power Engineering Society General Meeting*, pp. 1-6, June 2007.

[Bahrman07] M. P. Bahrman and B. K. Johnson, "The ABCs of HVSC Transmission Technologies", *IEEE Power & Energy Magazine*, vol. 5 no. 2, pp. 32-44, March/April 2007.

[Banerjee01] S. Banerjee and G. C. Verghese, *Nonlinear phenomena in power electronics*, IEEE press: New York, 2001.

[Caliskan99] V. A. Caliskan, G. C. Verghese and A. M. Stankovic, "Multifrequency averaging of DC/DC converters", *IEEE Transactions on Power Electronics*, vol. 14, no. 1, pp. 124-133, Jan. 1999.

[Campos01] R. G. Campos and L. O. Pimentel, "A finite-dimensional representation of the quantum angular momentum operator", *Nuovo Cimento* B, vol. 116, no. 1, pp. 31-45, Jan. 2001.

[Carvajal07] H. R. Carvajal-Pérez, "Análisis Multiparamétrico de Bifurcaciones en Sistemas Eléctricos" M. Sc. Thesis in the Facultad de Ingeniería Eléctrica, UMSNH, Morelia 2007.

[Chen05] G. Chen y X. Zhou, "Digital Simulation of Variable Frequency Transformers for Asynchronous Interconnection in Power System", in *Proc. IEEE PES Conference and Exposition in Africa*, pp. 1-6, June 2005.

[Chiang93] H. D. Chiang, C.W. Liu, P. Varaiya, F.F. Wu and M.G. Lauby, "Chaos in a simple power system", *IEEE Trans. on power systems*. vol. 8, No. 4, pp. 1407–1417. Nov. 1993.

[Contreras07] L. Contreras-Aguilar and N. García "Periodic Solutions of Stiff Systems Using the Limit Cycle Method and an Implicit Integration Technique", in *Proc. International Power Engineering Conference*, Singapore Singapore, pp. 1216-1221, Dec. 2007.

[Contreras08] L. Contreras-Aguilar and N. Garcia, "Accelerated Time Domain Solutions of a VFT Using the Poincaré Map Method with an Embedded Implicit Integration Algorithm", in *Proc. North American Power Symposium*, Calgary Canada, pp. 1-8, September 2008.

[Contreras09a] L. Contreras-Aguilar and N. Garcia, "Fast Convergence to the Steady-State Operating Point of a VFT Park Using the Limit Cycle Method and a

Reduced Order Model", in *Proc. IEEE Power Engineering Society General Meeting*, Calgary Canada, pp. 1-5, July 2009.

[Contreras09b] L. Contreras-Aguilar and N. Garcia, "Steady-State Solution of a VFT Park Using the Newton Method and a Reduced Order Model", in *Proc. IEEE PowerTech*, Bucharest Rumania, pp. 1-6, June-July 2009.

[Dalmau00] J. B. Dalmau and P. P. Schonwalder "A Discrete-Time Approach to the Steady-State and Stability Analysis of Distributed Nonlinear Autonomous Circuits", *IEEE Trans. on Circuits and Systems I: Fundamental Theory and Applications*, vol. 47, No. 2, pp. 231-236, Feb. 2000.

[Dobson89] I. Dobson and H. D. Chiang, "Towards a theory of voltage collapse in electric power systems", *Systems & Control Letters*, Vol. 13, pp. 253-262. April 1989.

[Dommel94] H. W. Dommel, *Electromagnetic Transient Program, Theory Book*, Canadian/American EMTP user group, July 1994.

[Donescu99] V. Donescu, A. Charette, Z. Yao and V. Rajagopalan, "Modeling and Simulation of Saturated Induction Motors in Phase Quantities", *IEEE Transactions on Energy Conversion*, vol. 14, No. 3, pp. 386-393, Sep. 1999.

[El-Din10] A. H. El-Din, M. A. Ashraf and M. Ibrahim, "A New Simulink Model to study the VFT performance when transferring power between Weak and Strong AC Grids", in *Proc. International Middle East Power Systems Conference*, Cairo Egypt, pp. 20-24, Dec. 2010.

[López01] F. A. López et al.,"A Discrete-Time Technique for the Steady State Analysis of Nonlinear Switched Circuits with Inconsistent Initial Conditions", *IEEE Symposium on Circuits and Systems*, vol. 3, pp. 6-9, May 2001.

[Fujita00] H. Fujita, S. Ihara, E. V. Larsen and W. W. Price, "Basic Characteristics of a Rotary Power flow Controller" in *Proc. IEEE Power Engineering Society Winter Meeting*, Vol. 2, pp. 1477-1482, Jan. 2000.

[Fujita01] H. Fujita, S. Ihara, E. V. Larsen, E. R. Pratico and W. W. Price, "Modeling and dynamic performance of a rotary power flow controller", in *Proc. IEEE Power Engineering Society Winter Meeting*, vol. 2, pp. 599-604, Jan-Feb. 2001.

[Funaki00] T. Funaki and K. Matsuura, "Feasibility of the low frequency AC transmission", in *Proc. IEEE PES winter meeting*, pp. 2693-2698, vol. 4, 2000.

[S.García01] S. García and A. Medina, "A state space three-phase multilimb transformer model in the time domain: fast periodic steady state analysis" in *Proc. IEEE Power Engineering Society Summer Meeting*, vol. 3, pp 1859 – 1864, 2001.

[S.García00] S. García, A. Medina and C. Perez, "A state space single-phase transformer model incorporating nonlinear phenomena of magnetic saturation and hysteresis for transient and periodic steady-state análisis", in *Proc. IEEE Power Engineering Society Summer*, IEEE 2417 – 2421, vol. 4, 2000.

[García00] N. Garcia and A. Medina, "Fast periodic steady state solution of systems containing thyristor switched capacitors", in *Proc. IEEE Power Engineering Society Summer Meeting*, vol. 2, Seattle, USA, pp. 1-6, July 2000.

[García04] N. García and E. Acha, "Periodic Steady-State Analysis of Large-Scale Electric Systems Using Poincaré Map and Parallel Processing", *IEEE Transaction on Power Systems*, vol. 19, no. 4, pp. 1784-1793, Nov. 2004.

[Garcia05] N. García, "Harmonic and power-Quality Ananlyses of Large-Sacle Electric Systems with STATCOMs: a Time Domain and Paralle Processinf Approach", *5th WSEAS Cobference*, Tenerife, Spain, pp. 1-9, Dec 16-18, 2005.

[Garcia02] N. García, E. Acha and A. Medina, "Application of Newton methods and parallel processing to the solution of electric Systems", *14th PSCC Conference*, Sevilla, Spain, 24-28, June 2002.

[Gómez06] M. A. Gómez-Martínez, "Aplicación de la Teoría de Bifurcaciones en el Análisis de las Oscilaciones No-Lineales Producidas por el Horno de Arco Eléctrico de Corriente Alterna" Doctor in Sciences Thesis in the Facultad de Ingeniería Eléctrica, UMSNH, Morelia 2006.

[Hassink07] P. Hassink, V. Beauregard, R. O'Keefe, E. V. Larsen and R. Bodo, "Second y Future Applications of Stability Enhancement in ERCOT with Asynchronous Interconnections", in *Proc. IEEE Power Engineering Society General Meeting*, pp. 1-7, June 2007.

[Hassink08] P. Hassink, P. E. Marken, R. O'Keefe and G. R. Trevino, "Improving Power System Dynamic Performance in Laredo, TX", in *Proc. PES Transmission and Distribution Conference and Exposition*, pp. 1-5, April 2008.

[Hingorani00] N. G. Hingorani and L. Gyugyi, *Understanding FACTS, Concepts and Technology of Flexible AC Transmission Systems*, IEEE Power Engineering Society, IEEE press, 2000.

[Hughes99] Wm. L. Hughes, "Feasibility of Exchanging Large Blocks of Power Between Unsynchronized Grids by Purely Electromechanical Means", in *Proc. IEEE Power Engineering Society Summer Meeting*, vol. 2, pp. 1158-1162, 1999.

[Kasusky03] R. G. Kasusky, C. R. Fuerte-Esquivel and D. Torres-Lucio, "Assessment of the SVC's effect on nonlinear instabilities and voltage collapse in electric power systems", in *Proc. IEEE Power Engineering Society General Meeting*, Toronto Canada, pp. 2659-2666, July 2003.

[Kieny91a] C. Kieny, "Application of the Bifurcation Theory in Studying and Understanding the Global Behavior of a Ferroresonant Electric Power Circuit", *IEEE Transactions on Power Delivery*, vol. 6, No. 2, pp. 866-872, April 1991.

[Kieny91b] C. Kieny, G. Le Roy and A. Sbai, "Ferroresonance Study Using Galerkin Method with Pseudo-Arclength Continuation Method", *IEEE Transactions on Power Delivery*, vol. 6, No. 4, pp. 1841-1847, Oct. 1991.

[Klopfenstein71] R. W. Klopfenstein, "Numerical Differentiation Formulas for Stiff Systems of Ordinary Differential Equations", RCA Review 32, pp. 447-462, 1971.

[Krause79] P. C. Krause, F. Nozari, T. L. Skvarenina and D. W. Olive, "The Theory of Neglecting Stator Transients", *IEEE Transactions on Power Apparatus and Systems*, vol. 98, No.1 Jan.-Feb. 1979.

[Krause94] P. C. Krause, O. Wasynczuk and S. D. Sudhoff, *Analysis of Electric Machinery*, New York, McGraw-Hill, 1994.

[Kundur94] P. Kundur, *Power System Stability and Control*, New York: McGraw-Hill, 1994.

[Kwatny86] H. G. Kwatny, A. K. Pasrija and L. Y. Bahar, "Static Bifurcations in Electric Power Networks: Loss of Steady-State Stability, and Voltage Collapse", *IEEE Transactions on Circuits and Systems*, vol. 33, No. 10, pp. 981-991, Oct. 1986.

[Larruskain05] D. M. Larruskain, I. Zamora, A. J. Mazón, O. Abarrategui and J. Monasterio "Transmission and Distribution Networks: AC versus DC", in *Proc. 9 Congreso Hispano-Luso de Ingeniería Eléctrica*, Marbella España, June- July, 2005.

[Larsen99] E. V. Larsen "A Classical Approach to Constructing a Power Flow Controller" in *Proc. IEEE Power Engineering Society Summer Meeting*, vol. 2, pp. 1192-1195, July 1999.

[Larsson01] T. Larsson, A. Petersson, A. Edris, D. Kidd and F. Aboytes, "Eagle Pass Back-to-Back Tie: A Dual Purpose Application of Voltage Source Converter Technology", in *Proc. IEEE Power Engineering Society Summer Meeting*, pp. 1686-1691, July 2001.

[Li09] X. Li and C. A. Cañizares, "Chaotic behavior observations in a power system model", in *Proc. IEEE PowerTech*, Bucharest Rumania, pp. 1-5, June-July 2009.

[Marken08] P. Marken, J. Roedel, D. Nadeau, D. Wallace and H. Mongeau, "VFT Maintenance and Operating Performance", in *Proc. PES General Meeting Conversion and Delivery of Electrical Energy*, pp. 1-5, July 2008.

[Medina98] A. Medina and N. Garcia, "Dynamic anayisis of electric arcs using a time domain Newton technique", *CIEP 2008*, Morelia, Mexico, pp. 82-88, 1998.

[Medina03] A. Medina, A Ramos-Paz and C.R. Fuerte-Esquivel, "Periodic steady state solution of electric systems with nonlinear components using parallel processing", *IEEE Trans. on Power Systems*, vol. 18 , no. 2, pp. 963 – 965, 2003.

[Merkhouf08] A. Merkhouf, P. Doyon and S. Upadhyay, "Variable Frequency Transformer-Concept and Electromagnetic Design Evaluation", *IEEE Transaction on Energy Conversion*, vol. 23, Issue 4, pp. 989-996, Dec. 2008.

[Middlebrook76] R. D. Middlebrook and S. Cuk, "A General Unified Approach to Modeling Switching-Converter Power Stages,"in *Proc. IEEE Power Electronics Specialists Conference*, pp. 18-34, June 1976.

[Mohan95] N. Mohan, T. M. Undeland and W. P. Robbins, *Power Electronics: Converters, Applications, and Design*, New York, John Willey & Sons, Inc., 1995.

[Nabb05] D. Mc Nabb, D. Nadeau, A. Nantel, E. Pratico, E. Larsen, G. Sybille, Van Que Do and D. Paré. "Transient and Dynamic Modeling of the New Langlois VFT Asynchronous Tie and Validation with Commissioning Tests", in *Proc. the International Conference on Power Systems Transients*, Montreal Canada, pp. 1-6, June 2005.

[Nadeau07] D. Nadeau, "A 100-MW Variable Frequency Transformer (VFT) on the Hydro-Québec TransÉnergie Network-The Behavior During Disturbance", in *Proc. PES General Meeting*, p.p. 1-5, June 2007.

[Naidu97] S. R. Naidu and B. A. Souza, "Analysis of Ferroresonant Circuits Using a Newton-Raphson Scheme", *IEEE Transactions on Power Delivery*, vol. 12, no. 4, pp. 1793-1798, Oct. 1997.

[Nakhla76] M. S. Nakhla and J. Vlach, "A Piecewice Harmonic Balanced Techniques for Determination of Periodic Response of Nonlinear Systems", *IEEE transaction on Circuits Systems*, vol. 23, No. 2, pp. 85-91, Feb. 1976.

[Nayfeh95] A. H. Nayfeh and B. Balachandran, *Applied Nonlinear Dynamics: Analytical, Computational and Experimental Methods*, New York: John Wiley & Sons, 1995.

[Nelson69] R. H. Nelson, T. A. Lipo and P. C. Krause, "Stability Analysis of a Symmetrical Induction Machine", *IEEE Transactions and Power Apparatus and Systems*, vol. 88, No. 11, pp. 1710-1717, Nov. 1969

[Parker89] T. S. Parker and L. O. Chua, *Practical Numerical Algorithms for Chaotic Systems*, NY: Springer Verlag, 1989.

[Piwko05] R. J. Piwko, E. V. Larsen and C. A. Wegner, "Variable Frequency transformer-a New Alternative for Asynchronous Power Transfer" in *Proc.*

IEEE PES Conferencia y Exposición en Africa, Durban, pp. 393-398, july 2005.

[Pratico07] E. R. Pratico, C. Wegner, E. V. Larsen, R. J. Piwko, D. R. Wallace and D. Kidd, "VFT Operational Overview-The Laredo Project", in *Proc. IEEE Power Engineering Society General Meeting*, Tampa FL, pp. 1-6, June 2007.

[Pratico10] E. R. Pratico, C. Wegner, P. E. Marken and J. J. Marczewski, "First multi-channel VFT application - the Linden project" in *Proc. IEEE Transmission and Distribution Conference and Exposition*, New Orleans, USA, pp. 1-7, April 2010.

[Press02] W. H. Press, S. A. Teukolsky, W. T. Vetterling, and B. P. Flanner, *Numerical Recipes in C++: the Art of Scientific Computing*, Cambridge University Press, 2002.

[Raslan10] E. T. Raslan, A. S. Abdel-Khalik, M. A. Abdulla and M. Z. Mustafa, "Performance of VFT when connecting two power grids operating under different frequencies", in *Proc. IET International Conference on Power Electronics*, Machines and Drives, Brighton, UK, pp. 1-6, April 2010.

[Rico01] J. J. Rico, E. Acha and M. Madrigal, "The Study of Inrush Current Phenomenon Using Operational Matrices", *IEEE Trans. Power Delivery*, vol. 16, No. 2, pp. 231-237, Apr. 2001.

[Rodriguez02] O. Rodriguez and A. Medina, "A Synchronous machine stability analysis using an efficient time domain methodology: unbalanced operation analysis", in *Proc. IEEE Power Engineering Society Summer Meeting*, vol. 2, pp. 677 - 681, 2002.

[Runkle02] M. A. Runkle and E. V. Larsen, "Interconnection Systems for Transmitting Power between Electrical Systems", U. S. Patent 6,356,472, Mar. 12, 2002.

[Sanders91] R. S. Sanders et al., "Generalized averaging method for power conversion circuits", *IEEE Transactions on Power Electronics*, vol. 6, no. 2, pp. 251-259, April 1991.

[Segundo08a] J. Segundo-Ramirez and A. Medina, "Transient and steady-state analysis of the UPFC using a Fourier series approach model", *13th International Conference on Harmonics and Quality of Power*, pp. 1 – 6, 2008.

[Segundo08b] J. Segundo-Ramirez and A. Medina, "Periodic Steady-State Solution of Electric Systems Including UPFCs by Extrapolation to the Limit Cycle", *IEEE Trans. on Power Delivery*, vol. 23 , no. 3, pp. 1506 – 1512, 2008.

[Segundo09] J. Segundo-Ramirez, A. Medina, A. Ghosh and G. Ledwich, "Stability Analysis Based on Bifurcation Theory of the DSTATCOM Operating in Current Control Mode", *IEEE transactions on power delivery*, vol. 24, No. 3, pp. 1670-1678, July 2009.

[Segundo10a] J. Segundo-Ramirez, "Nonlinear Analysis of Power Systems including FACTS nd Custom Power Devices based on Bifurcation Theory and Newton Methods", Doctor in Sciences Thesis in the Facultad de Ingeniería Eléctrica, UMSNH, Morelia 2010.

[Segundo10b] J. Segundo-Ramirez, E. Bárcenas, A. Medina and V. Cárdenas, "Steady-State and Dynamic State-Space Model for Fast and Efficient Solution and Stability Assessment of ASDs", *IEEE Trans. on Industrial Electronics*, Issue 99, Sept. 2010.

[Semlyen95] A. Semlyen and A. Medina, "Computation of the Periodic Steady State in Systems with Nonlinear Components Using a Hybrid Time and Frequency Domain Methodology", *IEEE Transaction on Power Systems*, vol. 10, No. 3, pp. 1498-1504, August 1995.

[Shampine97] L. F. Shampine and M. W. Reichelt, "The Matlab ODE Suite", *SIAM Journal on Scientific Computing*, Vol. 18, pp 1-22, 1997.

[Siemens07] Siemens Work Group, *Program Operation Manual*, Siemens Power Transmission & Distribution, Inc., December 2007.

[Solodovnik98] E. V. Solodovnik, G. J. Cokkinides and A. P. S. Meliopoulos, "Comparison of Implicit and Explicit Integration Techniques on the Non-Ideal Transformer Example", *IEEE Transaction on Power Systems*, vol. 10, No. 3, pp. 32-37, Aug. 1998.

[Stankovic00] A. M. Stankovic and T. Aydin, "Analysis of asymmetrical faults in power systems using dynamic phasors", *IEEE Transactions on Power Systems*, vol. 15, no. 3, pp. 1062-1068, Aug. 2000.

[Truman07] P. Truman and N. Stranges, "A Direct Current Torque Motor for Application on a Variable Frequency Transformer", in *Proc. IEEE PES General Meeting*, pp. 1-5, June 2007.

[Wang06] X. F. Wang, C. J. Cao and Z. C.Zhou, "Experimental on fractional frequency transmission system", *IEEE trans. on Power Systems*, vol. 21, No. 1, pp. 372-277, Feb. 2006.

[Wean01] T. K. Wean, "Overview on Solving Stiff Problems Using One-Step Methods", thesis of Master Science degree, Universiti Teknologi Malasys, 2001.

[Wildberger94] M. Wildberger, "Stability and Nonlinear Dynamics in Power Systems", *EPRI Journal*, pp. 36-39, June 1994.

[Xize02] N. Xize and Q. Jiajun, "Investigation of Torsional Instability, Bifurcation, and Chaos of a Generator Set", *IEEE Transactions on Energy Conversion*, vol. 17, No. 2, pp. 164-168, June 2002.

[VFT07] -"VFT Modeling for Planning Studies", Internal report for the CFE, Mexico, 2007.